Measurement Of The Branching Fraction $\mathbf{Br}(B_s^0 \to D_s^{(*)} D_s^{(*)})$ Using The DØ Detector At Fermilab

James William Walder MPHYS

This thesis is submitted for the degree of Doctor of Philosophy.

· May 2008 ·

Abstract

This thesis describes a measurement of the branching fraction $\mathrm{Br}(B_s^0 \to D_s^{(*)} D_s^{(*)})$ made using a data sample collected from proton-antiproton collisions at a centre-of-mass energy of 1.96 TeV, corresponding to approximately 1.3 fb^{-1} of integrated luminosity collected in 2002–2006 by the DØ detector at the Fermilab Tevatron Collider. One $D_s^{(*)}$ meson was partially reconstructed in the decay $D_s \to \phi\mu\nu$, and the other $D_s^{(*)}$ meson was identified using the decay $D_s \to \phi\pi$ where no attempt was made to distinguish D_s and D_s^* states. The resulting measurement is $\mathrm{Br}(B_s^0 \to D_s^{(*)} D_s^{(*)}) = 0.039^{+0.019}_{-0.017}(\mathrm{stat})^{+0.016}_{-0.015}(\mathrm{syst})$. This was subsequently used to estimate the width difference $\Delta\Gamma_s^{CP}$ in the B_s^0–$\bar{B}_s^0$ system: $\Delta\Gamma_s^{CP}/\Gamma_s = 0.079^{+0.038}_{-0.035}(\mathrm{stat})^{+0.031}_{-0.030}(\mathrm{syst})$, and is currently one of the most precise estimates of this quantity and consistent with the Standard Model.

Acknowledgements

Whilst there are many more people who deserved to be mentioned on this page, I would like to give a special thank you to the following people.

Firstly to Guennadi Borissov, whose exuberance, knowledge and understanding helped motivate and guide me. To Iain Bertram, for all his help throughout my time under his supervision. To Peter Ratoff, for all his support in facilitating my progression. There are many people at DØ who supported the work described herein; a special thank you to Rick van Kooten and Brendan Casey for their comments, advice and assistance. Thank you to the members of Editorial Board 27 for their help in shaping the form of this analysis for public dissemination.

To Louis Lyons, for sparking my interest in particle physics; I'm glad I was able to find out what you did away from our tutorials. I thank Lancaster University for providing financial assistance to carry out this research.

To Chicago, an amazing city, especially my neighbourhood of Wicker Park. With specific thanks to the staff and friends at the Alliance Bakery, Macs and the Pontiac Cafe for providing me with such a welcoming environment in which to work and relax.

To Mark and Sam, for talking through physics, and providing necessary distractions; here's to GT, TF and MK. To Adam, for the many evenings of discussions at Grad, and to everybody else I have known at Lancaster.

To Ceri, for motivating me through the final stages of this thesis.

To my Parents and family, for their help and support through all of my decisions.

Thank you all.

Contents

List of Figures

List of Tables

Chapter 1

Introduction

The current understanding of particle physics is contained within a theory known as the Standard Model of particle physics. It describes a framework of fundamental particles and their interactions, and has successfully been supported by rigourous experimental testing.

As it currently stands the Standard Model is not the final answer. It does not predict the masses of particles, and whilst the Higgs mechanism is the favoured model for the manifestation of mass, the Higgs boson (or bosons) that necessarily appear in this theory has not yet been discovered. Another unresolved question concerns the matter-antimatter asymmetry in the Universe, where the baryonic content of the Universe is believed to be matter dominated. The current known level of $\mathcal{CP}$ violation within the Standard Model is not sufficient to account for the asymmetry found in the observed universe. Whilst it is thought that $\mathcal{CP}$ violation can not provide a full solution to the problem, it may provide evidence for new physics.

To study these phenomena, large and complex scientific facilities are necessary in order to accelerate particles to the energies required to yield interesting interactions. Detectors are designed and built to reveal the residual particles and energy from these collisions, and therefore reconstruct the structure of the interaction.

The work presented in this thesis was carried out at the DØ experiment situated at the Tevatron Collider, at the Fermi National Accelerator Laboratory (Fermilab) in Batavia, near Chicago, Illinois, USA. The accelerator is a high luminosity environment, providing many interactions per second.

The use of hardware and software based triggering algorithms select specific types of events to be recorded for further analysis. This analysis used data collected by the DØ detector between 2002–2006, and corresponds to approximately $1.3\,\mathrm{fb}^{-1}$ of integrated luminosity in collisions of protons and antiprotons at a centre-of-mass energy[1] of 1.96 TeV.

The work contained within this thesis focuses on the neutral B_s meson system, consisting of bottom and strange (anti)quarks ($b\bar{s}, \bar{b}s$). In this system the interaction eigenstates can be different from the states of definite mass (and lifetime). Specifically, this thesis describes the measurement of the decay branching fraction measurement of B_s mesons into two D_s mesons with decays to a total of six final-state charged particles.

Branching fraction measurements are important in themselves, improving our understanding of physical processes, and an increase in precision may be propagated into other analyses. The decay of B_s mesons into two D_s mesons is of further interest, as under certain theoretical assumptions it is possible to relate this decay to the width[2] difference $\Delta\Gamma_s$ between the light and heavy mass eigenstates of the B_s system. Analysis of this decay provides a complementary method to estimate this width difference compared to the direct method of measuring $\Delta\Gamma_s$ with the decay of B_s mesons to $J/\psi(\mu\mu)\phi(KK)$.

In the Standard Model the ratio of the width difference to the average width Γ_s is predicted to be approximately 10%, and deviation from this value would be an indication of new physics. This measurement, along with other measurements at DØ and CDF, as well as future facilities such as the LHC will begin to complete our understanding of the B_s meson, and perhaps illuminate the existence of new physics.

In chapter 2 a brief overview of the Standard Model is presented, focusing on theoretical aspects relevant to this analysis. The DØ detector and Tevatron accelerator are outlined in chapter 3, and a detailed description of the analysis is presented in chapter 4. The results of this measurement, along with a discussion of the systematic uncertainties is given in chapter 5, and the conclusions and summary are presented in chapter 6.

The analysis presented in chapter 4 has been approved by the DØ collab-

[1] Energies are given in units of electron-Volts (eV), where $1\,\mathrm{eV} = 1.6 \times 10^{-19}\,\mathrm{J}$.

[2] The width Γ is related to the lifetime τ by $\Gamma = 1/\tau$.

oration and has been published in Phys. Rev. Lett. [1].

Chapter 2

Theoretical Overview

In this chapter a discussion is given of the Standard Model (SM) in the context of an analysis of B mesons at a hadron collider. For further information on high-energy physics and the SM, the references [2–4] are recommended.

2.1 Symmetry and transformations

Physicists like symmetries. A symmetry exists in a system if, after applying some transformation on the system, the system remains invariant. Some symmetries may appear from continuous transformations, or from discrete operations, such as time reversal, parity and charge conjugation as described below.

The transformations of parity $\mathcal{P}$ and time reversal $\mathcal{T}$ are defined through their effect on the coordinate vector $x^\mu = (t, x^1, x^2, x^3)$. With the convention of the metric $g_{\mu\nu} = \text{diag}(1, -1, -1, -1)$ and $x_\mu = g_{\mu\nu}x^\nu$, $\mathcal{P}$ and $\mathcal{T}$ are described by:

$$\begin{aligned} \mathcal{P}: &\qquad x^\mu \rightarrow x_\mu, \\ \mathcal{T}: &\qquad x^\mu \rightarrow -x_\mu. \end{aligned}$$

That is to say, the operator $\mathcal{P}$ changes the sign of the spatial coordinates, and $\mathcal{T}$ changes $t \rightarrow -t$. It should also be noted that the momentum p^μ and derivative $\partial^\mu = \partial/\partial x_\mu$ transform in the same way under $\mathcal{P}$ and $\mathcal{T}$. The charge conjugation $\mathcal{C}$ operator changes a particle into its antiparticle.

The combination of $\mathcal{CPT}$ is a conserved quantity, however it is now known that $\mathcal{C}$,$\mathcal{P}$, $\mathcal{CP}$, and $\mathcal{T}$ are each violated. An example of violation of symmetry can be seen in the weak-physics sector which contains left-handed neutrinos and right-handed antineutrinos. The operations of either $\mathcal{C}$ or $\mathcal{P}$ operators manifests a particle not found in nature, however the combined $\mathcal{CP}$ operation does not break the symmetry, i.e., $\mathcal{CP}\,|\nu_{LH}\rangle \rightarrow |\bar{\nu}_{RH}\rangle$. Later in this chapter it will be shown where $\mathcal{CP}$ invariance is also violated.

2.2 The Standard Model

The Standard Model (SM) is a mathematical framework that aims to describe the basic elements of matter and their interactions. In the SM, the fundamental particles are divided into fermions with half-integer spin and bosons with integer spin. The fermions (Tables 2.1 and 2.2) form the fundamental particles of matter. The bosons are the force-carrying particles that mediate the short and long range interactions (Table 2.3).

The photon, the carrier of the electromagnetic force, interacts only with electrically-charged particles. Weak interactions are mediated by the $W^{\pm}$ and Z bosons. The strong force is mediated by gluons which couples to particles that contain a "colour" charge quantum number. There are three colours, labelled as "red", "green", and "blue", and corresponding "anti-colours" for antiparticles. Together, these interactions are described by a symmetry group $\mathrm{SU_C}(3) \otimes \mathrm{SU}(2)_\mathrm{L} \otimes \mathrm{U}(1)_\mathrm{Y}$, where U indicates a unitary ($\mathrm{U}^\dagger = \mathrm{U}^{-1}$) group, and SU is the special unitary group with $\det(\mathrm{U}) = 1$.

Table 2.1: Basic properties of the fundamental fermions: leptons [5].

Name	Symbol	Electric charge ($\lvert e\rvert$)	Mass (MeV/c^2)
Electron	e	-1	0.511
Electron neutrino	ν_e	0	$< 2 \times 10^{-3}$
Muon	μ	-1	105.7
Muon neutrino	ν_μ	0	< 0.19
Tau	τ	-1	1777
Tau neutrino	τ_ν	0	< 18.2

Table 2.2: Basic properties of the fundamental fermions: quarks [5].

Name	Symbol	Electric charge ($\lvert e\rvert$)	Mass (MeV/c^2)
up	u	$+\frac{2}{3}$	1.5–3
down	d	$-\frac{1}{3}$	3–7
charm	c	$+\frac{2}{3}$	1250 ± 90
strange	s	$-\frac{1}{3}$	95 ± 25
top	t	$+\frac{2}{3}$	$(172.5 \pm 2.7) \times 10^3$
bottom	b	$-\frac{1}{3}$	$(4.20 \pm 0.07) \times 10^3$

Table 2.3: Basic properties of the fundamental bosons [5].

Force	Gauge boson	Symbol	Electric charge ($\lvert e\rvert$)	Spin	Mass (GeV/c^2)
Electromagnetic	Photon	γ	0	1	0
Weak	Z	Z	0	1	91.2
Weak	$W^{\pm}$	$W^{\pm}$	± 1	1	80.4
Strong	Gluon	g	0	1	0
Gravity	Graviton[a]	G	0	2	0

[a]The Graviton has not been observed experimentally and is not incorporated in the SM.

The group $SU_C(3)$ describes the strong interaction, mediated through the exchange of colour charge in the form of gluons, and is responsible for the structure of Quantum Chromodynamics (QCD). The group $SU(2)_L \otimes U(1)_Y$ describes the electroweak interactions, combining Quantum Electrodynamics (QED) with the weak sector. However, the above group cannot be exact and must be "broken" in such a way that the photon remains massless, whilst the $W^{\pm}$ and Z bosons acquire mass. The method by which this is thought to be achieved is through the Higgs mechanism [6], via spontaneous symmetry breaking, which introduces at least one additional massive boson, the Higgs. This particle is yet to be observed experimentally and current limits [5] give $M_H > 114.4$ GeV/c^2 at 95% CL for a SM Higgs boson. Prior to the discovery of neutrino oscillations, direct transitions between different families in the lepton sector had not been observed, leading to the conservation of lepton number. Incorporating neutrino oscillations, transitions between different lepton generations are possible, whilst overall lepton number is still believed to be conserved.

2.3 Mixing in the quark sector

At a time when only three quarks u, d, s were known, it was observed that the value of the Fermi constant obtained from nuclear β-decays (i.e. $n \rightarrow p + e^- + \bar{\nu}_e$) was smaller than the value deduced using muon decay calculations. Also, the decay $\Sigma^- \rightarrow n + e^- + \bar{\nu}_e$ was suppressed compared to the above decay. Cabibbo [7] proposed a mechanism whereby the u quark coupled, not with the pure flavour eigenstates d, s, but rather with a rotated set of states determined by the Cabibbo mixing angle θ_C: $d' = \cos\theta_C d + \sin\theta_C s$, which thereby solved these two observed discrepancies. This theory was incorporated by Glashow-Iliopoulos-Maiani [8] (the GIM mechanism) for two generations (including the proposal of the positively-charged c quark). Kobayashi and Maskawa [9] extended this framework to three generations and showed that the charge-changing interactions couples u, c, t not with d, s, b, but with

a rotated set

$$\begin{pmatrix} d' \\ s' \\ b' \end{pmatrix} = V_{CKM} \begin{pmatrix} d \\ s \\ b \end{pmatrix}$$

where V_{CKM} is a 3×3 unitary matrix known as the Cabibbo-Kobayashi-Maskawa (CKM) matrix. The weak charge-changing interactions are dominated by transitions within each family, i.e., $u \leftrightarrow d$, $c \leftrightarrow s$, and $t \leftrightarrow b$.

2.3.1 The CKM matrix and the unitarity triangles

A general 3×3 complex matrix contains $2 \times 3^2 = 18$ parameters. The CKM matrix however is constrained to only four free parameters, and whose matrix V_{CKM} is given as

$$V_{CKM} = \begin{pmatrix} V_{ud} & V_{us} & V_{ub} \\ V_{cd} & V_{cs} & V_{cb} \\ V_{td} & V_{ts} & V_{tb} \end{pmatrix}. \tag{2.1}$$

The requirement that the CKM matrix V_{CKM} is unitary reduces the number of free parameters from $2n^2$ to n^2, where n is the number of generations, and hence the size of the matrix. The phases of each of the up- and down-type quarks can be freely rotated, where the overall phase is irrelevant, reducing the number of degrees of freedom by $2n-1$, to give $(n-1)^2$ free parameters. A general $n \times n$ rotation matrix can be described by $\frac{1}{2}n(n-1)$ angles. The number of phases that remain is thus

$$(n-1)^2 - \frac{1}{2}n(n-1) = \frac{1}{2}(n-1)(n-2),$$

and hence for $n = 3$ generations there is one phase angle that can represent $\mathcal{CP}$ violation.

One of the conventional ways to rewrite the CKM matrix is given by the

Wolfenstein [10] parameterisation:

$$V_{CKM} = \begin{pmatrix} 1-\frac{1}{2}\lambda^2 & \lambda & A\lambda^3(\rho-i\eta) \\ -\lambda & 1-\frac{1}{2}\lambda^2 & A\lambda^2 \\ A\lambda^3(1-\rho-i\eta) & -A\lambda^2 & 1 \end{pmatrix} + \mathcal{O}\left(\lambda^4\right), \quad (2.2)$$

where A, $\lambda = |V_{us}|/\sqrt{|V_{ud}|^2 + |V_{us}|^2}$, and $\sqrt{\rho^2+\eta^2}$ are real. An alternative definition [5] can be given as:

$$V_{CKM} = \begin{pmatrix} c_{12}c_{13} & s_{12}c_{13} & s_{13}\mathrm{e}^{-i\delta} \\ -s_{12}c_{23} - c_{12}s_{23}s_{13}\mathrm{e}^{i\delta} & c_{12}c_{23} - s_{12}s_{23}s_{13}\mathrm{e}^{i\delta} & s_{23}c_{13} \\ s_{12}s_{23} - c_{12}c_{23}s_{13}\mathrm{e}^{i\delta} & -c_{12}s_{23} - s_{12}c_{23}s_{13}\mathrm{e}^{i\delta} & c_{23}c_{13} \end{pmatrix}, \quad (2.3)$$

where $s_{ij} \equiv \sin\theta_{ij}$, $c_{ij} \equiv \cos\theta_{ij}$, and δ is the phase angle that governs $\mathcal{CP}$ violation in the SM.

The current estimates of $|V_{ij}|$, the magnitudes of the elements of the CKM matrix, are [5]:

$$V_{CKM} = \begin{pmatrix} 0.97383 \pm 0.00024 & 0.2272 \pm 0.0010 & (3.96 \pm 0.09) \times 10^{-3} \\ 0.2271 \pm 0.10 & 0.97296 \pm 0.024 & (42.21^{+0.10}_{-0.80}) \times 10^{-3} \\ (8.14 \pm^{+0.32}_{-0.64}) \times 10^{-3} & (41.61^{+0.12}_{-0.78}) \times 10^{-3} & 0.999100^{+0.000034}_{-0.000004} \end{pmatrix}. \quad (2.4)$$

As the CKM matrix is unitary ($V^\dagger_{CKM} V_{CKM} = \mathrm{I}$), this leads to the property[1] $V_{ik}V^*_{jk} = \delta_{ij}$, $V_{ki}V^*_{kj} = \delta_{ij}$, or more explicitly for $i \neq j$:

$$V_{ud}V^*_{us} + V_{cd}V^*_{cs} + V_{td}V^*_{ts} = 0, \quad (2.5)$$
$$V_{us}V^*_{ub} + V_{cs}V^*_{cb} + V_{ts}V^*_{tb} = 0, \quad (2.6)$$
$$V_{ud}V^*_{ub} + V_{cd}V^*_{cb} + V_{td}V^*_{tb} = 0, \quad (2.7)$$
$$V_{ud}V^*_{cd} + V_{us}V^*_{cs} + V_{ub}V^*_{cb} = 0, \quad (2.8)$$
$$V_{cd}V^*_{td} + V_{cs}V^*_{ts} + V_{cb}V^*_{tb} = 0, \quad (2.9)$$
$$V_{ud}V^*_{td} + V_{us}V^*_{ts} + V_{ub}V^*_{tb} = 0. \quad (2.10)$$

[1] Where the Einstein summation convention and the Kronecker delta ($\delta_{ij} = 1$ for $i = j$, or 0 otherwise) have been used.

Geometrically, these expressions can be represented as triangles in the complex plane, and are referred to as "unitarity triangles". In general the unitarity triangles form long, thin shapes as one side has a length of differing order of magnitude. However the triangle constructed from the elements in Eq. 2.7 has sides of lengths $\sim \mathcal{O}(\lambda^3)$ and is commonly referred to as The Unitarity Triangle (Fig. 2.1). The Unitarity Triangle can be rescaled

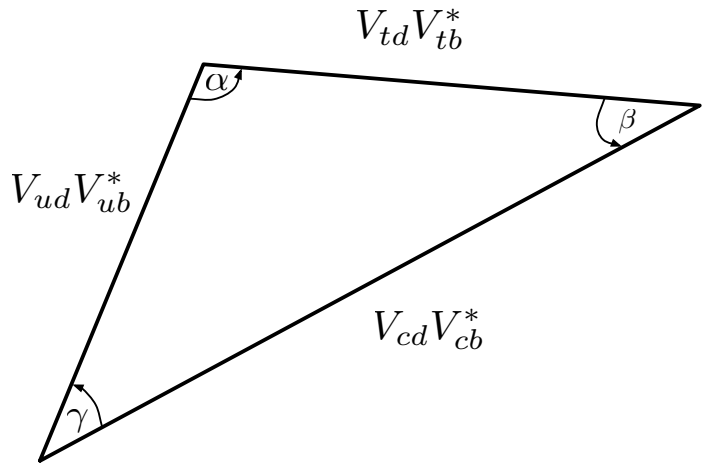

Figure 2.1: The Unitarity Triangle.

(Fig. 2.2) to show the comparison with the Wolfenstein parameterisation in Eq. 2.2.

By examination of the Unitarity Triangle in Fig. 2.1, the angles of the triangle are given as:

$$\begin{aligned}
\alpha \equiv \phi_2 &= \arg\left(-\frac{V_{td}V_{tb}^*}{V_{ud}V_{ub}^*}\right), \\
\beta \equiv \phi_1 &= \arg\left(-\frac{V_{cd}V_{cb}^*}{V_{td}V_{tb}^*}\right), \\
\gamma \equiv \phi_3 &= \arg\left(-\frac{V_{ud}V_{ub}^*}{V_{cd}V_{cb}^*}\right).
\end{aligned} \tag{2.11}$$

In the case of B_s mesons, the corresponding unitarity triangle is given by Eq. 2.6, and its triangle possesses a small angle β. It is possible that new physics processes may be found by investigating the properties of B_s^0 meson

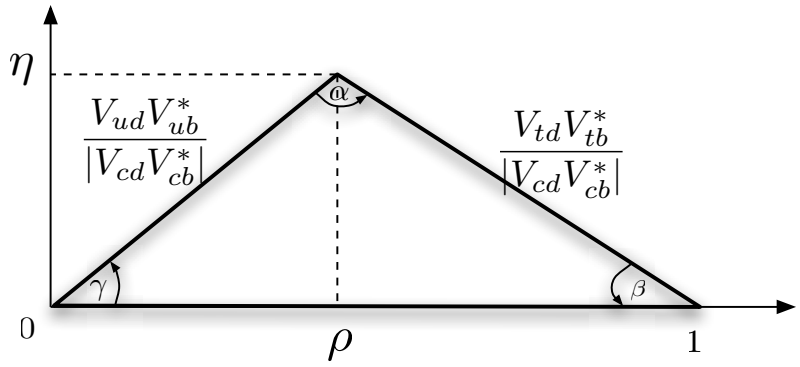

Figure 2.2: The rescaled Unitarity Triangle, where all sides have been redrawn scaled down by $|V_{cd}V^*_{cb}|$.

oscillations.

2.4 Mixing in the $B^0_{d,s}$ meson system

A B^0 meson (where in this section, B^0 refers to either B^0_d or B^0_s) produced initially in a flavour eigenstate B^0 or $\bar{B}^0$ will oscillate over time as a superposition of the two. For a B^0 meson tagged at time $t = 0$ as a B^0 ($\bar{B}^0$), i.e., $|B^0(t=0)\rangle \equiv |B^0\rangle$, the time evolution of the states is governed by the Schrödinger equation:

$$i\frac{\mathrm{d}}{\mathrm{d}t}\begin{pmatrix} |B^0(t)\rangle \\ |\bar{B}^0(t)\rangle \end{pmatrix} = \begin{pmatrix} M_{11} - \frac{i}{2}\Gamma_{11} & M_{12} - \frac{i}{2}\Gamma_{12} \\ M^*_{12} - \frac{i}{2}\Gamma^*_{12} & M_{11} - \frac{i}{2}\Gamma_{11} \end{pmatrix}\begin{pmatrix} |B^0(t)\rangle \\ |\bar{B}^0(t)\rangle \end{pmatrix} \quad (2.12)$$

where M_{ij} and Γ_{ij} are elements of the Hermitian mass M and decay Γ matrices. From CPT invariance [3], $M_{11} = M_{22}$ and $\Gamma_{11} = \Gamma_{22}$.

Transitions of B^0 mesons between $|B^0_s\rangle$ and $|\bar{B}^0_s\rangle$ occur with a change of bottom quantum-number $|\Delta\tilde{B}| = 2$ and produce non-zero off-diagonal elements in Eq. 2.12. This implies a difference between the mass eigenstates of the the neutral B^0 mesons and the flavour eigenstates, B^0 and $\bar{B}^0$. The mass eigenstates, labelled as heavy (B_H) and light (B_L), relate to the flavour

eigenstates through

$$\begin{aligned} |B_{\rm L}\rangle &= p\left|B^0\right\rangle + q\left|\bar{B}^0\right\rangle, \\ |B_{\rm H}\rangle &= p\left|B^0\right\rangle - q\left|\bar{B}^0\right\rangle, \end{aligned} \tag{2.13}$$

where $|p|^2 + |q|^2 = 1$, and noting that in general, $|B_{\rm L}\rangle$ and $|B_{\rm H}\rangle$ are not orthogonal.

The time evolution of the mass eigenstates is then given as:

$$|B_{H,L}(t)\rangle = {\rm e}^{-\left(iM_{H,L}+\Gamma_{H,L}/2\right)t}\,|B_{H,L}\rangle \tag{2.14}$$

and using Eq. 2.13, the time evolution of the flavour states can be expressed as:

$$\begin{aligned} \left|B^0(t)\right\rangle &= \frac{1}{2p}\left\{{\rm e}^{-i\omega_L t}\,|B_L\rangle + {\rm e}^{-i\omega_H t}\,|B_H\rangle\right\}, \\ \left|\bar{B}^0(t)\right\rangle &= \frac{1}{2q}\left\{{\rm e}^{-i\omega_L t}\,|B_L\rangle - {\rm e}^{-i\omega_H t}\,|B_H\rangle\right\}, \end{aligned} \tag{2.15}$$

where the following definitions have and will be used:

$$M = \frac{M_H + M_L}{2} = M_{11}, \tag{2.16}$$
$$\Delta M = M_H - M_L, \tag{2.17}$$
$$\Gamma = \frac{\Gamma_H + \Gamma_L}{2} = \Gamma_{11}, \tag{2.18}$$
$$\Delta\Gamma = \Gamma_L - \Gamma_H, \tag{2.19}$$
$$\omega_{L,H} = M_{L,H} - i\Gamma_{L,H}/2 \tag{2.20}$$
$$\omega = \frac{\omega_L + \omega_H}{2} \tag{2.21}$$
$$\Delta\omega = \omega_H - \omega_L, \tag{2.22}$$

noting that ΔM is positive by definition, and the SM prediction of $\Delta\Gamma$ is positive for the convention adopted in Eq. 2.19.

By substituting the expressions found in Eq. 2.14 into Eq.2.15, the ex-

pressions

$$\begin{aligned} \left|B^0(t)\right\rangle &= g_+(t)\left|B^0\right\rangle + g_-(t)\frac{q}{p}\left|\bar{B}^0\right\rangle, \\ \left|\bar{B}^0(t)\right\rangle &= g_-(t)\frac{p}{q}\left|B^0\right\rangle + g_+(t)\left|\bar{B}^0\right\rangle, \end{aligned} \tag{2.23}$$

are obtained, where

$$g_\pm(t) = \mathrm{e}^{-iMt}\mathrm{e}^{-\Gamma t/2}\left(\mathrm{e}^{\Delta\Gamma t/4}\mathrm{e}^{i\Delta M t/2} \pm \mathrm{e}^{-\Delta\Gamma t/4}\mathrm{e}^{-i\Delta M t/2}\right). \tag{2.24}$$

Equation 2.23 shows that for $t > 0$ there is a non-zero probability for a particle to oscillate, or "mix" to its antiparticle state and vice-versa. The probability for one state to mix (not mix) to the other is proportional to $g^*_\pm g_\pm$:

$$\begin{aligned} P^{\mathrm{no-mix}}(t) &\sim g^*_+ g_+ = \frac{\mathrm{e}^{-\Gamma t}}{2}\left\{\cosh\frac{\Delta\Gamma t}{2} + \cos\Delta M t\right\} \\ P^{\mathrm{mix}}(t) &\sim g^*_- g_- = \frac{\mathrm{e}^{-\Gamma t}}{2}\left\{\cosh\frac{\Delta\Gamma t}{2} - \cos\Delta M t\right\} \end{aligned} \tag{2.25}$$

The terms ΔM, $\Delta\Gamma$ and q/p can be expressed in terms of the off-diagonal elements of the matrix $M - i\Gamma/2$ given in Eq. 2.12. Solving the expression $\det|M - i\Gamma/2 - \omega_{H,L}| = 0$ yields [11],

$$\begin{aligned} (\Delta M)^2 - \frac{1}{4}(\Delta\Gamma)^2 &= 4|M_{12}|^2 - |\Gamma_{12}|^2, \\ \Delta M\Delta\Gamma &= -4\mathrm{Re}(M_{12}\Gamma^*_{12}), \\ \frac{q}{p} &= \frac{\Delta M + i\Delta\Gamma/2}{2M_{12} - i\Gamma_{12}} = \frac{2M^*_{12} - i\Gamma^*_{12}}{\Delta M + i\Delta\Gamma/2}. \end{aligned} \tag{2.26}$$

Another important quantity is the relative phase ϕ between M_{12} and Γ_{12} and is defined by

$$\phi = \arg\left(-\frac{M_{12}}{\Gamma_{12}}\right), \tag{2.27}$$

and is known as the $\mathcal{CP}$ violating phase angle.

An approximate solution for ΔM and $\Delta\Gamma$ can be made for the case

$$|\Gamma_{12}| \ll |M_{12}|, \quad \Delta\Gamma \ll \Delta M,$$

which is found to hold for both the B_s and B_d systems [3]. In such a situation, the expressions

$$\Delta M = 2|M_{12}| \left[1 + \mathcal{O}\left(\left|\frac{\Gamma_{12}}{M_{12}}\right|^2\right)\right], \tag{2.28}$$

$$\Delta\Gamma = 2|\Gamma_{12}| \cos\phi \left[1 + \mathcal{O}\left(\left|\frac{\Gamma_{12}}{M_{12}}\right|^2\right)\right], \tag{2.29}$$

$$\frac{q}{p} = -\mathrm{e}^{i\phi_M}\left[1 - \frac{a}{2}\right], \tag{2.30}$$

are obtained [11], where ϕ_M is just the phase of the matrix element M_{12}, i.e., $M_{12} = |M_{12}|\mathrm{e}^{i\phi_M}$, and a is a small parameter, defined as $|\Gamma_{12}/M_{12}|\sin\phi$ and can often be neglected in calculations [12]. The following section describes the methods by which $\mathcal{CP}$ violation can manifest itself.

2.5 $\mathcal{CP}$ violation

There are three methods by which $\mathcal{CP}$ can be violated. These are classified [13] as $\mathcal{CP}$ violation in:

- decay – occurs in both charged and neutral decays, where the amplitudes for a decay and the $\mathcal{CP}$ conjugate process differ in magnitude;
- mixing – when the $\mathcal{CP}$ eigenstates of a neutral system differs from the mass eigenstates;
- the interference of decays with and without mixing – occurs with decays into final states that are common to both B and $\bar{B}$.

2.5.1 $\mathcal{CP}$ violation in decay

$\mathcal{CP}$ violation in decay[2] occurs when the amplitude A_f for a decay into a final state f differs from the $\mathcal{CP}$ decay $\bar{A}_{\bar{f}}$, such that

$$\left|\frac{\bar{A}_{\bar{f}}}{A_f}\right| \neq 1,$$

as illustrated in Fig. 2.3.

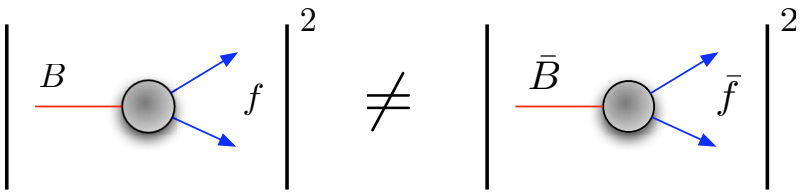

Figure 2.3: Illustration of $\mathcal{CP}$ violation in decay.

The simplest example of $\mathcal{CP}$ violation in decay is in the asymmetry

$$\frac{\Gamma(B^- \to f) - \Gamma(B^+ \to \bar{f})}{\Gamma(B^- \to f) + \Gamma(B^+ \to \bar{f})} = \frac{1 - \left|\bar{A}_{\bar{f}}/A_f\right|^2}{1 + \left|\bar{A}_{\bar{f}}/A_f\right|^2}. \tag{2.31}$$

2.5.2 $\mathcal{CP}$ violation in mixing

$\mathcal{CP}$ violation in mixing[3] can occur when the $\mathcal{CP}$ eigenstates differ from those of the mass eigenstates, i.e.,

$$\left|\frac{q}{p}\right| \neq 1.$$

If $\mathcal{CP}$ were to be conserved, then the relative phase between M_{12} and Γ_{12} would be zero, and the $\mathcal{CP}$ eigenstates would be identical to the mass eigenstates, i.e., $\langle B_{\mathrm{L}}|\, B_{\mathrm{H}}\rangle = |p|^2 - |q|^2$ (from Eq. 2.13) would be orthogonal. Figure 2.4 illustrates this mechanism of $\mathcal{CP}$ violation.

One example of $\mathcal{CP}$ violation in mixing is shown through an asymmetry in the semileptonic decays of neutral mesons to wrong-signed leptons, i.e.,

[2] $\mathcal{CP}$ violation in decay also known as direct $\mathcal{CP}$ violation.
[3] $\mathcal{CP}$ violation in mixing is also referred to as indirect $\mathcal{CP}$ violation.

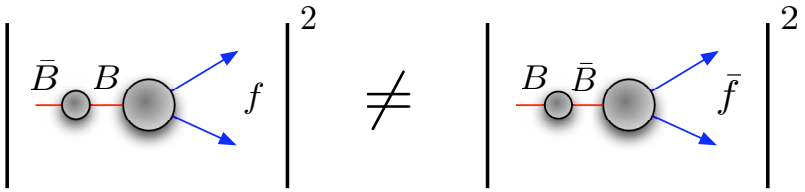

Figure 2.4: Illustration of $\mathcal{CP}$ violation in mixing.

where a meson initially produced in one state, oscillates to the other, and decays semileptonically. The asymmetry is given by [11]:

$$a_{sl} = \frac{\Gamma(\bar{B}^0(t) \to l^+\nu X) - \Gamma(B^0(t) \to l^-\bar{\nu}X)}{\Gamma(\bar{B}^0(t) \to l^+\nu X) + \Gamma(B^0(t) \to l^-\bar{\nu}X)} \tag{2.32}$$

$$= \frac{1 - |q/p|^4}{1 + |q/p|^4}, \tag{2.33}$$

where Eq. 2.33 is obtained by using Eq. 2.23, also noting that a_{sl} is time-independent.

2.5.3 $\mathcal{CP}$ violation in the interference between decay and mixing

In the case of the decay of a neutral meson into a final state with a definite $\mathcal{CP}$ eigenstate f_{CP}, if $\mathcal{CP}$ is conserved then $\left|\bar{A}_{\bar{f}}/A_f\right| = 1$, $|q/p| = 1$, and the relative phase between $\bar{A}_{\bar{f}}/A_f$ and q/p is zero. Defining

$$\lambda_{f_{CP}} = \frac{q}{p}\frac{\bar{A}_{f_{CP}}}{A_{f_{CP}}} = \eta_{f_{CP}}\frac{q}{p}\frac{\bar{A}_{\bar{f}_{CP}}}{A_{f_{CP}}}, \tag{2.34}$$

where $\eta_{f_{CP}} = \pm 1$ is the $\mathcal{CP}$ eigenvalue of f_{CP}; $\mathcal{CP}$ violation occurs through interference between decay and mixing when

$$\lambda_{f_{CP}} \neq \pm 1.$$

Its name is due to the $\mathcal{CP}$-violating interference between $B^0 \to f_{CP}$ and $B^0 \to \bar{B}^0 \to f_{CP}$, as illustrated by Fig. 2.5.

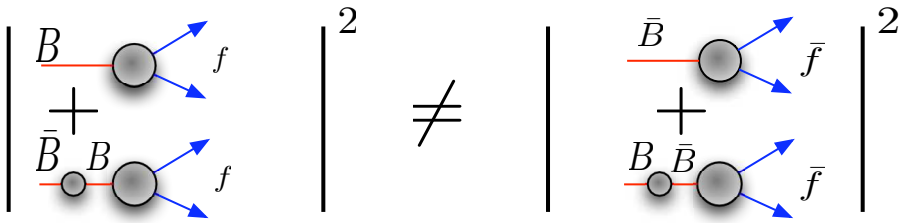

Figure 2.5: Illustration of $\mathcal{CP}$ violation in the interference between decay and mixing.

2.6 Width difference $\Delta\Gamma_s$ and branching fraction $\mathbf{Br}(B_s^0 \to D_s^{(*)} D_s^{(*)})$

In the B_d^0 system, the width difference between the light and heavy mass eigenstates is small; $|\Delta\Gamma_d|/\Gamma_d = 0.009 \pm 0.037$ [5]. In the B_s^0 system, the corresponding width difference may be sizeable [11]. The following text describes the outline of the relationship between the width difference $\Delta\Gamma_s$ and the decay $B_s^0 \to D_s^{(*)} D_s^{(*)}$.

Using the convention $\mathcal{CP}\,|B_s^0\rangle = -\left|\bar{B}_s^0\right\rangle$, the even and odd $\mathcal{CP}$ eigenstates of the B_s^0–$\bar{B}_s^0$ meson system are given as:

$$\begin{aligned} |B_s^{\text{even}}\rangle &= \frac{1}{\sqrt{2}}\left(|B_s^0\rangle - \left|\bar{B}_s^0\right\rangle\right); \\ \left|B_s^{\text{odd}}\right\rangle &= \frac{1}{\sqrt{2}}\left(|B_s^0\rangle + \left|\bar{B}_s^0\right\rangle\right). \end{aligned} \tag{2.35}$$

From the above expressions, the light and heavy eigenstates can be expressed as:

$$\begin{aligned} |B_{s\text{L}}\rangle &= \frac{1}{\sqrt{2}}\left[(p-q)\,|B_s^{\text{even}}\rangle + (p+q)\left|B_s^{\text{odd}}\right\rangle\right], \\ &= \frac{1+\mathrm{e}^{i\phi}}{2}\,|B_s^{\text{even}}\rangle - \frac{1-\mathrm{e}^{i\phi}}{2}\left|B_s^{\text{odd}}\right\rangle, \\ |B_{s\text{H}}\rangle &= \frac{1}{\sqrt{2}}\left[(p+q)\,|B_s^{\text{even}}\rangle + (p-q)\left|B_s^{\text{odd}}\right\rangle\right], \\ &= -\frac{1-\mathrm{e}^{i\phi}}{2}\,|B_s^{\text{even}}\rangle + \frac{1+\mathrm{e}^{i\phi}}{2}\left|B_s^{\text{odd}}\right\rangle, \end{aligned} \tag{2.36}$$

where the second line of each expression is found using Eq. 2.30, and neglecting terms of $\mathcal{O}(a)$. Using these expressions, the time-independent decay-rate for the even and odd eigenstates of the B_s meson can be determined.

2.6.1 Decay rate

The time-dependent decay rate $W(B_s^0(t) \to f)$ of an initially ($t = 0$) tagged[4] B_s^0 meson into a final state f is given by

$$W(B_s^0(t) \to f) \;=\; \frac{1}{N_{B_s^0}} \frac{\mathrm{d}N(B_s^0(t) \to f)}{\mathrm{d}t}, \tag{2.37}$$

where $\mathrm{d}N(B_s^0(t) \to f)$ is the number of B_s^0 mesons that decay into final state f in the time $[t, t + \mathrm{d}t]$ and $N_{B_s^0}$ are the number of B_s^0 mesons at time $t = 0$.

At the Tevatron, where B_s^0 and $\bar{B}_s^0$ mesons are produced in equal quantities, the untagged decay rate $W[f, t]$ for the decay $B_s \to f$ is given by:

$$\begin{aligned} W[f,t] &= W(B_s^0(t) \to f) + W(\bar{B}_s^0(t) \to f) \\ &= \mathcal{N}_f \left[|\langle f| B_{s\mathrm{L}}\rangle|^2 \mathrm{e}^{-\Gamma_L t} + |\langle f| B_{s\mathrm{H}}\rangle|^2 \mathrm{e}^{-\Gamma_H t} \right], \end{aligned} \tag{2.38}$$

where $\mathcal{N}_f$ is an overall normalisation factor. Substituting for $B_{s\mathrm{L}}$ and $B_{s\mathrm{H}}$ with Eq. 2.36 yields

$$\begin{aligned} W[f] = \mathcal{N}_f \Bigg\{ &\left[\frac{1+\cos\phi}{2\Gamma_L} + \frac{1-\cos\phi}{2\Gamma_H} \right] |\langle f| B_s^{\mathrm{even}}\rangle|^2 \\ &+ \left[\frac{1-\cos\phi}{2\Gamma_L} + \frac{1+\cos\phi}{2\Gamma_H} \right] |\langle f| B_s^{\mathrm{odd}}\rangle|^2 \Bigg\}, \end{aligned} \tag{2.39}$$

where the time-dependence on $W[f, t]$ has been integrated out. The relationship between the untagged decay rate and the branching fraction $\mathrm{Br}[f]$ is given by

$$\mathrm{Br}[f] \;=\; \frac{1}{2} \int_0^\infty W[f,t]\, \mathrm{d}t. \tag{2.40}$$

In the next section the decay of B_s mesons to $\mathcal{CP}$-specific final state modes

[4]Tagged mesons are those where the initial state has been identified. This is generally achieved by extracting properties of the B meson produced on the "opposite-side" of the event in $b\bar{b}$ production, or through "same-side" tagging methods.

is considered, before finally establishing the relationship of the decays of $B_s^0 \to D_s^{(*)} D_s^{(*)}$ and the ratio $\Delta\Gamma_s/\Gamma_s$.

2.6.2 Γ_{12} and the decay to $f_{CP^\pm}$

From the definition of Γ_{12} [12] it is possible to express this quantity in terms of final states of definite $\mathcal{CP}$, as follows:

$$\begin{aligned}\Gamma_{12} =& \sum_f \mathcal{N}_f \left\langle B_s^0 \right| f\rangle \langle f| \bar{B}_s^0\rangle \\ =& \frac{1}{2}\sum_f \mathcal{N}_f \left[\left\langle B_s^0\right| f\rangle \langle f| \bar{B}_s^0\rangle + \left\langle B_s^0\right| \bar{f}\rangle \left\langle \bar{f}\right| \bar{B}_s^0\rangle\right], \\ =& -\mathrm{e}^{2i\phi_{c\bar{c}s}} \sum_f \mathcal{N}_f \left[|\left\langle f_{CP^+}\right| B_s^0\rangle|^2 - |\left\langle f_{CP^-}\right| B_s^0\rangle|^2\right], \end{aligned} \tag{2.41}$$

where the second line utilises $\left|\bar{f}\right\rangle = -\mathcal{CP}\left|f\right\rangle$, and in the last line the final state f is separated into its $\mathcal{CP}$-even and $\mathcal{CP}$-odd components $|f\rangle = |f_{CP^+}\rangle + |f_{CP^-}\rangle$, and the $\mathcal{CP}$ transformation

$$\left\langle f_{CP^\pm}\right| \bar{B}_s^0\rangle = \mp \mathrm{e}^{2i\phi_{c\bar{c}s}} \left\langle f_{CP^\pm}\right| B_s^0\rangle,$$

is used, where $\phi_{c\bar{c}s} = \arg(V_{cb}V_{cs}^*)$ is the phase of the $b \to c\bar{c}s$ decay amplitude, dominating Γ_{12} [12].

Finally, inserting expressions for the Eq. 2.35, a new term, $\Delta\Gamma_s^{\mathrm{CP}}$ can be defined as:

$$\Delta\Gamma_s^{\mathrm{CP}} \equiv 2|\Gamma_{12}| = \Gamma(\mathrm{even}) - \Gamma(\mathrm{odd}), \tag{2.42}$$

where Γ(even) and Γ(odd) are the total widths of the decays to $\mathcal{CP}$-even and $\mathcal{CP}$-odd states respectively. From the above expression and Eq. 2.29, the width $\Delta\Gamma_s$ can now be rewritten as

$$\Delta\Gamma_s = \Delta\Gamma_s^{\mathrm{CP}} \cos\phi.$$

2.6.3 The decay $B_s^0 \to D_s^{(*)} D_s^{(*)}$

The decay of B_s mesons to the state $D_s^+ D_s^-$ is $\mathcal{CP}$-even [14]. Under certain theoretical assumptions [14], the decay $B_s^0 \to D_s^{(*)} D_s^{(*)}$ is predominately $\mathcal{CP}$-even, where $D_s^{(*)} D_s^{(*)}$ implies the decays $D_s^+ D_s^-$, $D_s^+ D_s^{*-}$, $D_s^{*+} D_s^-$, and $D_s^{*+} D_s^{*-}$. It is related to the quantity $\Delta\Gamma_s^{\mathrm{CP}}$ under the assumptions as summarised in ref. [12]:

- the decay $B_s^0 \to D_s^+ D_s^-$ is pure $\mathcal{CP}$-even;
- the decay $B_s^0 \to D_s^{\pm} D_s^{*\mp}$ is forbidden in the heavy quark limit ($m_c \to \infty$) and neglecting particular terms $\mathcal{O}(1/N_c)$ (where $N_c = 3$ is the number of colours), hence the decay of B_s mesons to $D_s^{\pm} D_s^{*\mp}$ is $\mathcal{CP}$-even;
- In the Shifman-Voloshin (SV) limit $m_c \to \infty$, with $m_b - 2m_c \to 0$, the width of the B_s^{odd} decays vanishes, and the decay of B_s mesons to $D_s^{(*)} D_s^{(*)}$ saturates $\Delta\Gamma_s^{\mathrm{CP}}$.

The even and odd widths are thus given as $\Gamma(B_s^{\mathrm{even}} \to D_s^{(*)} D_s^{(*)}) \approx \Delta\Gamma_s^{\mathrm{CP}}$, $\Gamma(B_s^{\mathrm{odd}} \to D_s^{(*)} D_s^{(*)}) \approx 0$, and by substituting for $\Delta\Gamma_s^{\mathrm{CP}}$ from Eq. 2.42, and combining with the branching fraction (Eq. 2.40) and untagged decay rate (Eq. 2.39), an estimate of the parameter $\Delta\Gamma_s^{\mathrm{CP}}$ can be made from the decay $B_s^0 \to D_s^{(*)} D_s^{(*)}$:

$$\begin{aligned} 2\mathrm{Br}(B_s^0 \to D_s^{(*)} D_s^{(*)}) &\approx \Delta\Gamma_s^{\mathrm{CP}} \left[\frac{1+\cos\phi}{2\Gamma_L} + \frac{1-\cos\phi}{2\Gamma_H} \right] \\ &= \frac{\Delta\Gamma_s^{\mathrm{CP}}}{\Gamma_s} \left[1 + \mathcal{O}\left(\frac{\Delta\Gamma_s}{\Gamma_s} \right) \right]. \end{aligned} \tag{2.43}$$

It should be noted that this equation holds under the theoretical assumptions summarised above, and without experimental determination of the individual decay fractions of the four states of $B_s^0 \to D_s^{(*)} D_s^{(*)}$, some caution should be given as to the validity of this relationship. It does however provide a independent measure of $\Delta\Gamma_s$.

2.6.4 SM prediction of $\Delta\Gamma_s/\Gamma_s$

The SM prediction of $\Delta\Gamma_s/\Gamma_s$ is given as [15]:

$$\frac{\Delta\Gamma_s}{\Gamma_s} = 0.147 \pm 0.060. \tag{2.44}$$

Recalling that $\Delta\Gamma = \Delta\Gamma^{\mathrm{CP}} \cos\phi$ and, in the SM $\phi \approx -0.004\,\mathrm{rad.}$, thus $\Delta\Gamma_{SM} \approx \Delta\Gamma_s^{\mathrm{CP}}$. The term $\Delta\Gamma^{\mathrm{CP}}$ is not sensitive to the effects of new physics as Γ_{12} is dominated by tree-level processes. Significant deviation from the SM expectation value would be evidence of new physics processes.

2.7 B meson production at the Tevatron

The leading-order QCD processes responsible for the production of heavy quark pairs are quark–antiquark annihilation and gluon–gluon fusion as shown in Fig. 2.6. For t quarks, the former process dominates, whilst it is the latter for b quarks [16]. In such a model, the b and $\bar{b}$ quarks are produced

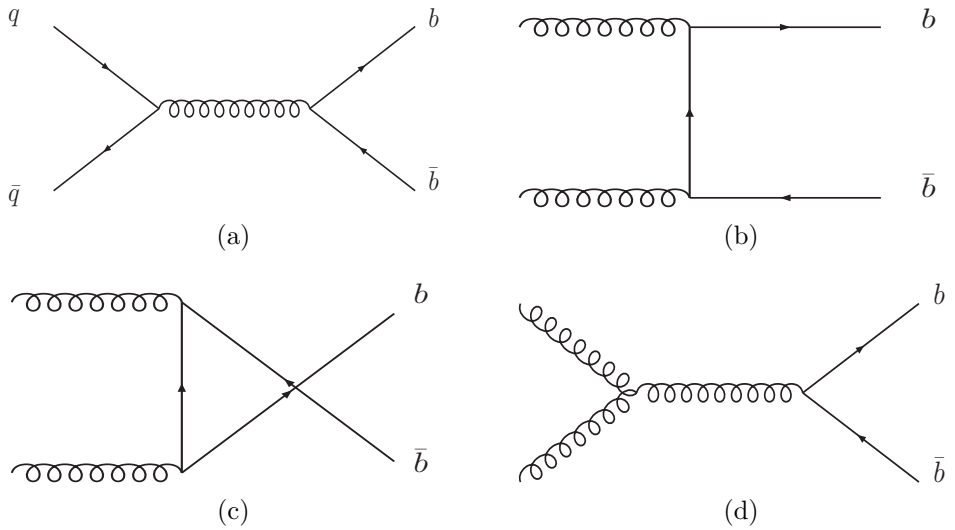

Figure 2.6: The leading-order diagrams for production of $b\bar{b}$ quark pairs through (a) quark-antiquark annihilation and (b)–(d) gluon-gluon fusion.

back-to-back in the plane transverse with respect to the beam direction.

After the initial hard process of forming a $b\bar{b}$ pair, B hadrons are formed through hadronisation or fragmentation. A $q\bar{q}$ pair will "pop" out of the

vacuum as the $b\bar{b}$ pair move apart to form colour-neutral systems. A $\bar{b}$ quark[5] will produce B^+, B^0, B_s^0, B_c^+ and $\bar{b}$-baryons depending on the initial flavour of the vacuum-quark pair. The lighter masses of the u and d quarks result in higher production rates for B^+, B^0 mesons. The production of b-baryons is suppressed as two additional quarks are required, and the production of B_c^+ is negligible compared to other modes. The production fractions for b hadrons are given in Table 2.4.

Table 2.4: Probabilities of production for b-hadrons [5].

Hadron	Symbol	Probability (%)
B^+	f_u	40.0 ± 1.0
B^0	f_d	40.0 ± 1.0
B_s^0	f_s	10.8 ± 1.2
b baryons	f_{baryons}	9.2 ± 1.8
B_c^+	f_c	negligible

2.8 Current experimental results

The branching fraction $\text{Br}(B_s^0 \to D_s^{(*)} D_s^{(*)})$ has been previously measured by the ALEPH collaboration at the LEP collider in the correlated production of $\phi\phi$ mesons. By using an event counting technique with background subtraction, the result $\text{Br}(B_s^0 \to D_s^{(*)} D_s^{(*)}) = 0.12^{+0.11}_{-0.06}$ was obtained [17].

The CDF collaboration performed a measurement [18] with $355\,\text{pb}^{-1}$ of integrated luminosity using their Run II detector in the decay of B_s^0 mesons to $D_s^+ D_s^-$ and obtained the ratio

$$\frac{\text{Br}(B_s \to D_s^+ D_s^-)}{\text{Br}(B^0 \to D_s^+ D^-)} = 1.67 \pm 0.41\,(\text{stat}) \pm 0.12\,(\text{syst}) \pm 0.24\,(f_s/f_d) \pm 0.39\,(\text{Br}_{\phi\pi}). \quad (2.45)$$

Even with the estimate $\text{Br}(B^0 \to D_s^+ D^-) = (6.5 \pm 1.3) \times 10^{-3}$ [5], comparison to $\text{Br}(B_s^0 \to D_s^{(*)} D_s^{(*)})$ is difficult as the excited D_s^* meson modes are excluded.

[5] With corresponding hadrons for b quarks.

Both the DØ and CDF collaborations have measured the width difference $\Delta\Gamma_s$ in the decays of B_s mesons in the decay $B_s \to J/\psi(\mu^+\mu^-)\phi(K^+K^-)$. In this decay, the final states contains contributions of $\mathcal{CP}$-even and $\mathcal{CP}$-odd modes. The two $\mathcal{CP}$ states produce different angular distributions in their decays and, by collecting a sample of B_s mesons, a time-dependent three-angle fit to the data can separate the $\mathcal{CP}$ states to allow the width difference and $\mathcal{CP}$-violating phase angle to be extracted.

The DØ collaboration have measured [19] τ_s, $\Delta\Gamma_s$ and ϕ_s corresponding to $2.8\,\text{fb}^{-1}$ of integrated luminosity using "flavour-tagging" to identify the flavour of the initial state of the B_s meson. The results using a free value for ϕ_s are summarised in Tab. 2.5.

The CDF collaboration, using $1.7\,\text{fb}^{-1}$ integrated luminosity, measured [20] τ_s, $\Delta\Gamma_s$ and ϕ_s using untagged decays and under the assumption of $\mathcal{CP}$ conservation. Their results are summarised in Tab. 2.5. The CDF collaboration have also performed a measurement [21] using $1.35\,\text{fb}^{-1}$ integrated luminosity with flavour-tagged decays of B_s mesons to obtain a bound on $2\beta_s$, the mixing-induced CP parameter[6], given in Table 2.5.

Table 2.5: Summary of current theoretical results from the decay $B_s \to J/\psi\phi$. The statistical uncertainty is given first; the systematic uncertainty is second.

Experiment	Parameter	Value
DØ [19]	τ_s (ps)	$1.52 \pm 0.06 \pm 0.01$
	$\Delta\Gamma_s$ (ps^{-1})	$0.19 \pm 0.07^{+0.02}_{-0.01}$
	ϕ_s	$-0.57^{+0.24\ +0.07}_{-0.30\ -0.02}$
CDF [20]	τ_s (ps)	$1.52 \pm 0.04 \pm 0.02$
	$\Delta\Gamma_s$ (ps^{-1})	$0.076^{+0.059}_{-0.063} \pm 0.006$
CDF [21]	$2\beta_s$	$[0.32, 2.82]$

[6] $2\beta_s = 2\text{arg}\left\{\frac{-V_{ts}V_{tb}^*}{V_{cs}V_{cb}}\right\}$. Both $\phi_s \approx 0.004$ and $2\beta_s \approx 0.04$ are small in the SM, and any new physics would contribute equally to these angles.

Chapter 3

The Fermilab Accelerator Complex and the DØ Detector

The Fermilab accelerator collider is located close to Chicago, Il., USA, and is currently home to the highest-energy collider in the world. As well as performing fixed-target experiments, it supplies high-energy protons and antiprotons for collisions in the Tevatron accelerator ring.

The two detectors situated on the Tevatron are called DØ and CDF[1]. The initial running period of the DØ detector, known as Run I, occurred from 1992–1995, with centre-of-mass energy of $\sqrt{s} = 1.8\,\text{TeV}$, and collected approximately $120\,\text{pb}^{-1}$ of data. With a substantially upgraded detector, including a central tracking system with silicon and scintillating-fibre based trackers enclosed in a solenoid magnet, Run II operations began in 2001. The Tevatron was also upgraded to supply an increased luminosity and a collision centre-of-mass energy of $\sqrt{s} = 1.96\,\text{TeV}/c^2$. The period of Run IIa occurred between 2001–2006. With further upgrades, the Run IIb detector has been in operation since 2006 and is expected to continue into 2009 and potentially beyond.

In this chapter, the accelerator complex and DØ detector are briefly described, with emphasis on the components used to provide the proton-antiproton interactions in the Tevatron and the detector systems essential for a B physics related analysis.

[1] CDF is an acronym for the Collider Detector at Fermilab. The DØ detector is so-called as it is positioned at the point labelled D0 of the Tevatron.

3.1 The Fermilab Tevatron Collider accelerator

To obtain protons and antiprotons and then to accelerate them to collision energies requires several stages of particle acceleration. These accelerator components (illustrated in Fig. 3.1) are described briefly below.

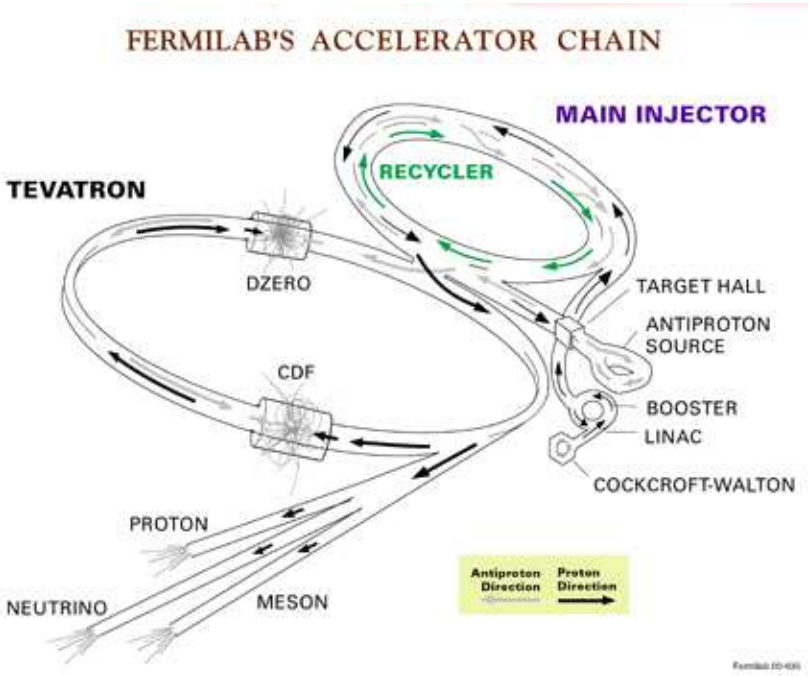

Figure 3.1: Schematic of the Fermilab accelerator chain [22].

3.1.1 Proton source

A bottle of hydrogen gas provides the source of protons for collisions. Additional electrons are injected into the hydrogen gas, forming negatively-charged hydrogen ions that are then accelerated by a Cockroft-Walton accelerator to 750 keV and then by a Linac to 400 MeV, prior to injection into the Booster. The Booster is 475 m in circumference and strips the electrons from the atoms using a carbon foil. The remaining protons are accelerated from 400 MeV to 8 GeV during $\sim$ 16 thousand revolutions.

3.1.2 Antiproton production

Antiprotons are produced from protons with an energy of 120 GeV from the Main Injector (described below) which impact on a Nickel target every 1.5 s. The particles produced in the collision are focused using a lithium lens and antiprotons are selected using a pulsed magnet. These antiprotons are bunched in time and the Debuncher is used to transform the high-energy narrow-time spread of the antiprotons to a low-energy large-time spaced source in a period of approximately 100 ms by stochastic cooling. Antiprotons are transferred to the accumulator where they are stored for extended periods of time until enough are gathered to enter a store[2]. Cooling is also applied in the Accumulator.

3.1.3 The Main Injector and Recycler

The Main Injector takes 8 GeV protons from the Booster and accelerates them up to energies of 120 GeV for antiproton and fixed-beam experiments, or 150 GeV for injection into the Tevatron. Antiprotons are also taken from the Accumulator or Recycler at 8 GeV and injected into the Tevatron.

The Recycler is situated in the same tunnel as the Main Injector and is comprised of a series of permanent magnets and is used to collect antiprotons from the Accumulator and contain them until they are needed for a store. Typically the Recycler stores up to ~ 2–3×10^{12} antiprotons.

3.1.4 The Tevatron

The Tevatron is the final accelerator in the chain and is a 6 km circumference ring that accelerates protons and antiprotons each to energy of 980 GeV. Protons and antiprotons are transported in the same beampipe due to their opposite charge. Superconducting 4 T dipole magnets are used to keep the beams in a circle and quadrapole magnets are used to focus the beam area.

The instantaneous luminosity $\mathcal{L}$ is given by

$$\mathcal{L} = \frac{N_p N_{\bar{p}} n_B f}{4\pi\sigma_a^2}, \tag{3.1}$$

[2]A store is the period in which protons and antiprotons are circulated in the Tevatron for collisions.

where N_p and $N_{\bar{p}}$ are the number of particles in the p and $\bar{p}$ bunches respectively, σ_a^2 the cross-sectional area of interaction, n_B is the number of bunches, and f is the frequency of bunch revolution. Typical values for Run IIa operations are shown in Table 3.1.

Table 3.1: Typical Tevatron beam values. Symbols are defined in section 3.1.4

Parameter	Value
N_p	$\sim 2.7 \times 10^{11}$
$N_{\bar{p}}$	$\sim 3 \times 10^{10}$
σ_a^2	$\sim 5 \times 10^{-5}\,\mathrm{cm}^2$
n_B	36
f	$\sim 50\,\mathrm{kHz}$
Peak luminosity	$\sim 10^{32}\,\mathrm{cm}^{-2}\mathrm{s}^{-1}$
Interactions per crossing	~ 2.3

The performance of the Tevatron has increased throughout Run IIa operation, with a peak luminosity reaching $1.71 \times 10^{32}\,\mathrm{cm}^{-2}\mathrm{s}^{-1}$ [23] as shown in Fig. 3.2. The integrated luminosity recorded to the DØ detector is shown in Fig. 3.3.

3.2 The DØ detector

This section gives a brief description of the DØ detector with emphasis given to the components important to the analysis described in this Thesis. The majority of information in this section relating to the DØ detector has been derived from the detailed reference [24]. The cross-sectional view of the DØ detector is shown in Fig. 3.4 and displays the major systems of the detector.

3.2.1 The DØ coordinate system

A right-handed coordinate system is used in DØ where the z-axis is defined by the direction of the proton beam, the y-axis points vertically upwards and the x-axis is in the direction away from the centre of the Tevatron. The

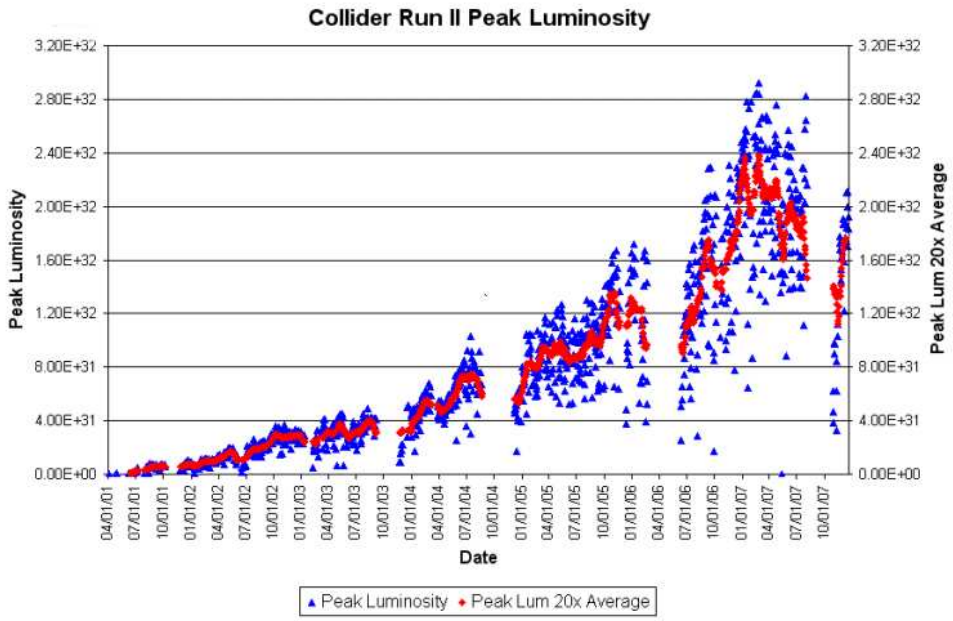

Figure 3.2: Peak luminosity delivered by the Tevatron accelerator during the DØ Run II period of operation (2001–2007) [22]. The breaks in data indicate periods of accelerator shutdown, used for upgrades and repairs. In blue the peak luminosity is displayed, and in red, the average peak luminosity using the previous 20 runs.

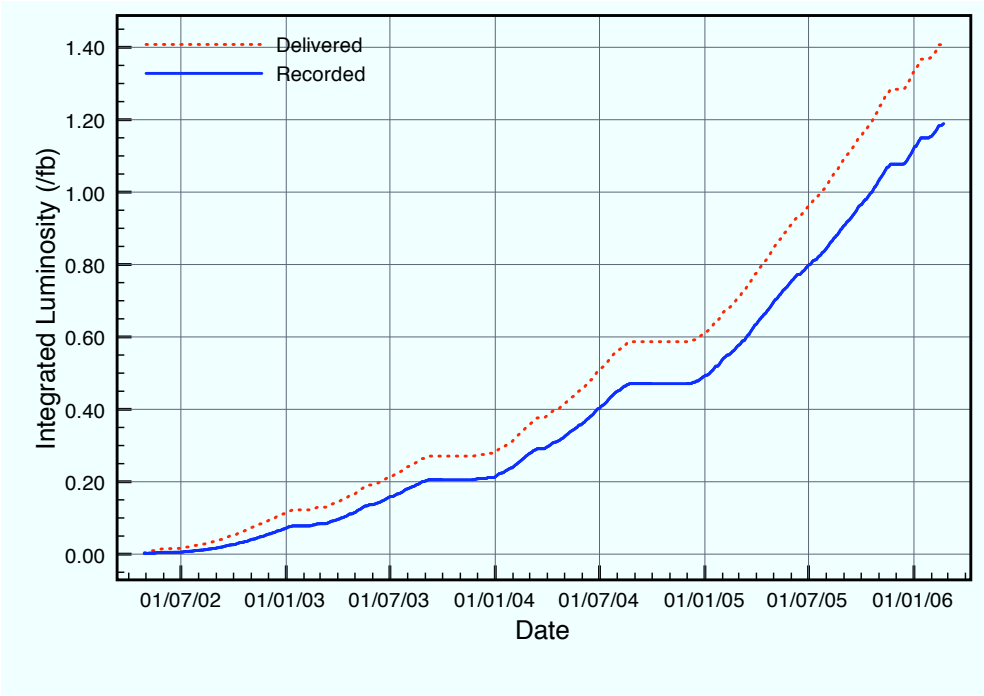

Figure 3.3: Integrated luminosity delivered to (dotted line) and recorded by (solid line) the DØ detector during the Run IIa (2002–2006) period of operation.

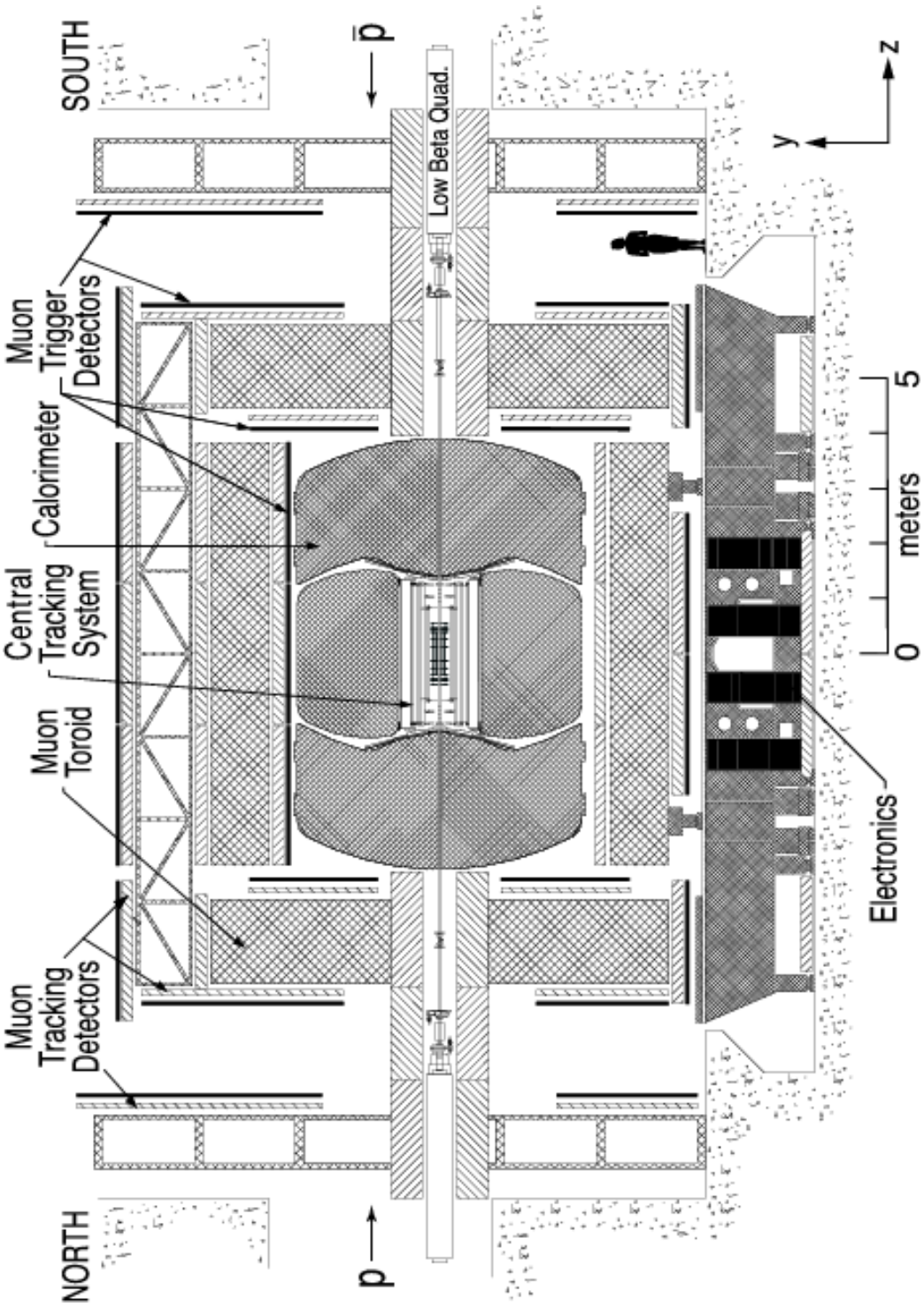

Figure 3.4: Cross-sectional view of the DØ detector with major detector subsystems labelled [24].

origin $(0, 0, 0)$, is defined as the geometric centre of the DØ detector. The azimuthal (ϕ) and polar (θ) angles are defined by

$$\phi = \tan^{-1}\left(\frac{y}{x}\right),$$
$$\theta = \tan^{-1}\left(\frac{r}{z}\right),$$

where r is the perpendicular distance from the direction of the beam. It is also useful to define other quantities for use in further discussion. As transverse momentum is an approximately conserved quantity, the transverse variables $p_{\mathrm{T}} = p\sin\theta$ is used. The rapidity y is defined by

$$y = \frac{1}{2}\ln\left(\frac{E + p_{\mathrm{z}}}{E - p_{\mathrm{z}}}\right)$$

and can be approximated in the ultra-relativistic limit $m/E \to 0$ by the pseudo-rapidity η:

$$\eta = -\ln\left[\tan\left(\frac{\theta}{2}\right)\right].$$

Rapidity is a useful quantity as Δy is invariant under longitudinal Lorentz-transformations.

3.2.2 Silicon Microstrip Tracker

The requirement of precise tracking is essential for many physics studies, including b physics. Surrounding the Beryllium beam-pipe is the Silicon Microstrip Tracker (SMT) which is itself enclosed by the Central Fiber Tracker (CFT). This is surrounded by a 2 T solenoid as shown in Figure 3.5. The collision interaction region has a length scale of $\sigma_z \approx 25\,\mathrm{cm}$, and influences the design of the tracking detectors to allow maximal performance throughout this region.

As illustrated in Fig. 3.6 the SMT is comprised of horizontal barrels, interspersed with vertical disks. There are six 12 cm barrel sections each consisting of four silicon layers. The silicon modules within the barrel are called "ladders", of which there are twelve (twenty-four) ladders in layers 1,2 (3,4) for a total of 432 ladders. The central radius of each layer is at

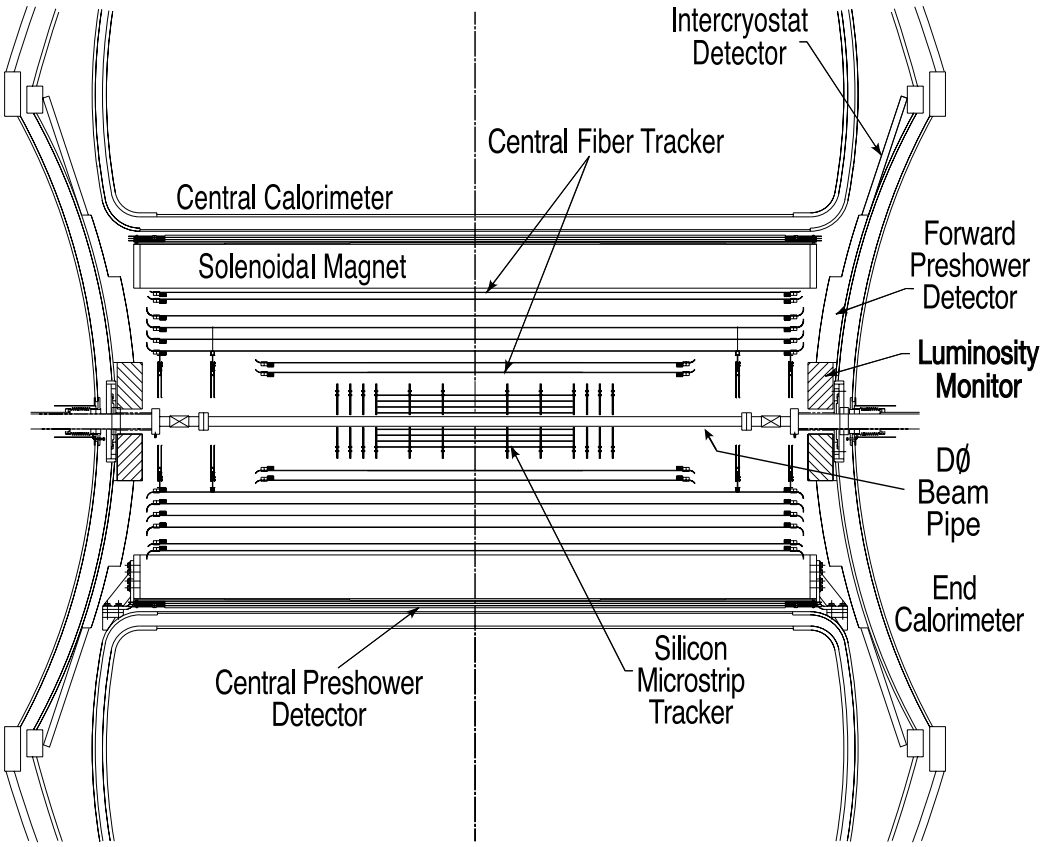

Figure 3.5: Cross-section in the xz plane of the central tracking system in relation to outer components of the detector [24].

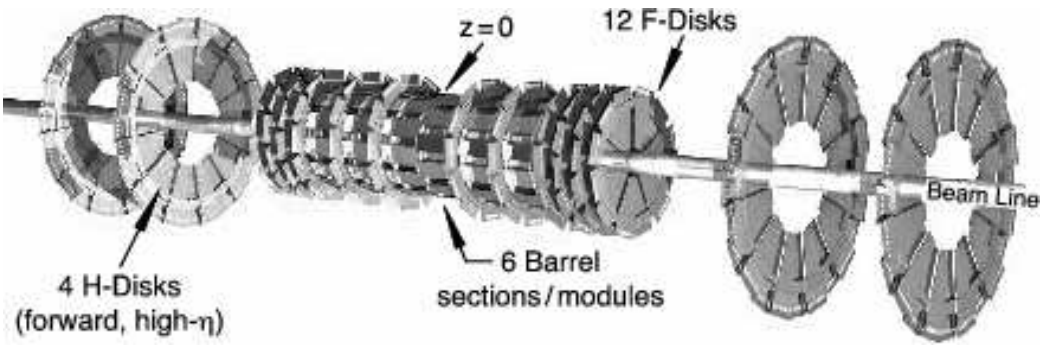

Figure 3.6: Silicon microstrip tracker layout [24].

$r = 2.7, 4.6, 7.6, 10.5\,\text{cm}$. The first and third layers of the inner four barrel sections are made from stereo 90° sensors. On the outer two barrels layers 1 and 2 use single-sided axial sensors, and for all barrels, the second and fourth layers are constructed from double-sided stereo sensors with a 2° offset between the stereo and axial strips.

The twelve F-disks are placed at $\pm z = 12.5, 25.3, 38.2, 43.1, 48.1, 53.1\,\text{cm}$ and have an inner radius of 2.6 cm, and outer radius 10 cm. Each F-disk is made from twelve double-sided wedge modules. The four[3] H-disks are located at $\pm z = 100.4, 121.0\,\text{cm}$ and extend the coverage of the SMT. Each H-disk is made from twenty-four full wedges, with two single-sided half wedges glued back-to-back each with ±7.5° difference. The single-hit resolution for the SMT is typically around $10\,\mu\text{m}$.

3.2.3 Central Fibre Tracker

The CFT, illustrated in Fig. 3.5, is made from eight concentric cylinders using scintillating fibres. Its radius covers $20 < r < 50\,\text{cm}$, with a length of 1.66 m for the inner two layers so as to avoid the H-disks and the other six layers each with length 2.52 m. Tracking coverage is provided out to $|\eta| \lesssim 1.7$. Each of the eight cylinders contains one doublet layer of fibres orientated along the $\hat{z}$ direction (axial direction), and another double layer orientated at a stereo angle ϕ of $+3°$ ($\hat{u}$) or $-3°$ ($\hat{v}$) (stereo directions). The stereo orientation ($\hat{u}$ or $\hat{v}$) alternates for each cylinder starting with $\hat{z}\hat{u}$ for the innermost cylinder.

The scintillating fibres are connected to clear fibre waveguides which transmit the light to the Visible Light Photon Counters (VLPC). The base material for the scintillating fibres is polystyrene doped (1% by weight) with an organic fluorescent dye paraterphenyl. Excitations in the polystyrene cause the dye to emit light at a wavelength of approximately 340 nm. This wavelength is strongly attenuated in the polystyrene, therefore in order for the light to exit the module it is wave-shifted to 530 nm using a low concentration of 3-hydroxyflavone dye where it can be easily transmitted. The VLPCs are silicon-impurity avalanche diodes operated at $\sim 9\,\text{K}$. The VLPC

[3]Note that for Run IIb operations the outer two H-disks were removed.

provides single photon detection and a fast response. Trigger[4] information is provided at Level 1 from axial doublet layers for tracks above specified p_{T} thresholds. Level 1 candidate tracks are used in Level 2, and Level 3 utilises the full detector readout information. For the CFT, a single-hit resolution of 150 μm is typical.

3.2.4 Solenoid

The solenoid was designed to fit within the physical constraints of the Run I detector and has dimension of 2.73 m in length and 1.42 m diameter. The superconducting magnet generates an approximately uniform 2 T field in the central region and is cooled using a system of liquid helium and liquid nitrogen systems. This field value was selected to optimise the tracking resolution $\delta p_{\mathrm{T}}/p_{\mathrm{T}}$ given the design constraints. The solenoid polarity is designed to be reversed, which is important in some physics analyses (e.g. [25]) to cancel systematic effects of the detector geometry, and tracking differences between particles of opposite charge. The solenoid and supporting devices contribute approximately a radiation length (X_0) in thickness to the detector.

3.2.5 Preshower detectors

The Forward Preshowers (FPS) and Central Preshower (CPS) are used both online and offline to aid in the identification of electrons and discrimination of background. Both types of preshower detector are constructed using interleaved triangular strips of scintillator with wavelength-shifting fibres that transport light to the VLPCs. Each scintillating layer provides stereo information. The CPS sits between the solenoid and central calorimeter and provides coverage out to $|\eta| < 1.3$ which is increased by the two FPS placed on each end calorimeter, covering $1.5 < |\eta| < 2.5$. The CPS contains approximately $1X_0$ thickness of lead covered in stainless steel skins with three concentric layers of scintillator. The FPS is situated on the face of the end calorimeter cryostats and consists of two scintillator layers separated by $2X_0$ of lead and stainless steel absorber.

[4]The trigger system is described in further detail in section 3.3 on page 38.

3.2.6 The Calorimeter

The calorimeter of the DØ detector is a destructive system for energy measurements of electrons, photons and jets. The three calorimeter sections are shown in Fig. 3.7 and are called the Central Calorimeter (CC), End Calorimeter North (ECN), and End Calorimeter South (ECS). Coverage of this detector extends to $|\eta| \lesssim 1$ for the CC and is extended to $|\eta| \sim 4$ with the two end calorimeters. Each calorimeter is contained within its own cryostat to maintain an operating temperature around 90 K.

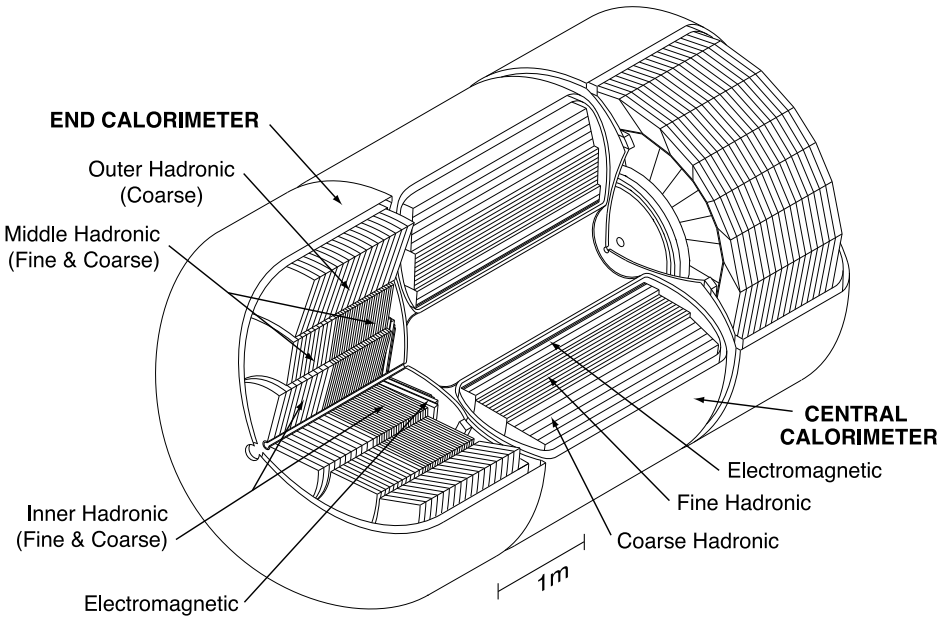

Figure 3.7: View of the central and two end calorimeters [24].

Each calorimeter is divided into the sections: Electromagnetic (EM), situated closest to the beampipe; Fine Hadronic (FH), located outside of the electromagnetic; and the Coarse Hadronic (CH), furthest from the interaction region. The choice of using liquid argon as the active component in sampling ionisation from hadronic and electromagnetic showers was motivated by the gain and relative ease of calibration [26]. The absorbers consist of depleted uranium and steel.

3.2.7 The Muon system

The identification and momentum measurements of muons are facilitated through the muon detector system. The primary reason for energy loss of typical muons produced from the proton-antiproton collisions is through ionisation, meaning that muons are able to penetrate through the whole detector, hence any detectable particle to make it out of the DØ detector is likely to be a muon.

The muon system provides coverage $|\eta| \lesssim 2.0$ using the Wide Angle Muon System (WAMUS) operating out to $|\eta| \approx 1.0$, and the Forward Angle Muon Systems (FAMUS) which extends the coverage. Both systems have Scintillation counters, shown in Fig. 3.8a, providing fast timing information. To make precision position measurements, the WAMUS contains Proportional Drift Tubes (PDT), whereas the FAMUS uses Mini Drift Tubes (MDT), both shown in Fig. 3.8b. To measure the momentum, toroid magnets of approximately 1.9 T bend the muon trajectory in the rz plane. The magnets are situated between the innermost muon layer A and the two outer B and C layers. The central toroid covers the region $|\eta| \leq 1$, and is at a radius $r = 318\,\text{cm}$ from the beamline. The two end toroids are located at $454 \leq |z| \leq 610\,\text{cm}$. As with the solenoid, the polarity of the toroid is also routinely reversed. The triggering of muon events occurs using both scintillation counters and wire chambers, and both contribute to background rejection from scintillation counters for timing information and wire chambers for track segments.

The WAMUS is constructed with three layers of scintillation counters and PDTs. The PDT are made of rectangular extended aluminium tubes with a typical area $2.8 \times 5.6\,\text{m}^2$ and are subdivided into cells 10.1 cm across. Typical chambers are 24 cells wide and the A (B,C) layer contains 96 (72) cells. A gas mixture 84% argon, 8% methane and 8% CF_4 gives a drift velocity of approximately $10\,\text{cm}/\mu\text{s}$ and maximum drift time of approximately 500 ns.

The FAMUS is similar to the WAMUS and has a three layer system, however it uses MDTs with a gas mixture of 90% CF_4 and 10% CH_4. The maximum drift time is 60 ns.

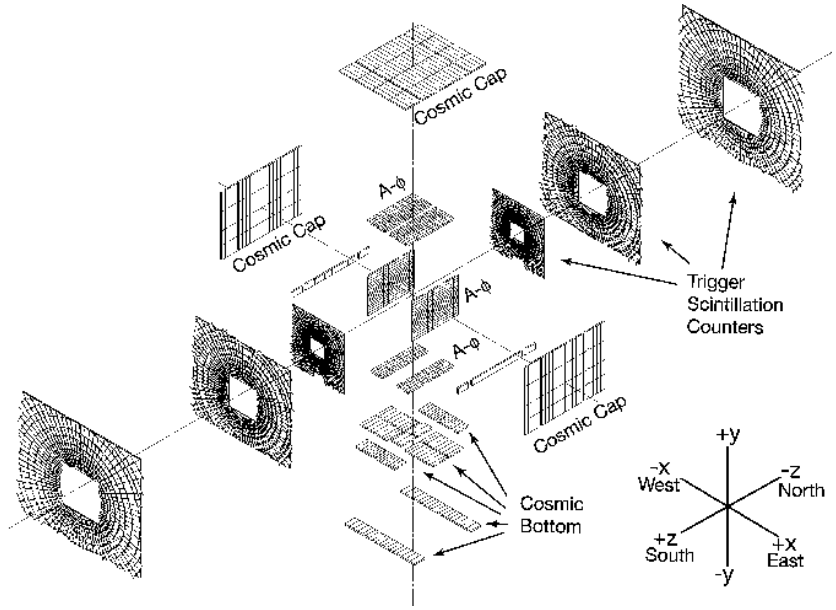

(a)

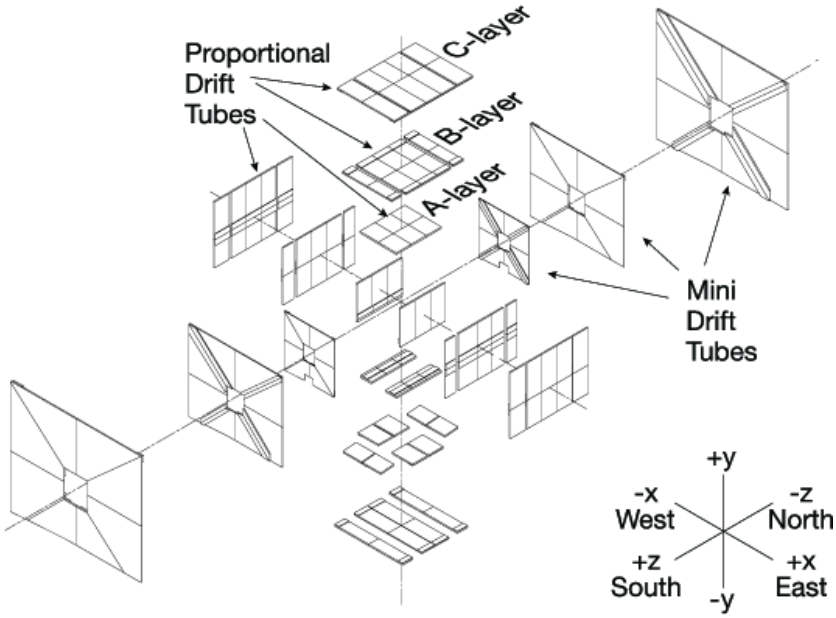

(b)

Figure 3.8: a) Muon scintillation detectors. b) Wire chambers of muon system [24].

3.2.8 Luminosity monitor

The Luminosity Monitor (LM) detectors are situated at $z = \pm 140\,\text{cm}$ and each consist of an array of twenty-four scintillation counters with PMT readout that covers $2.7 < |\eta| < 4.4$. Time-of-flight resolution for the counters is approximately 0.3 ns.

The purpose of the LM is to determine the luminosity at DØ using inelastic $p\bar{p}$ collisions, and also to provide a fast method of primary vertex position measurements and beam halo rates. The luminosity $\mathcal{L}$ is determined from $\mathcal{L} = f\bar{N}_{LM}/\sigma_{LM}$, where f is the beam crossing frequency, σ_{LM} the cross-section for the LM after acceptance and efficiency. The average number of $p\bar{p}$ interactions $\bar{N}_{LM}$ is determined using Poisson statistics by considering the fraction of beam crossings with no interactions.

Discrimination between beam halo backgrounds and $p\bar{p}$ interactions is performed from time-of-flight information to determine the interaction z coordinate $z_v = \frac{c}{2}(t_- - t_+)$, where $t_\pm$ are the particle time-of-flight measurements at the corresponding LM. Events where $|z_v| < 100\,\text{cm}$ are considered to have originated from an interaction, whereas beam halos in the $\pm\hat{z}$ direction will have $z_v \approx \mp 140\,\text{cm}$.

3.3 The DØ trigger system

The number of interactions occurring in the DØ detector are far greater than the capabilities to capture all events. Also, many of these interactions are from inelastic $p\bar{p}$ scattering and are not interesting enough to be recorded, hence the utilisation of a trigger system to select events based on certain criteria allow the event capture rate to be controlled and potentially interesting events to be recorded.

Three levels of trigger are applied, where each successive level reduces the number of events and increases the complexity of computation. The Level 1 trigger is hardware based and reduces the event rate by a factor of $\sim$1000. At Level 2, individual objects are reconstructed and correlations performed using subdetector-based embedded microprocessors to pass information to a global trigger processor, which roughly halves the rate. Events that pass Level 1 and 2 are then passed to a farm of CPUs where more detailed reconstruction

occurs. Successful events are recorded to tape for full reconstruction later with an average output rate of 50 Hz.

Control and co-ordination of the DØ triggering system is managed by the system COOR. COOR accepts user-inputs to start or stop runs, configure the trigger system, and to send correct signals to Levels 1,2 and 3. A list of network addresses for online services is also stored by the COOR system, which enables the communication of time-dependent information (such as beamspot position) to be available to the trigger systems. A schematic of the full chain is given in Fig. 3.9.

As luminosity increases,some triggers take more of the available bandwidth. In order to limit the event rate to the total bandwidth required the use of prescales are employed. A prescale setting will randomly reject a trigger on a certain fraction of events. The event may still be accepted as if another trigger fires, the event will be recorded anyway.

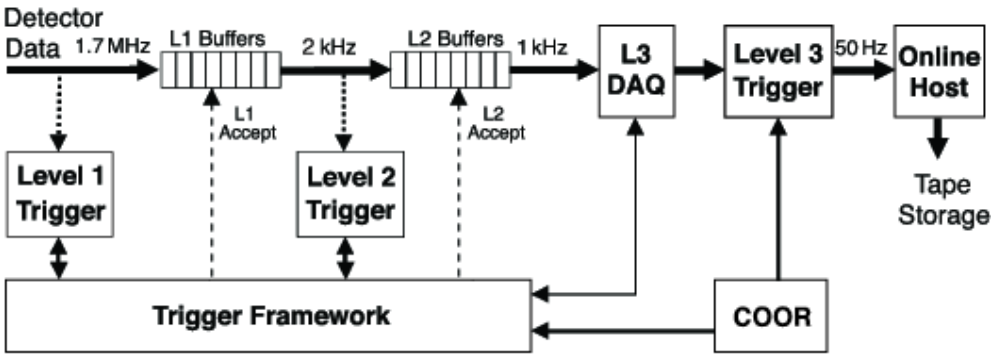

Figure 3.9: Schematic overview of the trigger system [24].

3.3.1 Level 1

Level 1 (L1) is designed to examine every event and make decisions on specific patterns. It is hardware based and designed to accept a bream crossing rate of 2.5 MHz and output around 2 kHz.

Trigger decisions can be either "yes" or "no", so must be based on threshold values rather than non-binary responses. For the calorimeter trigger (L1Cal) transverse energy deposits thresholds are used. The muon (L1Muon)

and central track triggers (L1CTT) are examined both combined and separately for tracks that exceed specified thresholds.

Minimising deadtime is essential at L1 and the event is stored in pipelined buffers. A Level 1 decision to accept or reject the event is required within 3.5 μs. The limitation of the accept rate from L1 is governed by the time taken to read out the participating subsystems of the detector.

Trigger framework

The Trigger Framework (TFW) is responsible for issuing accept or reject decisions at Level 1. It is capable of issuing vetoes for various triggers as well as applying prescales. There are 128 triggers (called "physics" triggers) that can be formed from the 256 bits (called "AND-OR" terms) of the detector systems. By "OR-ing" all of these triggers it can be determined if a beam crossing should be accepted. For each of the 128 physics triggers a "beam condition" trigger is associated with it that must also be satisfied.

3.3.2 Level 2

At L2, the rate is reduced from approximately 2 kHz (although designed to handle up to 10 kHz) to approximately 1 kHz. L2 uses a global processor (L2Global) and preprocessing systems for the subdetector systems to test for physics signatures. From the set of triggers fired at L1 and additional selection criteria, an event that passes L2 requests full readout of the detector for further analysis at L3.

Paralleled preprocessors for subsystems such as muon, tracking and calorimetry work with L2Global to produce physics objects from across the subsystems. An unbiased sampling mode can also be set which passes all L1 accepted events to L3 without rejection, however the result of the L2 triggers are still recorded.

3.3.3 Level 3

Full detector information is read out at L3 for events that are accepted from L2. Simpler reconstruction algorithms than offline reconstruction are used to form complete physics objects as well as relationships between objects. The

software is required to unpack the raw data, locate hits, form clusters, apply calibration corrections and reconstruct physics objects such as electrons, vertices and $\not\!\!E_T$[5]. If an event is accepted at L3 then it is recorded to tape for full offline reconstruction. The output rate is at an average of approximately 50 Hz.

3.3.4 Triggering for b-physics

The principle form of triggering for b-physics analyses at DØ is through muon identification. Three methods of muon triggering are used [27]:

- di-muon triggers – where the decays of J/ψ mesons, rare decays $B_s \rightarrow \mu\mu$, or single-muon decays where a second muon is used to identify the flavour of the B_s meson decay;
- lifetime-unbiased single-muon triggers – using track-matched muons with momentum threshold values of $3, 4$ and 5 GeV;
- impact-parameter biased single-muon triggers – by selecting muons with a large impact parameter, the flavour of a B meson can be determined without biasing the signal-side of the event.

The trigger rates used in b-physics compete with other physics analyses for the available bandwidth. As these other analyses tend to require high-p_{T} triggers, the b-physics triggers can utilise the additional rate that is available at lower luminosity, as shown in Fig. 3.10.

3.4 Computing and software

The standard programming language for Run II is C++, with legacy software from Run I or external non-C++ software often utilising FORTRAN contained within C++ wrappers. This section briefly describes the structure within the DØ experiment including the simulation of events for a typical b-physics analysis.

[5] $\not\!\!E_T$ is defined as the missing transverse energy.

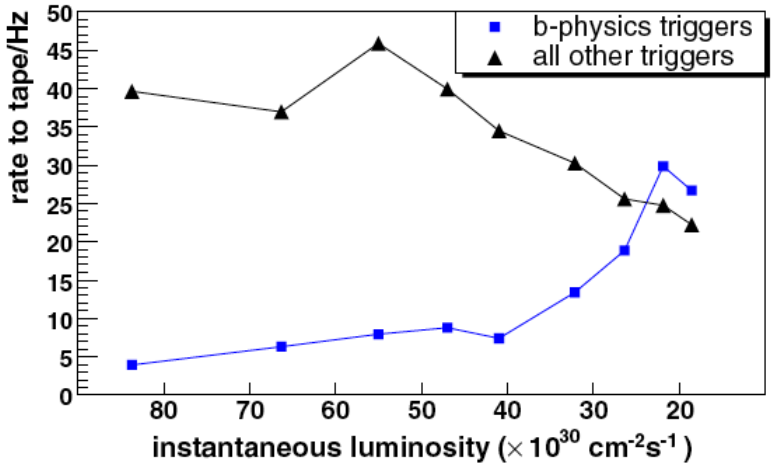

Figure 3.10: Data event rate written onto tape for b and non-b physics triggers with respect to decreasing instantaneous luminosity within a typical store [27].

3.4.1 Event simulation

The production of Monte Carlo (MC) events to simulate a beam crossing in the detector requires the use of several packages. The initial step in MC event generation is the simulation of the physical process of $p\bar{p}$ interactions, producing a set of decays according to the hard-scattering of the underlying event. PYTHIA [28] is a commonly used program which outputs momentum four-vectors and vertex information. The decay of b-hadrons and their daughter particles is typically managed through the package EvtGen [29], which is a framework responsible for the complex sequential decays that may occur where $\mathcal{CP}$-violating effects and angular distributions are important. For processes with small branching fractions, it can be necessary to consider the time required to process the desired number of events, as it is an unnecessary use of resources to perform the full simulation chain for events that will never pass the selection criteria. The package DØ_MESS [30] was designed to filter and reject events according to simple topological or kinematic selection criteria.

The DØ detector is a complex device of many components of different materials and thicknesses that must accurately be simulated to correctly describe the detector response for each event. The executable DØGSTAR [31]

uses the program GEANT [32] to determine paths through active media, energy deposition and secondary interactions of the representative model of the detector. The program DØSIM [33] takes the MC response and applies modifications accounting for detector related effects. Inefficiencies within the detector and noise contributions from readout electronics and detector elements must be modelled, as well as possible multiple interactions per beam crossing.

For the analysis described in chapter 4 the simulated data were produced using the DØ software release p14.07.00, with PYTHIA version 6.202, using the parton distribution function set CTEQ5L [34].

3.4.2 Offline event reconstruction

The program DØRECO [35] is the standard offline reconstruction program processing real data and MC events to produce objects used in further analysis. The Event Data Model (EDM) is used to store information and results within blocks or "chunks" for the event. The Raw Data Chunk (RDC), created by an L3 processor node or MC is the primary input to DØRECO, which then outputs additional chunks associated with the reconstructed objects.

Detector-specific components are extracted from the RDC where electronic channels are associated with detector components and calibration constants are applied. Hit and cluster objects are formed from the raw information to be passed further down the reconstruction chain. Track reconstruction is the most CPU intensive operation in event reconstruction and utilises the hit objects from the SMT and CFT to form track objects. These tracks can be used to identify vertices. The locations of primary vertex (PV) candidates are formed that identify the position of $p\bar{p}$ interactions and can be used to impose various constraints. Next, secondary vertices displaced from the primary interaction are located, originating from the decays of long-lived particles. Using the objects that have been reconstructed, physics-object candidates such as muons, electrons, $\not\!\!E_T$, etc., can then be found.

Central tracking reconstruction

Charged particles traversing the tracking components of the SMT and CFT are registered as "hits" by elements within the detector. These hits are used to form clusters used in tracking algorithms. In the SMT a number of adjacent strip elements may register a hit, characterised by Analog-to-Digital Counts (ADC). After strip-by-strip offsets and gains are applied [36], the central position of the cluster is given by the pulse height weighted average $\bar{n}$:

$$\bar{n} = \frac{\sum_{i}^{N} n_i w_i}{\sum_{i}^{N} w_i}. \tag{3.2}$$

Here, n_i is the strip number and w_i the ADC value for the i^{th} adjacent strip above threshold ADC count. The centroid of the cluster u is given by $u = u_1 + (\bar{n} - 1)p$, where u_1 is the local position of the first strip and p, the strip pitch. These local coordinates are then converted to the global system.

For the CFT the light yield is converted to an ADC value using calibrations for offset and gain in each fibre. Adjacent hits above threshold are included in cluster finding and the centroid is defined as the mid-point between cluster edges.

Cluster points are used in track finding, a cpu intensive process to form tracks from a number of hypotheses. A number of algorithms are employed at DØ. One method, AATrack, is outlined in section 3.4.3.

Muon reconstruction

Reconstruction of muon-object candidates requires: identification of hits in the muon detectors; fitting straight-line segments to the hits; and track fitting, including central track matching.

Hits in the muon scintillator system are determined from the drift time and increase precision. After hits have been reconstructed, links are formed between the hits within 20 cm of each other. These links are then combined to try and form straight-line track segments. Two segments compatible with a new straight line are combined to form a new segment, and these line

segments are extrapolated to scintilator hits and the track refitted. For the B and C layers a fit is performed including both layers as there is no magnetic field between them. The best segments are selected using the track hypothesis that provides the lowest χ^2/ndf. For the case of segments with only two hits, the segment that extrapolates a track closest to the primary vertex is selected. A "local" muon track is formed from a fit to the A and BC-layers and includes the effects of the magnetic fields, energy deposition and multiple scattering.

3.4.3 AATrack

The reconstruction of tracks for DØ is performed using the tracking algorithms AATrack [37], HTF [38], and GTR [39]. The AATrack and HTF algorithms are used to form a pool of track hypotheses that are then input to GTR to perform a final filter and refit of the tracks, as illustrated by Fig. 3.11. The HTF algorithm uses the transformation of hits from the coordinate space (x, y) to the parameter space (ρ, ϕ), where ρ is the curvature of a track, defined by $\rho = qB/p_{\mathrm{T}}$, and ϕ is the direction of the track at the closest point of approach to the beamline[6]. A hit in this parameter space is represented as a line (or a band if uncertainties are included), and a track as a point. Therefore hits from the same track will intersect at the point representing the track.

The AATrack algorithm is useful for b-physics as it has a higher track reconstruction efficiency for lower momentum particles than the HTF algorithm, and hence will be discussed in further detail.

The AATrack algorithm builds a list of track hypotheses by considering tracks that satisfy the following criteria, which are added to a pool of tracks. A track hypothesis begins in the SMT by selecting a series of three axial hits, which contains at least one stereo measurement per hit. The hypothesis is extrapolated to the next layer in the SMT or CFT and, if a hit is found within the expected crossing region, it is added to the track hypothesis and the track is refitted. If multiple new hits are found, a new hypothesis is created for

[6]The case of small impact parameters ($d_0 \sim 0$) is considered in this algorithm, reducing the number of parameters required to describe a track in the plane perpendicular to the magnetic field from three (ρ, d_0, ϕ) to two.

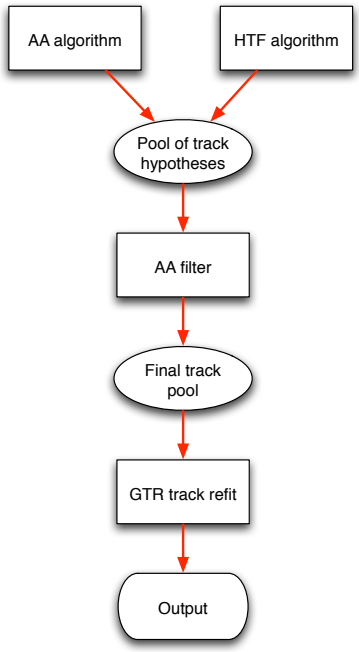

Figure 3.11: Flow-diagram illustrating the track hypothesis, filtering and refitting stages of track reconstruction [40].

each new hit using the shared previous hits. In the case that no hit is found, and the particular element is known to be active, a "miss" is recorded, which accounts for possible detector inefficiencies. This extrapolation technique continues until either three consecutive misses are recorded, or the outside of the CFT is reached. If the track hypothesis contains a sufficient number of hits-versus-misses in the detector it is added to the track pool.

Once a list of tracks has been found, a two pass filtering technique is applied. The tracks are ordered into a sequence with priority given to: greatest number of track hits, fewest misses, and smallest χ^2 of the track fit. The tracks are then filtered according to the number of axial hits N_s they share with a previous track, compared to the total number N_t of axial hits on the track. A track is kept if either of the two conditions:

- $N_s \leq \frac{2}{3}N_t$ and $N_t - N_s \geq 4$;
- $N_s \leq \frac{1}{5}N_t$

are met. From this pool of tracks the primary vertices are found (see below for vertex reconstruction), which is used as a constraint in the second pass of the filter.

The final set of tracks are found by adding to each track two fake hits, situated close to the estimated PV. This technique allows the tracks to be ordered in preference of distance from the PV, which means for tracks sharing a number of hits, the track that passes closest to the PV is favoured, reducing fakes. The previous ordering and filtering procedure is reapplied to provide the final track selection.

Vertex and beamspot reconstruction

The primary vertex is determined on an event-by-event basis, using the beamspot position and a set of tracks. The position of the beamspot tends to remain stable throughout a run, hence its position is determined from the run-averaged position from the beamspot database, and can be used as a constraint in the fit of the primary vertex. The χ^2 function minimised to determine the PV position ($\vec{V}$) is given by [41]:

$$\chi^2(\vec{V}) = \sum_a \sum_{\alpha,\beta=1,2} d^a_\alpha (S^{-1}_a)_{\alpha\beta} d^a_\beta + \sum_i \frac{(V^{sp}_i - V_i)^2}{(\sigma^{sp}_i)^2}. \tag{3.3}$$

Here, d_α and d_β are the two-dimensional vectors of transverse and longitudinal impact-parameter components respectively for the track a, and S is the covariance matrix of the measured impact parameter components. The first term is summed over all tracks a. In the second term, V_i^{sp} and σ_i^{sp} are the beamspot position and size for $i = \{x, y\}$ coordinates. The inclusion of the beamspot constraint is able to reduce the resolution of the PV from approximately 30–60 μm to 20–25 μm. To reduce bias from tracks not originating from the PV, the χ^2 fit is repeated, excluding one track, for all tracks in the fit. The fit which yields a maximum deviation of χ^2 value from the original fit has the corresponding track excluded from the PV, if the difference in χ^2 is greater than 9. This procedure is repeated until no further tracks are excluded. Secondary vertices are found by only considering the first term of Eq. 3.3.

3.4.4 Tracking performance

When reconstructing tracks the possibility exists that erroneous information, such as detector-related noise, is included in the fitting procedures leading to incorrectly reconstructed, or fake, tracks. For the Run IIa period of data-running, the rate of fake track production is typically less than 2%. For the more recent period of Run IIb, which exists in an environment of higher luminosity, the fake rates are still estimated at only 3–4% [42]. Miss-reconstructed tracks, or tracks that originate from real particles but are distorted due the presence of detector noise, inefficiencies in detector subsystems, or miss-allocation of hits occur at a rate of typically 7–8% [43], meaning less than 10% of tracks are incorrectly reconstructed. The transverse momentum resolution of the joint SMT and CFT subsystems is found to be:

$$\Delta p_{\mathrm{T}} = 0.002 \cdot (p_{\mathrm{T}})^2 \, [\,\mathrm{GeV}/c]$$

which implies a typical momentum resolution of $\approx 5\,\mathrm{GeV}/c$ for a $p_{\mathrm{T}} = 50\,\mathrm{GeV}/c$ particle [42].

In the muon system the efficiency of matching a muon in the muon system to a track in the central tracking region is estimated to be an average of

$\approx 95\%$ [44]. This study was performed using a sample of $Z \to \mu\mu$ events.

Chapter 4

Analysis

This chapter describes the measurement of the branching fraction $\mathrm{Br}(B_s^0 \to D_s^{(*)} D_s^{(*)})$ using a sample of semileptonic B_s^0 decays collected by the DØ experiment at Fermilab in $p\bar{p}$ collisions at $\sqrt{s} = 1.96$ TeV. The data correspond to an integrated luminosity of approximately 1.3 fb^{-1}. The B_s^0 meson was selected through the decay $B_s^0 \to D_s^{+(*)} D_s^{-(*)}$, where one D_s^+ decays to $\phi_1 \pi^+$, the other D_s^- decays by $\phi_2 \mu^- \nu$, and where each ϕ meson decays by $\phi \to K^+ K^-$. Charge conjugate states are implied throughout. The ϕ mesons which are produced from each D_s meson are distinguished in the text by the subscripts {1,2}, as used above. No attempt was made to reconstruct the photon or π^0 from the decay $D_s^* \to D_s \gamma/\pi^0$ and thus the state $D_s^{(*)} D_s^{(*)}$ contains contributions from $D_s D_s$, $D_s^* D_s$ and $D_s^* D_s^*$. To reduce systematic effects, the branching fraction $\mathrm{Br}(B_s^0 \to D_s^{(*)} D_s^{(*)})$ was normalised to the decay $B_s^0 \to D_s^{(*)} \mu \nu$.

4.1 Analysis outline

Of the total data sample collected by the DØ detector, only a tiny fraction of events are of interest to this analysis. By application of selection criteria or "cuts", a sample may be selected that maximises the purity of the signal process of interest, whilst minimising the contamination of background events. With the application of these selection criteria and with the inevitable detector-related inefficiencies, MC simulations are used to estimate and correct for these effects. The analysis was performed using the BANA [45]

software package, which forms the basis of many b-physics studies at DØ. It provides access to track, particle and vertex information, and provides methods to filter decay tracks from neutral particle candidates as well as particle identification of J/ψ candidates.

This chapter first describes the decay processes of interest, including important backgrounds, then defines the selection criteria used to obtain three data samples: the preselection sample of initial candidate events; the ($\mu D_s^{(*)}$) sample of candidates for the normalisation channel; and the ($\mu\phi_2 D_s^{(*)}$) sample with candidate events for the final selection of signal events. The methods used to extract parameters of interest from the data are then described, along with necessary cross-checking procedures. The use of MC in determining background contamination and in estimating the efficiencies is then considered.

4.2 Decay channels

The signal decay chain for $B_s^0 \to D_s^{(*)} D_s^{(*)}$ is shown in Fig. 4.1 where it can be seen that there are six reconstructed final-state objects, one D_s that decays semileptonically, and that the charge of the muon and pion are opposite.

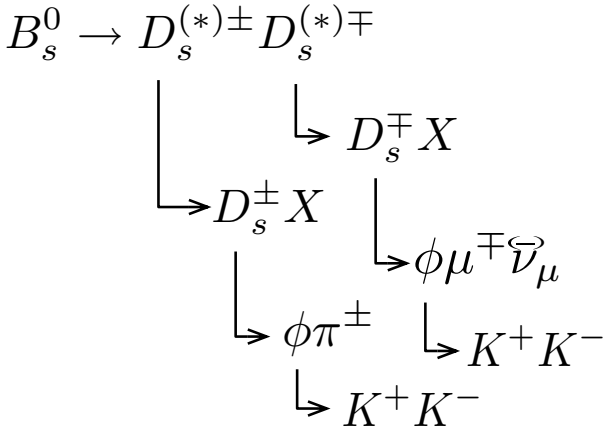

Figure 4.1: Reconstructed decay chain for the channel $B_s^0 \to D_s^{(*)} D_s^{(*)}$. Here $X = \gamma(94.2\%), \pi^0(5.8\%)$ for decays of the excited state D_s^* meson, or $X =$ nothing for the decay of the non-excited D_s.

The above decay is normalised to the decay of $B_s^0 \to D_s^{(*)} \mu\nu X$, with the

full decay chain shown in Fig. 4.2.

$$B_s^0 \to D_s^{(*)\pm}\mu^{\mp}\overset{(-)}{\nu}_{\mu}$$
$$\hookrightarrow D_s^{\pm}X$$
$$\hookrightarrow \phi\pi^{\pm}$$
$$\hookrightarrow K^+K^-$$

Figure 4.2: Reconstructed decay chain for the channel $B_s^0 \to D_s^{(*)}\mu\nu$. Here $X = \gamma(94.2\%), \pi^0(5.8\%)$ for decays of the excited state D_s^* meson, or $X =$ nothing for the decay of the non-excited D_s.

The choice of the specific decay mode $D_s \to \phi\mu\nu$ is due to trigger requirements (such that a muon is identified according to the criteria defined in section 4.5). The decay $D_s \to \phi\pi$ has a branching fraction 0.045 ± 0.004 [5], and contains a vertex of three charged particles. The decay $\phi \to K^+K^-$ was selected due to its high (0.493 ± 0.006) [5] branching fraction and ease of reconstruction.

4.3 Branching fraction calculation

The value $\mathrm{Br}(B_s^0 \to D_s^{(*)}D_s^{(*)})$ is extracted from the equation

$$\frac{N(\mu\phi_2 D_s^{(*)}) - N_{\mathrm{bkg}}}{N(\mu D_s^{(*)})\ f(B_s^0 \to D_s^{(*)}\mu\nu)} = \frac{2\ \mathrm{Br}(B_s^0 \to D_s^{(*)}D_s^{(*)}) \cdot \mathrm{Br}(D_s \to \phi\mu\nu)}{\mathrm{Br}(B_s^0 \to D_s^{(*)}\mu\nu)} \times \mathrm{Br}(\phi \to KK)\frac{\varepsilon(B_s^0 \to D_s^{(*)}D_s^{(*)})}{\varepsilon(B_s^0 \to D_s^{(*)}\mu\nu)}, \qquad (4.1)$$

where:

- $N(\mu\phi_2 D_s^{(*)})$ is the number of $B_s^0 \to D_s^{(*)}D_s^{(*)}$ candidates, estimated from a fit using a sample of events selected as the $(\mu\phi_2 D_s^{(*)})$ sample (see section 4.5.3);

- $N_{\rm bkg}$ is the number of background events contributing to the number, $N(\mu\phi_2 D_s^{(*)})$, of events extracted from the fit, estimated using MC and data;
- $N(\mu D_s^{(*)})$ is the number of $B_s^0 \to D_s^{(*)}\mu\nu X$ candidates, estimated from a fit using events in the $(\mu D_s^{(*)})$ sample (see section 4.5.2);
- $f(B_s^0 \to D_s^{(*)}\mu\nu)$ is the fraction of events from $N(\mu D_s^{(*)})$ to come from the decay $B_s^0 \to D_s^{(*)}\mu\nu X$ and not the background processes considered in section 4.4.2;
- The factor of two is due to the possible decays: $D_s^+ \to \phi_1\pi^+$, $D_s^- \to \phi_2\mu^-\nu$; and $D_s^- \to \phi_1\pi^-$, $D_s^+ \to \phi_2\mu^+\bar{\nu}$;
- $\mathrm{Br}(B_s^0 \to D_s^{(*)}D_s^{(*)})$ is the branching fraction value to be measured;
- $\mathrm{Br}(D_s \to \phi\mu\nu)$, $\mathrm{Br}(B_s^0 \to D_s^{(*)}\mu\nu)$, and $\mathrm{Br}(\phi \to KK)$ are values taken from the PDG [5]; and
- $\frac{\varepsilon(B_s^0 \to D_s^{(*)}D_s^{(*)})}{\varepsilon(B_s^0 \to D_s^{(*)}\mu\nu)}$ is the ratio of the reconstruction efficiencies of the two decay processes, as determined from MC.

A ratio R can be defined in terms of branching fractions as:

$$R = \frac{\mathrm{Br}(B_s^0 \to D_s^{(*)}D_s^{(*)}) \cdot \mathrm{Br}(D_s \to \phi\mu\nu)}{\mathrm{Br}(B_s^0 \to D_s^{(*)}\mu\nu)}. \tag{4.2}$$

The value of $\mathrm{Br}(B_s^0 \to D_s^{(*)}D_s^{(*)})$ is determined from the experimental extraction of R using Eq. 4.1, and branching fraction values from the PDG [5].

4.4 Background processes

The selected samples of events contain additional contributions to the desired signal components. As this analysis does not use particle identification, i.e. separating a pion from a kaon, background events can be produced when, for example, a pion is assigned the mass of a kaon, or a track passes close to a secondary vertex but does not originate from the decay of interest and

is assigned to the vertex. These backgrounds are called combinatoric backgrounds.

Some physical processes can imitate the decay of interest and their effect can be reduced using specific selection criteria. Using MC and data the level of contamination can be estimated. In this analysis the term "peaking background" is defined to include the decays $c\bar{c} \to \mu\nu D_s^{(*)}X$, $b\bar{b} \to \mu\nu D_s^{(*)}X$ originating from production close to the PV. Backgrounds with potential contributions to the two main decay channels are given below.

4.4.1 Background contributions to the $(\mu\phi_2 D_s^{(*)})$ sample

The sample of $(\mu\phi_2 D_s^{(*)})$ events contain contributions from the signal $B_s^0 \to D_s^{(*)}D_s^{(*)}$ decay, combinatorial background, and additional contributions from:

1. $B_{u,d} \to D_s^{(*)}D_s^{(*)}KX$;
2. $B_s^0 \to D_s^{(*)}D_s^{(*)}X$;
3. $B_s^0 \to D_s^{(*)}\mu\nu\phi$;
4. Peaking background;
5. $B_s^0 \to D_s^{(*)}\mu\nu$ and ϕ meson from fragmentation.

The contribution of these processes to the $(\mu\phi_2 D_s^{(*)})$ sample is given in section 4.12 on page 84.

4.4.2 Background contributions to the $(\mu D_s^{(*)})$ sample

The following processes, in addition to combinatorial background and the signal channel, were considered to contribute as to the $(\mu D_s^{(*)})$ sample:

1. $B^0 \to D_s^{(*)}D^{(*)}X$;
2. $B^{\pm} \to D_s^{(*)}D^{(*)}X$;

3. $B_s^0 \to D_s^{(*)} D_s^{(*)}$;

4. $B_s^0 \to D_s^{(*)} DX$;

5. Peaking background.

The contribution of these processes to the $(\mu D_s^{(*)})$ sample is given in section 4.11 on page 83.

4.5 Event selection

To make maximal use of the available statistics, no explicit trigger requirement was applied to select the event sample. However, the majority of events were collected from a suite of single-muon inclusive triggers. To reduce any bias from the lack of trigger requirement, the decay $B_s^0 \to D_s^{(*)} D_s^{(*)}$ was normalised to the decay of $B_s^0 \to D_s^{(*)} \mu\nu$ which has a similar final state. The MC simulations do not account for trigger effects, and possible differences between MC and data are taken into account by the reweighting procedure described in section 4.13. From the data collected at DØ, a set of selection criteria were made to obtain an initial "skim", or set of data, useful for b-physics analyses. The selection criteria required a muon to have:

- hits in at least the BC-layers of the muon detector;
- at least one hit in both the SMT and CFT;
- a track in the muon subdetector matched to a track in the central detector systems; and,
- $p_{\mathrm{T}}(\mu) > 1.5\,\mathrm{GeV}/c$.

This common skim [46] for the b-physics group at DØ was used as the initial dataset in this analysis to which further selections were then applied.

A preselection sample was produced, which identified $D_s(\phi_1\pi)$ candidates originating from the same primary vertex as a muon. The samples of $(\mu D_s^{(*)})$ and $(\mu\phi_2 D_s^{(*)})$ candidates were each obtained from this preselection sample. Motivation for some of the selection criteria was derived from previous b physics analyses, such as the selection criteria for the decay $D_s^{(*)} \to \mu\nu X$ [47] and for muons and ϕ mesons [48].

4.5.1 The preselection sample

All charged tracks were required to have at least two axial hits in both the SMT and CFT. For each event, at least one muon was required, as identified by the standard DØ algorithm described previously, with the additional requirements of $p_{\mathrm{T}} > 2\,\mathrm{GeV}/c$ and $p > 3\,\mathrm{GeV}/c$. The muon was required to have at least two hits in the BC layers of the muon system and be matched to a track in the central region of the DØ detector. Two oppositely-charged particles with $p_{\mathrm{T}} > 0.8\,\mathrm{GeV}/c$ were selected from all remaining particles and each assigned the mass of a kaon. The invariant mass of the (KK) system was required to be $1.01 < M(KK) < 1.03\,\mathrm{GeV}/c^2$, so as to be consistent with the mass ($1.019\,\mathrm{GeV}/c^2$ [5]) of a ϕ meson. As the decay of the ϕ_1 meson will be displaced from the PV it is possible to reduce background contamination by selecting kaon tracks with large impact parameter significance, as illustrated in Fig. 4.3. For each kaon candidate, axial[1] (δ_T) and stereo[2]

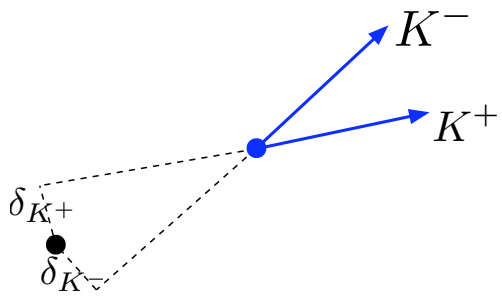

Figure 4.3: Impact parameter for the two kaons from a ϕ meson decay. Background is suppressed by requiring kaons that originate away from the primary vertex, hence possess a large impact parameter significance.

(δ_L) projections of the impact parameter were determined, along with the associated uncertainties ($\sigma(\delta_T), \sigma(\delta_L)$). The impact parameter significance S_K, defined as:

$$S_K = \left(\frac{\delta_T}{\sigma(\delta_T)}\right)^2 + \left(\frac{\delta_L}{\sigma(\delta_L)}\right)^2 \tag{4.3}$$

[1]Perpendicular to the beam direction.
[2]In the plane perpendicular to the beam direction.

was required to be $S_K > 4$ for both kaons. Each pair of kaons that satisfied these criteria was combined to form a common D_s vertex with a third particle of $p_{\mathrm{T}} > 1.0\,\mathrm{GeV}/c$, which was assigned the mass of a pion. The pion candidate and muon were required to have opposite charge. The χ^2 of the $D_s(\phi_1\pi)$ vertex fit, as defined in section 3.4.3, was required to be $\chi^2 < 16$.

The distance from the primary vertex to the $D_s(\phi_1\pi)$ decay vertex in the transverse plane $d_T^{D_\pi}$ was required to have significance $d_T^{D_\pi}/\sigma(d_T^{D_\pi}) > 4$. The angle α_T^D (illustrated in Fig. 4.4), defined as the angle between the $D_s(\phi_1\pi)$ momentum and the direction of the $D_s(\phi_1\pi)$ candidate from the PV to its decay vertex, was required to be $\cos\alpha_T^D > 0.9$. The distribution of $\cos\alpha_T^D$ for the signal sample $B_s^0 \to D_s^{(*)}D_s^{(*)}$ in MC is shown in Fig. 4.5. The use of this selection suppresses the number of combinations from tracks that are not associated with the correct signal decay mode.

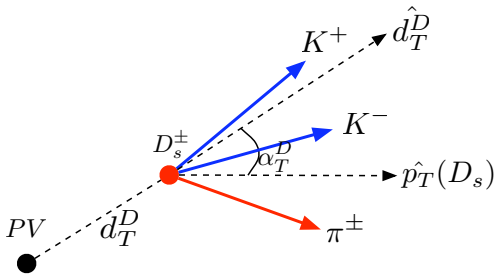

Figure 4.4: Illustration of the decay vertex of $D_s \to \phi_1\pi$. Symbols are defined in the text.

A helicity angle χ, defined as the angle between the momenta of the D_s candidate and a K meson in the (KK) centre of mass system. The decay of $D_s \to \phi_1\pi$ follows a $\cos^2\chi$ distribution, while for background $\cos\chi$ is expected to be flat, as shown in Fig. 4.6. To suppress background, the requirement $|\cos(\chi)| > 0.35$ was applied to all events. The motivation for the value 0.35 for this cut is derived from the following theoretical consideration. Under the assumption of a flat distribution in $\cos(\chi)$ for background and $\cos^2(\chi)$ for signal, the cut-value that maximises the figure-of-merit criterion $\mathrm{Signal}/\sqrt{\mathrm{Signal} + \mathrm{Background}}$ is found to be $|\cos(\chi)| \approx 0.35$ Events passing these selection requirements are referred to as the preselection sample, and this sample was used to form the initial selection for both the $(\mu D_s^{(*)})$ and

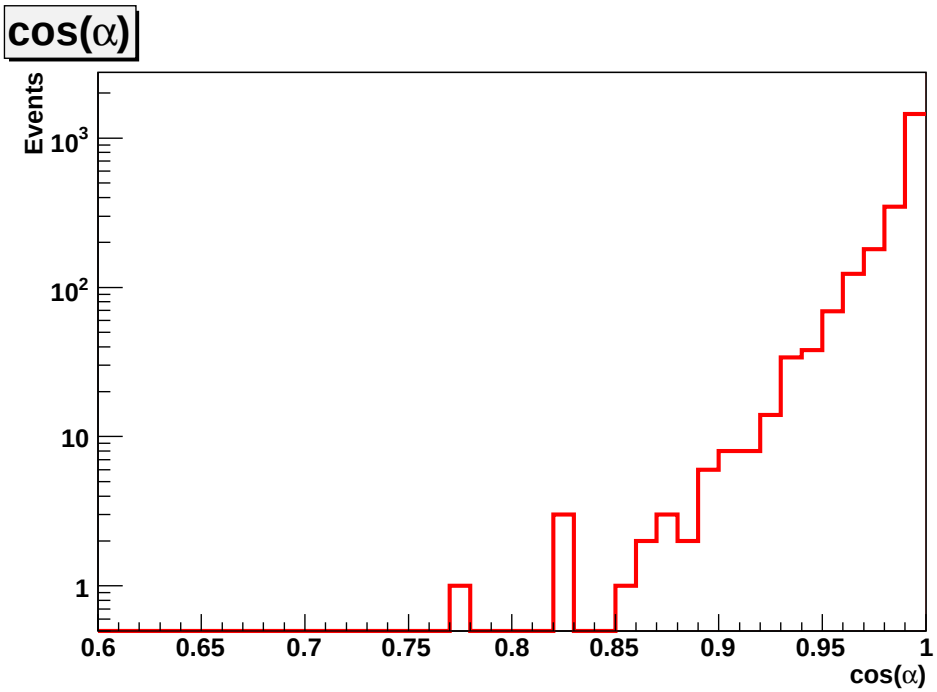

Figure 4.5: Normalised MC distribution of $\cos(\alpha_T^D)$ for the decay $B_s^0 \to D_s^{(*)} D_s^{(*)}$. Events passing the preselection criteria required $\cos(\alpha_T^D) > 0.9$.

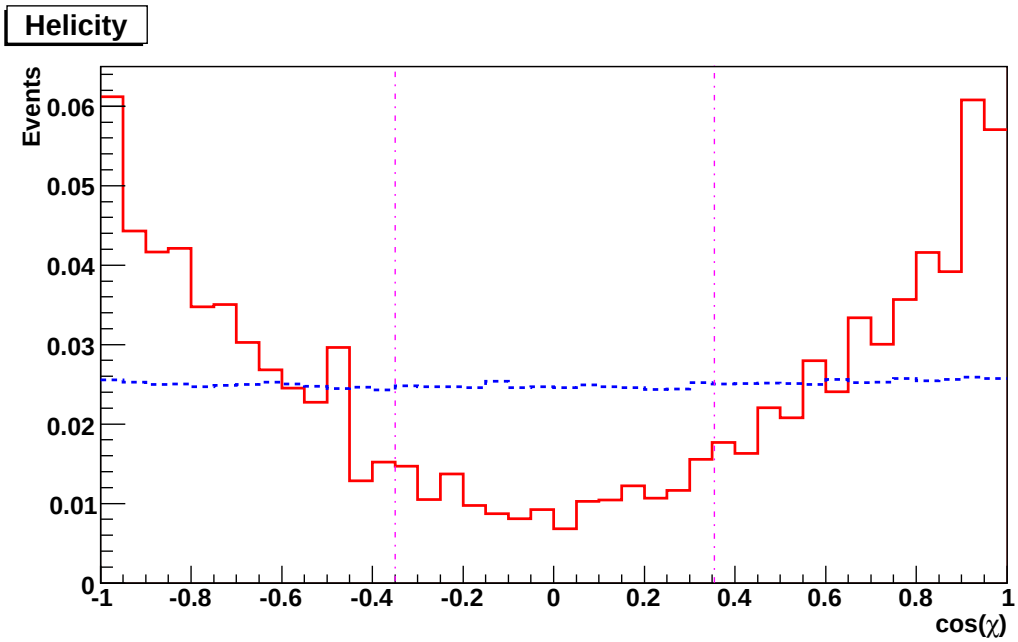

Figure 4.6: Normalised distributions of $\cos\chi$, where the helicity angle χ has been defined in section 4.5.1. The distribution in red (solid) is from the MC sample $B_s^0 \to D_s^{(*)} D_s^{(*)}$ and in blue (dotted) from background data. Events were rejected if their value of $\cos\chi$ was between the vertical dashed lines.

$(\mu\phi_2 D_s^{(*)})$ samples.

4.5.2 Selection of $B_s^0 \to D_s^{(*)}\mu\nu X$ candidates

To construct a $(\mu D_s^{(*)})$ candidate from the preselection sample, the muon and the $D_s(\phi_1\pi)$ candidate were required to form a common vertex with a vertex fit $\chi^2 < 16$. As the D_s meson is expected to decay further from the PV than the B_s^0 meson, it was allowed for $d_T^{D_\pi}$ to be less than d_T^B, the distance between the B_s^0 vertex and PV in the transverse plane, only if the distance d_T^{BD} between B_s^0 and D_s vertices was less than $2\sigma(d_T^{BD})$.

An isolation variable $\mathcal{I}(\mu D_s^{(*)})$ was defined:

$$\mathcal{I}(\mu D_s^{(*)}) = \frac{p^{\text{tot}}(\mu D_s^{(*)})}{p^{\text{tot}}(\mu D_s^{(*)}) + \sum p_i^{\text{tot}}}, \tag{4.4}$$

where $p^{\text{tot}}(\mu D_s^{(*)})$ is the total momentum of the $(\mu D_s^{(*)})$ system, and $\sum p_i^{\text{tot}}$ is the sum of momenta of all charged tracks not from the B_s^0 decay within a cone $\Delta\mathcal{R} = \sqrt{(\Delta\eta)^2 + (\Delta\phi)^2} < 0.5$. Here $\Delta\eta$ and $\Delta\phi$ are the pseudorapidity and azimuthal angle taken with respect to the direction of the B_s^0 candidate. The isolation was required to be $\mathcal{I}(\mu D_s^{(*)}) > 0.6$, which was motivated from MC. The distribution of isolation is shown in Fig. 4.7. The value of 0.6 used for the isolation cut was determined from the sample of $(\mu D_s^{(*)})$ events using the results of the fit for a range of isolation values. The optimal value chosen was based on the figure-of-merit value $N_{\text{Signal}}/\sqrt{N_{\text{Signal}} + N_{\text{Background}}}$ whilst ensuring this value was stable across a range. Table 4.5.2 gives the significance for a range of isolation values.

The Visible Proper Decay-Length (VPDL), defined as

$$\text{VPDL} = \frac{\vec{L}_{\text{T}} \cdot \vec{p}_{\text{T}}}{p_{\text{T}}^2} \cdot M(B_s^0), \tag{4.5}$$

was required to exceed $150\,\mu$m. Here, $\vec{L}_{\text{T}}$ is the displacement from the PV to the B_s^0 decay vertex in the transverse plane, and $M(B_s^0)$ is the mass ($5.366\,\text{GeV}/c^2$ [5]) of the B_s^0 meson.

The mass of the $(\mu D_s^{(*)})$ system was required to be $M(\mu D_s^{(*)}) < 5.2\,\text{GeV}/c^2$. Events that satisfied the above criteria are referred to as the

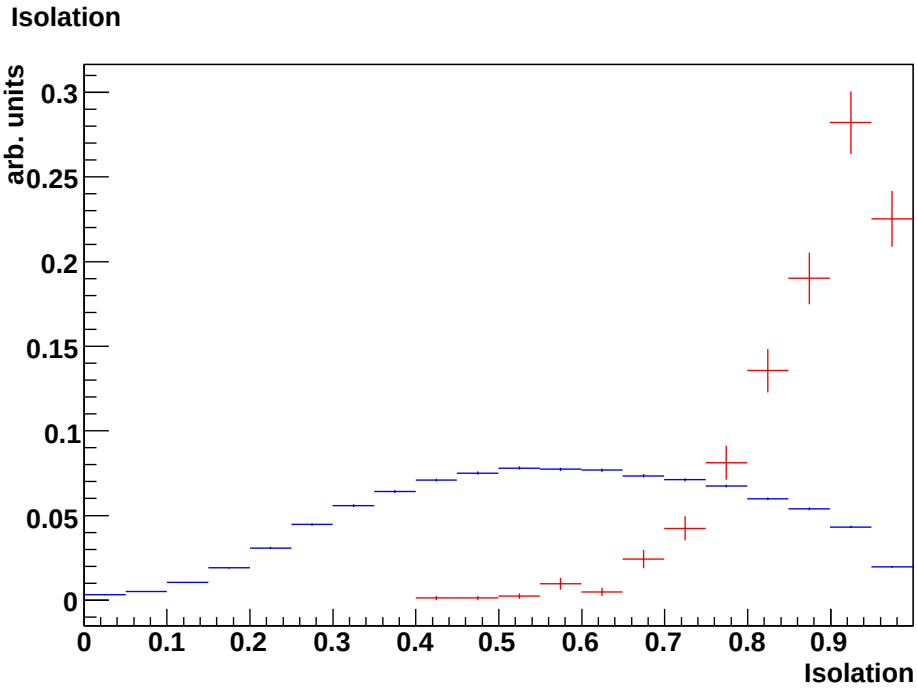

Figure 4.7: The distribution of the isolation variable is shown in red for the $B_s^0 \to D_s^{(*)} D_s^{(*)}$ MC sample, and in blue for a sample of background data. The relative normalisations are arbitrary. Events were selected with isolation values greater than 0.6.

Table 4.1: Significance values defined by $N_{\text{Signal}}/\sqrt{N_{\text{Signal}} + N_{\text{Background}}}$ from the fitted values to the $(\mu D_s^{(*)})$ sample.

Isolation cut value	Significance
0.4	52.5
0.5	52.9
0.6	52.9
0.7	52.4
0.8	49.7
0.9	42.8

$(\mu D_s^{(*)})$ sample and were used to estimate the number of $B_s^0 \to D_s^{(*)}\mu\nu$ events, as discussed in section 4.6.

The mass spectrum of the (KK) system in the signal window of the $D_s(\phi_1\pi)$ is shown in Fig. 4.8. The number of ϕ_1 meson candidates is estimated as 22100 ± 800 events. Figure 4.9 shows the mass of the $(\phi_1\pi)$

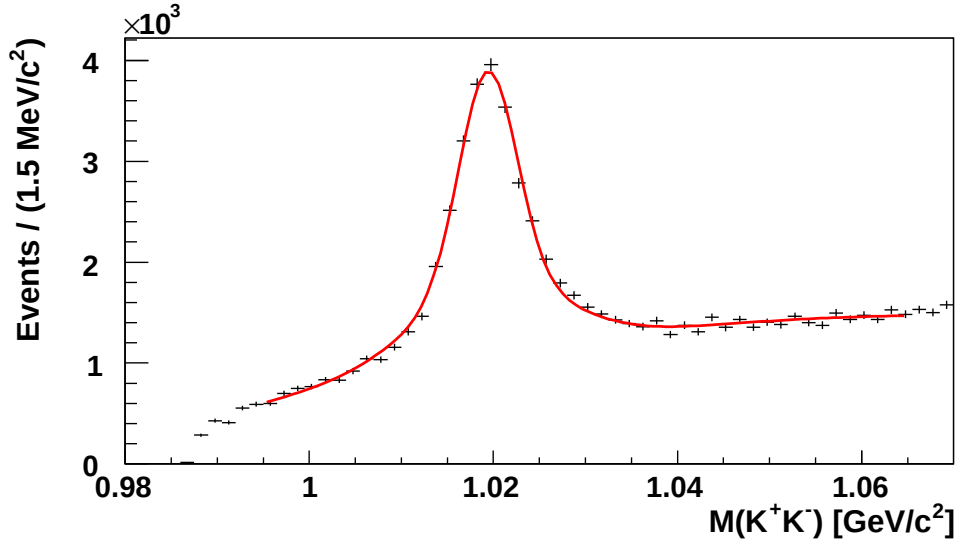

Figure 4.8: Invariant mass $M(KK)$ distribution for the $(\mu D_s^{(*)})$ sample in the mass window $1.92 < M(\phi_1\pi) < 2.00\,\mathrm{GeV}/c^2$. The fit is given by a second-order polynomial to parameterise the background, and a double Gaussian for the ϕ meson mass peak.

spectrum. The $D^{\pm}$ and D_s peaks are clearly visible. The results of the fit (described in section 4.6.2) estimate the number of events in the D_s mass peak as 17670 ± 230 events, and 5700 ± 200 events for the $D^{\pm}$ mass peak.

4.5.3 Selection of $B_s^0 \to D_s^{(*)} D_s^{(*)} X$ candidates

From the preselection sample of events, an additional ϕ meson was required. The selection criteria for this second ϕ_2 meson was the same as the first ϕ_1 meson, however a wider invariant mass range of $0.99 < M(KK) < 1.07\,\mathrm{GeV}/c^2$ was used. This wider window was necessary to estimate the background contribution under the ϕ_2 peak in the fitting procedure, described in section 4.7.

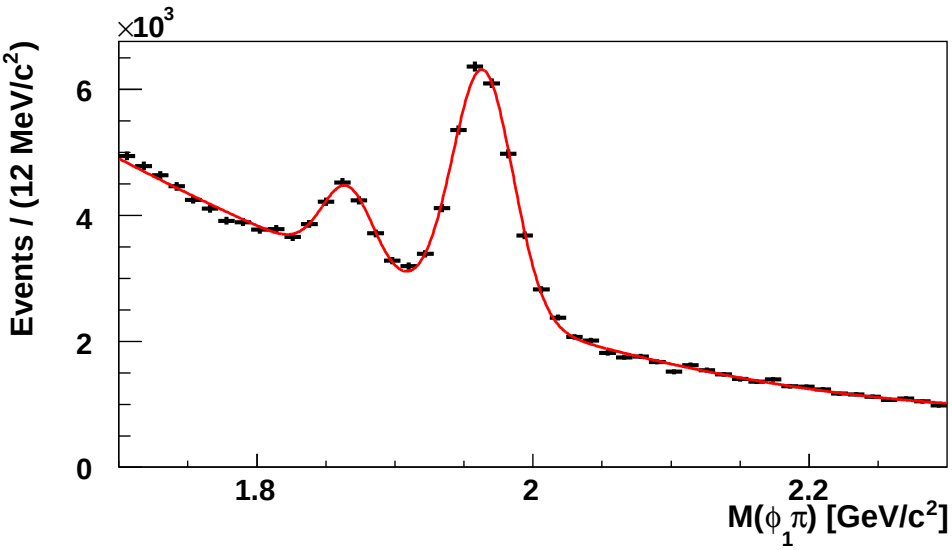

Figure 4.9: Invariant mass $M(\phi_1\pi)$ distribution for the $(\mu D_s^{(*)})$ sample in the mass window $1.01 < M(K^+K^-) < 1.03\,\mathrm{GeV}/c^2$. The fit is a Gaussian for each of the mass peaks, and a second-order polynomial to parameterise the background.

The two additional kaons and the muon were required to form a common $D_s(\phi_2\mu)$ vertex, with the χ^2 of the vertex fit $\chi^2 < 16$. The significance for $d_T^{D_\mu}$, the distance in the transverse plane between the PV and the $D_s(\phi_2\mu)$ decay vertex, was required to be $d_T^{D_\mu}/\sigma(d_T^{D_\mu}) > 1$.

As the decay $D_s \to \phi_2\mu\nu$ is only partially reconstructed, the mass of the $(\phi_2\mu)$ system cannot exceed that of the D_s meson, while possible background processes may have a higher $(\phi_2\mu)$ invariant mass. To suppress background, the mass of the $(\phi_2\mu)$ system was required to be $1.2 < M(\phi_2\mu) < 1.85\,\mathrm{GeV}/c^2$. Figure 4.10 displays the $(\phi_2\mu)$ invariant mass distributions in MC for $B_s^0 \to D_s^{(*)}D_s^{(*)}$ and a background process $B_s^0 \to D_s^{(*)}\mu\nu\phi$.

The $D_s(\phi_1\pi)$ and $D_s(\phi_2\mu)$ candidates were required to form a common B_s^0 vertex with the χ^2 of the vertex fit $\chi^2 < 16$. The distance d_T^B in the transverse plane between the PV and the decay vertex of the B_s^0 meson was allowed to exceed the distance $d_T^{D_{\pi,\mu}}$ of either of the two D_s mesons, providing $d_T^{D_{\pi,\mu}B} > 2\sigma(d_T^{D_{\pi,\mu}B})$. An isolation $\mathcal{I}(\mu\phi_2 D_s^{(*)})$ was defined as in Eq. 4.4, however the sum $\sum p_i^{\mathrm{tot}}$ also excluded the two kaons from the additional ϕ_2 meson decay. It was required that $\mathcal{I}(\mu\phi_2 D_s^{(*)}) > 0.6$. The VPDL, as defined

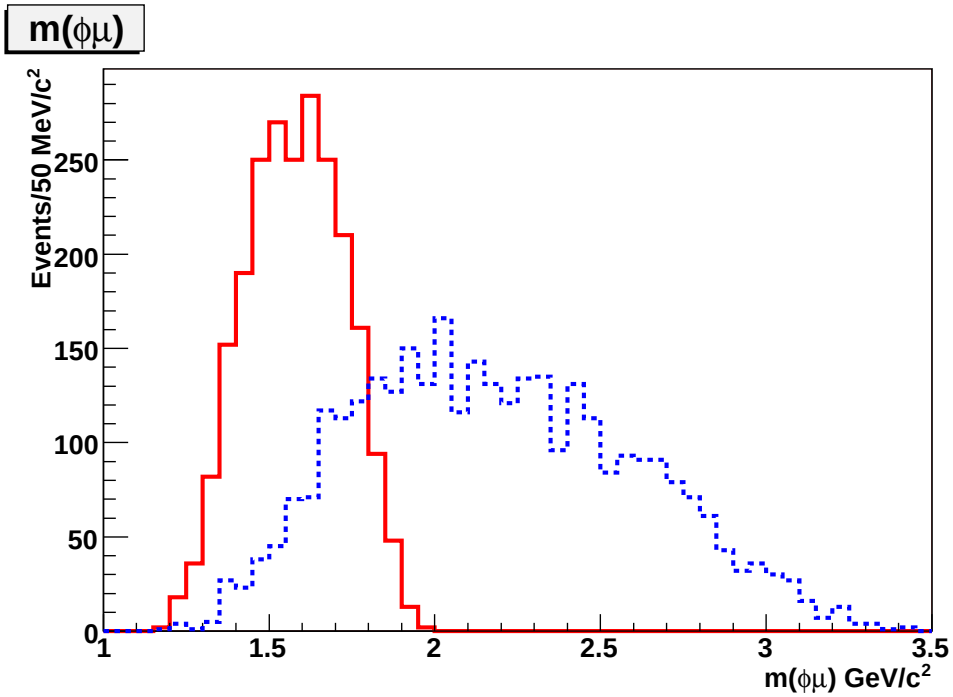

Figure 4.10: Invariant mass distributions of $M(\phi_2\mu)$ for the MC processes $B_s^0 \to D_s^{(*)}D_s^{(*)}$ shown in red (solid), and the background process $B_s^0 \to D_s^{(*)}\mu\nu\phi$ given in blue (dotted). The two histograms are shown normalised to the same area.

in Eq. 4.5, was required to exceed $150\,\mu$m.

The mass of the $(\mu\phi_2 D_s^{(*)})$ system was required to be $M(\mu\phi_2 D_s^{(*)}) < 5.2\,\mathrm{GeV}/c^2$. Events satisfying these criteria are referred to as the $(\mu\phi_2 D_s^{(*)})$ sample and were used to extract the number of $B_s^0 \to D_s^{(*)} D_s^{(*)}$ events $N(\mu\phi_2 D_s^{(*)})$, as described in section 4.7. In Table 4.2 a summary is displayed of the selection criteria for the final samples.

4.6 Extracting $N(\mu D_s^{(*)})$

Binned likelihood fits to the $(\mu D_s^{(*)})$ sample were performed to extract $N(\mu D_s^{(*)})$, the number of events in the $D_s \to \phi_1\pi$ mass peak, and the mass and width parameters of the ϕ meson. The fits were made using the ROOT [49] analysis framework with the minimisation class TMinuit, which had been derived from [50].

4.6.1 Invariant (KK) mass distribution

The (KK) invariant mass distribution was fitted in order to extract the measured mass and width values of the ϕ meson. The function used is given by

$$\mathcal{F}_{KK}(m) = N_{KK} \cdot \left\{ f_p \left[\frac{\hat{h}}{\sqrt{2\pi}\hat{\sigma}_n} \mathrm{e}^{-\frac{1}{2}\left(\frac{m-\hat{m}}{\hat{\sigma}_n}\right)^2} + \frac{1-\hat{h}}{\sqrt{2\pi}\hat{\sigma}_w} \mathrm{e}^{-\frac{1}{2}\left(\frac{m-\hat{m}}{\hat{\sigma}_w}\right)^2} \right] + (1-f_p)\left[\frac{1}{m_{\max}-m_{\min}} + b_{KK}m' + c_{KK}(m'^2 - \frac{1}{3}) \right] \right\}, \quad (4.6)$$

where:

- N_{KK} is normalised to the number of events used in the fit;
- f_p is the fraction of all events that contribute to the ϕ mass peak;
- $\hat{h}$ is the fraction of events in the mass peak from the narrow Gaussian;
- b_{KK} and c_{KK} are background parameters determined by the fit;
- $m_{\min}, m_{\max}$ are the minimum and maximum values of the range over which the fit is performed; and

Table 4.2: Summary of selection criteria used. Nomenclature is defined in the text.

Particle	Selection Criterion
All tracks:	Number of axial hits in SMT$\geq$ 2
	Number of axial hits in CFT$\geq$ 2
Muon:	$p_{\mathrm{T}} > 2$ GeV/c
	p > 3 GeV/c
	Track matched to central region
Pion:	$p_{\mathrm{T}} > 1.0$ GeV/c
	Opposite charge combination $(\mu^{\pm}, \pi^{\mp})$
$K^{\pm}$:	$p_{\mathrm{T}} > 0.8$ GeV/c
ϕ:	Both kaons to have $S_K > 4$, as defined in Eq. (4.3)
	Opposite charge kaon combination
ϕ_1 from $D_s \to \phi_1\pi$:	$1.01 < m(KK) < 1.03$ GeV/c^2
ϕ_2 from $D_s \to \phi_2\mu$:	$0.99 < m(KK) < 1.07$ GeV/c^2
$D_s \to \phi_1\pi$:	$1.7 < m(\phi_1\pi) < 2.3$ GeV/c
	χ^2(vertex)< 16
	$d_T^{D_\pi}/\sigma(d_T^{D_\pi}) > 4$
	$\cos(\alpha_T^D) > 0.9$
	Helicity between D_s and K, $\lvert\cos(\chi)\rvert > 0.35$
$D_s \to \phi_2\mu\nu$	$1.2 < m(\phi_2\mu) < 1.85$ GeV/c^2
	χ^2(vertex)< 16
	$d_T^{D_\mu}/\sigma(d_T^{D_\mu}) > 1$
$B_s^0 \to \mu D_s$:	χ^2(B vertex)< 16
	$m(\mu D_s) < 5.2$ GeV/c^2
	$d_T^B < d_T^D$ or $d_T^{BD} < 2 \cdot \sigma(d_T^{BD})$
	$L(\mu D_s) = M(B_s) \cdot d_T^B/p_{\mathrm{T}}(\mu D_s) > 150\mu$m
	$\mathcal{I} > 0.6$
$B_s^0 \to \mu\phi_2 D_s$:	χ^2(B vertex)< 16
	$4.3 < m(\mu\phi_2 D_s) < 5.2$ GeV/c^2
	$d_T^B < d_T^D$ or $d_T^{BD} < 2 \cdot \sigma(d_T^{BD})$
	$L(\mu\phi_2 D_s) = M(B_s) \cdot d_T^B/p_{\mathrm{T}}(\mu\phi_2 D_s) > 150\mu$m
	$\mathcal{I} > 0.6$

- $$m' = 2\frac{m - m_{\rm c}}{m_{\rm max} - m_{\rm min}}, \quad \text{where} \tag{4.7}$$
$$m_{\rm c} = \frac{m_{\rm max} + m_{\rm min}}{2}. \tag{4.8}$$

Equation 4.6 describes the ϕ meson mass peak with a double Gaussian and second-order polynomial to parameterise the background. This decision was motivated from the analysis [47], and its effect on the result is tested in section 4.8.2. To increase stability of the fitting procedure, the mass variable m in the second-order background polynomial was transformed to the range $[-1, 1]$ using the expressions defined in Eqs. 4.7 and 4.8. The result of the fit is superimposed as a solid red curve in Fig. 4.8 on page 62. The results of the fit gave: $\hat{m}_\phi = 1.0194 \pm 0.0001\,\text{GeV}/c^2$; $\hat{\sigma}_n = 3.2 \pm 0.1\,\text{MeV}/c^2$; $\hat{\sigma}_w = 7.9 \pm 0.9\,\text{MeV}/c^2$; $\hat{h} = 0.56 \pm 0.04$.

4.6.2 $(\phi_1\pi)$ mass distribution

The function fitted to the $(\phi_1\pi)$ mass distribution is described by Eq. 4.9 with a single Gaussian for each of the $D^\pm$ and D_s mass peaks, and a second-order polynomial to parameterise the background.

$$\begin{aligned}\mathcal{F}_{\phi\pi}(m) &= \frac{N_{D^+}}{\sqrt{2\pi}\hat{\sigma}_{D^+}} \exp\left\{-\frac{1}{2}\left(\frac{m - \hat{m}_{D^+}}{\hat{\sigma}_{D^+}}\right)^2\right\} \\ &+ \frac{N_{D_s}}{\sqrt{2\pi}\hat{\sigma}_{D_s}} \exp\left\{-\frac{1}{2}\left(\frac{m - \hat{m}_{D_s}}{\hat{\sigma}_{D_s}}\right)^2\right\} \\ &+ a_{\phi\pi} + b_{\phi\pi} m + c_{\phi\pi} m^2. \end{aligned} \tag{4.9}$$

Here, N_{D^+} and N_{D_s} are the normalisation constants for the D^+ and D_s peaks respectively. The result of the fit is superimposed in Fig. 4.9 on page. 63. The results of the fit gave: $\hat{m}_{D_s} = 1.9637 \pm 0.0003\,\text{GeV}/c^2$; $\hat{\sigma}_{D_s} = 21.9 \pm 0.3\,\text{MeV}/c^2$; $\hat{m}_{D^+} = 1.8658 \pm 0.0008\,\text{GeV}/c^2$; $\hat{\sigma}_{D^+} = 18.4 \pm 0.9\,\text{MeV}/c^2$;

From the fit, the number of events in the D_s mass peak is estimated as:

$$N(\mu D_s^{(*)}) = 17670 \pm 230 \ \text{ events}. \tag{4.10}$$

The mass peak positions, widths, and fraction $\hat{h}$ extracted from the two previous fits are used as fixed inputs into the fitting procedure described in

section 4.7 to estimate the number of $(\mu\phi_2 D_s^{(*)})$ events.

4.7 Extracting $N(\mu\phi_2 D_s^{(*)})$

A two-dimensional unbinned log-likelihood fit was performed on the $(\mu\phi_2 D_s^{(*)})$ sample. The invariant masses of $(\phi_1\pi)$ from $D_s(\phi_1\pi)$, and (KK) from $D_s(\phi_2\mu)$ were input into the fit, as fitting the two masses on an event-by-event basis allows for a better estimation of the sample composition. Extracted from the fit were the fractions of:

1. f_s, events from correlated (joint) signal production of $D_s(\phi_1\pi)$ mesons with ϕ_2 mesons from the decay of $D_s(\phi_2\mu)$;

2. f_D, events with a reconstructed $(\phi_1\pi)$ meson in the mass peak of a $D_s(\phi_1\pi)$ meson without the joint production of a ϕ_2 meson from $D_s(\phi_2\mu)$ mesons decay (i.e., uncorrelated);

3. f_ϕ, events with a reconstructed ϕ_2 meson from $D_s(\phi_2\mu)$ without the joint production of a $D_s(\phi_1\pi)$ meson; and,

4. combinatorial background.

In case one, a $D_s(\phi_1\pi)$ meson is reconstructed (i.e. in the mass peak of a D_s meson) from the decay $D_s \to \phi_1\pi$, jointly with the reconstruction of a ϕ_2 meson from the decay $D_s \to \phi_2\mu\nu$. In the second case, whilst a $D_s(\phi_1\pi)$ meson is reconstructed from the decay $D_s \to \phi_1\pi$, the mass of the (KK) system is not in the mass peak of the ϕ_2 meson, and these events contribute to the background. Similarly in case three, even though the $D_s(\phi_1\pi)$ is reconstructed, the (KK) mass is not in the mass peak of the ϕ_2 meson. In case four, the $(\phi_1\pi)$ and (KK) masses are reconstructed outside of their respective $D_s(\phi_1\pi)$ and ϕ_2 mass peaks. These events form the combinatorial background.

The (KK) distribution was modelled by a double Gaussian for the ϕ mass peak and a second-order polynomial to parameterise the background. The $(\phi_1\pi)$ distribution was modelled by a Gaussian to describe the D_s mass peak and a second-order polynomial to parameterise the background. No $D^\pm$ peak is included in the function, however it is included as a cross-check

as described in section 4.8.4. The mass peaks and widths were fixed to the values extracted from the fits of the $(\mu D_s^{(*)})$ sample. The likelihood function $\mathcal{L}$ is given by

$$\mathcal{L} = \prod_i \mathcal{F}^i, \tag{4.11}$$

where the index i runs over the total number of events $N_{(\mu\phi_2 D_s^{(*)})}$ of the $(\mu\phi_2 D_s^{(*)})$ sample, and the PDF $\mathcal{F}$ is defined as

$$\begin{aligned}\mathcal{F}(M_D, M_\phi) = & f_s \mathcal{S}_D(M_D)\mathcal{S}_\phi(M_\phi) \\ & + f_\phi \mathcal{B}(M_D, a_D, b_D)\mathcal{S}_\phi(M_\phi) \\ & + f_D \mathcal{S}_D(M_D)\mathcal{B}(M_\phi, a_\phi, b_\phi) \\ & + (1 - f_s - f_D - f_\phi)\, \mathcal{B}(M_D, a_D, b_D)\mathcal{B}(M_\phi, a_\phi, b_\phi),\end{aligned} \tag{4.12}$$

where

$$\mathcal{S}_D(m) = \frac{1}{\sqrt{2\pi}\hat{\sigma}_{D_s}} \exp\left\{-\frac{1}{2}\left(\frac{m - \hat{m}_{D_s}}{\hat{\sigma}_{D_s}}\right)^2\right\}, \tag{4.13}$$

$$\begin{aligned}\mathcal{S}_\phi(m) = & \frac{\hat{h}}{\sqrt{2\pi}\hat{\sigma}_n} \exp\left\{-\frac{1}{2}\left(\frac{m - \hat{m}_\phi}{\hat{\sigma}_n}\right)^2\right\} \\ & + \frac{1 - \hat{h}}{\sqrt{2\pi}\hat{\sigma}_w} \exp\left\{-\frac{1}{2}\left(\frac{m - \hat{m}_\phi}{\hat{\sigma}_w}\right)^2\right\},\end{aligned} \tag{4.14}$$

$$\mathcal{B}(m, a, b) = \frac{1}{m_{\max} - m_{\min}} + am' + b(m'^2 - \frac{1}{3}), \tag{4.15}$$

where m' is defined in Eq. 4.7. In the fit, the values that $f_x\{x = s, D, \phi\}$ could take were constrained to be in the range $[0, 1]$. The number of signal events $N(\mu\phi_2 D_s^{(*)})$ was determined from

$$N(\mu\phi_2 D_s^{(*)}) = f_s N_{\text{cand}}. \tag{4.16}$$

From the $N_{\text{cand}} = 341$ events included in the fit,

$$N(\mu\phi_2 D_s^{(*)}) = 13.4^{+6.6}_{-6.0} \text{ events} \tag{4.17}$$

are estimated.

To illustrate the results of the fit, all events were separated into signal and sideband regions according to invariant mass, as defined by Table 4.7. For each of the mass distributions $(\phi_1\pi)$ and (KK), the data were split into two histograms, separated by whether the mass (KK) or $(\phi_1\pi)$ of the other system was in the signal or sideband region. The fit results were projected onto one-dimension by integrating out the other mass over its signal or sideband mass range, and are shown as the superimposed curves in Figs. 4.11 and 4.12.

Table 4.3: The mass ranges defining the signal and sideband regions used in projecting the result of the unbinned log-likelihood fitting procedure. Events in the low and high sideband regions are combined.

Mass	Region	Range
$(\phi_1\pi)$	Sideband low	$1.7 < M(\phi_1\pi) < 1.92\,\mathrm{GeV}/c^2$
$(\phi_1\pi)$	Signal	$1.92 < M(\phi_1\pi) < 2.0\,\mathrm{GeV}/c^2$
$(\phi_1\pi)$	Sideband high	$2.0 < M(\phi_1\pi) < 2.3\,\mathrm{GeV}/c^2$
(KK)	Sideband low	$0.99 < M(KK) < 1.01\,\mathrm{GeV}/c^2$
(KK)	Signal	$1.01 < M(KK) < 1.03\,\mathrm{GeV}/c^2$
(KK)	Sideband high	$1.03 < M(KK) < 1.07\,\mathrm{GeV}/c^2$

4.8 Cross-checks

To check the results of the unbinned log-likelihood fitting procedure described in section 4.7 the following cross-check procedures were employed.

4.8.1 Binned fit to the $(\mu\phi_2 D_s^{(*)})$ sample

One method to check the unbinned fitting procedure is to return to a binned-fit for comparison. In this case, in each mass distribution signal and sideband regions were defined, given in Tables 4.4 and 4.5, and one-dimensional fits performed for each mass. For the $(\phi_1\pi)$ mass, events were separated into two samples according to whether the (KK) mass was in its signal or sideband region. A binned likelihood fit was performed to the two (signal and

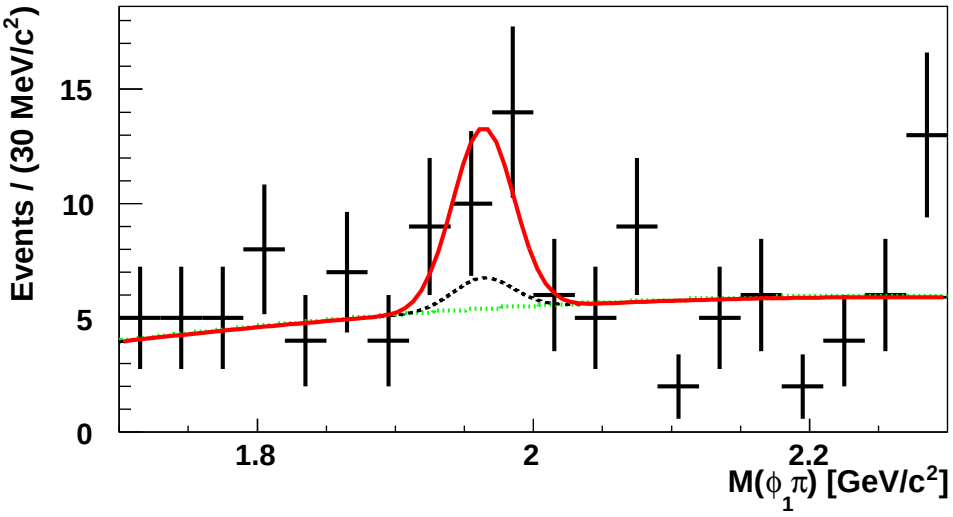

(a)

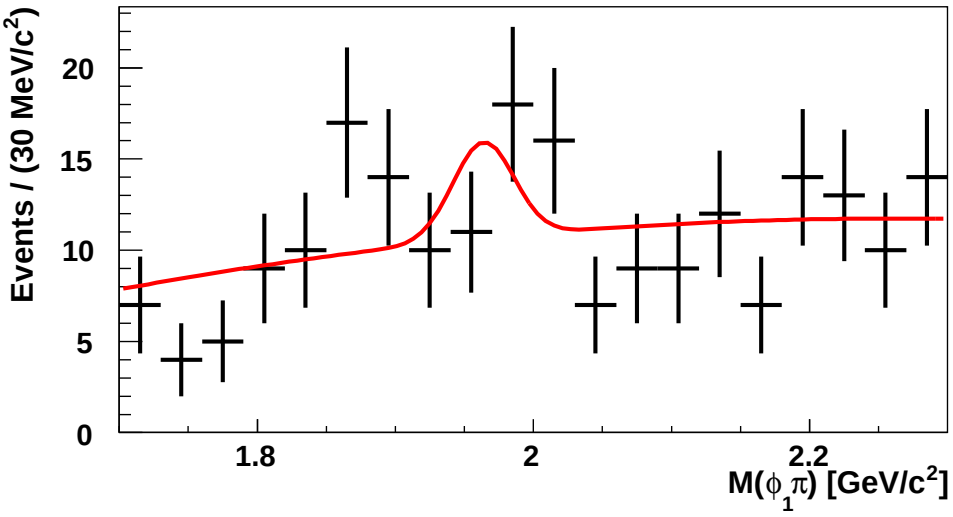

(b)

Figure 4.11: Invariant mass plot of $(\phi_1\pi)$ distribution for (a) events from the (KK) signal region, and (b) events in the (KK) sideband mass window. The solid curve (red) displayed in the plot corresponds to the fitted result of the unbinned log-likelihood fit projected into the different mass regions. The dotted curves are projections of background contributions for the polynomial (green) and uncorrelated (black) D_s production.

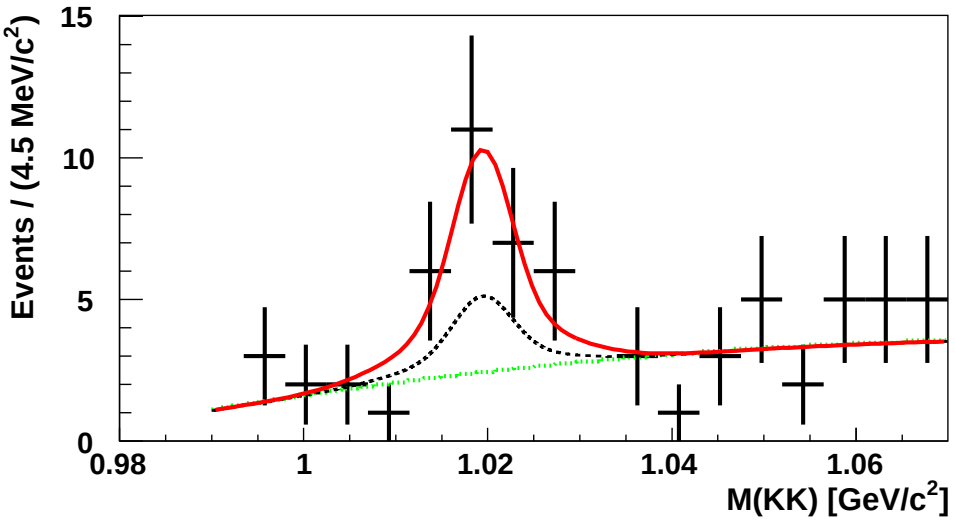

(a)

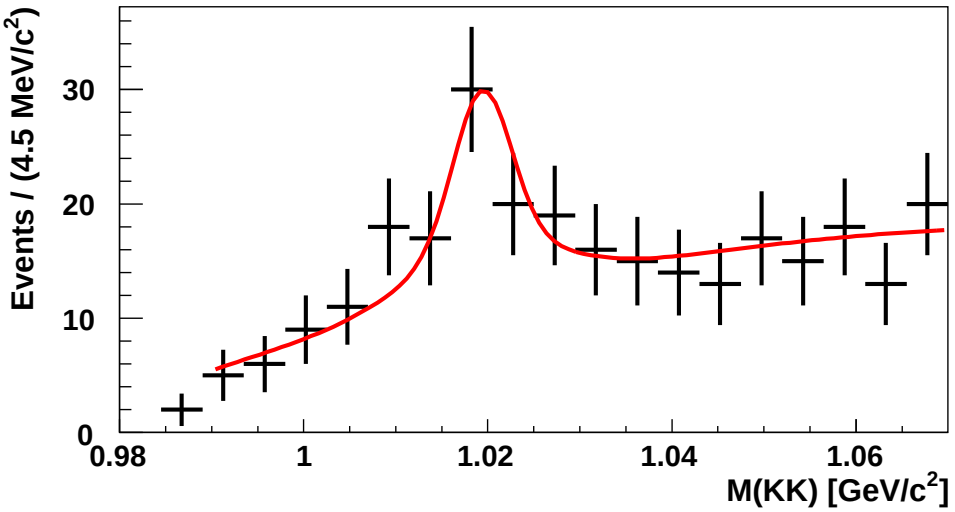

(b)

Figure 4.12: Invariant mass plot of the (KK) distribution for $D_s \to \phi_2\mu\nu$ projected into the $(\phi_1\pi)$ (a) signal region, and (b) sideband region. The superimposed solid curves (red) are projections from the unbinned log-likelihood fit into the different mass regions. The dotted curves are the polynomial (green) and uncorrelated (black) ϕ_2 meson background contributions.

Table 4.4: Mass window ranges of M($\phi_1\pi$) for the estimate of signal candidates from the mass of ϕ_2 from $D_s \to \phi_2\mu\nu$.

Region	Mass window
Sideband low	$1.72 < M(\phi_1\pi) < 1.86\,\mathrm{GeV}/c^2$
Signal	$1.92 < M(\phi_1\pi) < 2.0\,\mathrm{GeV}/c^2$
Sideband high	$2.06 < M(\phi_1\pi) < 2.2\,\mathrm{GeV}/c^2$

Table 4.5: Mass window ranges of $M(KK)$ from $\mathrm{D_s} \to \phi_2\mu$ for the estimate of signal candidates from the mass of M($\phi_1\pi$).

Region	Mass window
Sideband low	$0.995 < M(KK) < 1.005\,\mathrm{GeV}/c^2$
Signal	$1.01 < M(KK) < 1.03\,\mathrm{GeV}/c^2$
Sideband high	$1.035 < M(KK) < 1.045\,\mathrm{GeV}/c^2$

sideband) samples to give the number of events in the D_S mass peak defined as N_{signal} and N_{sideband}. Sideband subtraction was then performed using

$$N(\mu\phi D_s^{(*)}) = N_{\mathrm{signal}} - N_{\mathrm{sideband}} A_{\mathrm{signal}}/A_{\mathrm{sideband}}, \tag{4.18}$$

where A_{signal} and A_{sideband} are the areas under a fitted background curve for the signal and sideband regions respectively of the (KK) mass distribution. An identical procedure was performed for the (KK) mass distribution, using the $(\phi_1\pi)$ mass distribution for the signal and sideband separation regions. The mass distributions and corresponding fit results are shown in Figs. 4.13 and 4.14.

For the $(\phi_1\pi)$ and (KK) mass distributions, the fits yield

$$N(\mu\phi_2 D_s^{(*)}) = \begin{cases} 6.6 \pm 8.4 & \text{from the fit to } (\phi_1\pi), \\ 18.1 \pm 8.3 & \text{from the fit to } (KK). \end{cases} \tag{4.19}$$

These numbers are self-consistent and compatible with the unbinned log-likelihood fit result of Eq. 4.17. As the binned fit is unable to separate the uncorrelated background contributions, an increased yield is expected.

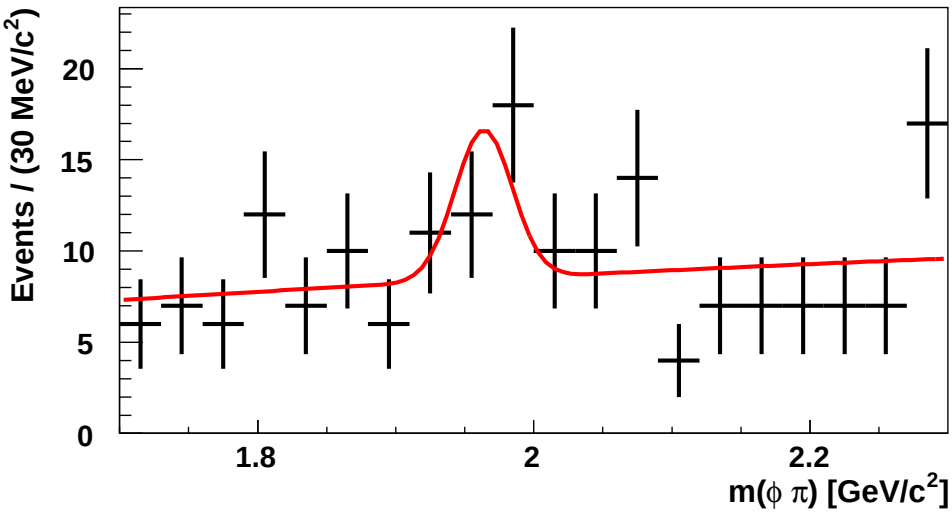

(a)

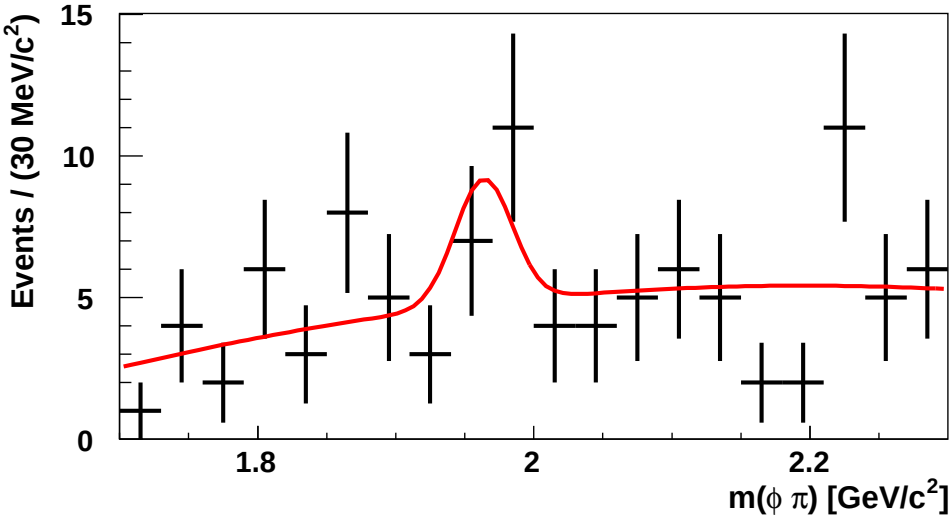

(b)

Figure 4.13: The resulting binned fit for the $(\mu\phi_2 D_s^{(*)})$ system is shown for the $(\phi_1\pi)$ mass spectrum for (a) (KK) signal and (b) sideband regions.

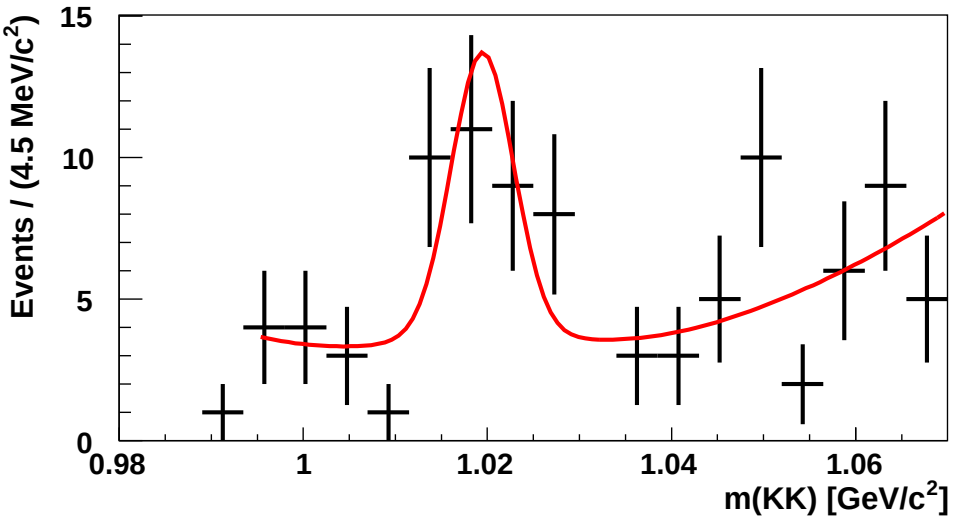

(a)

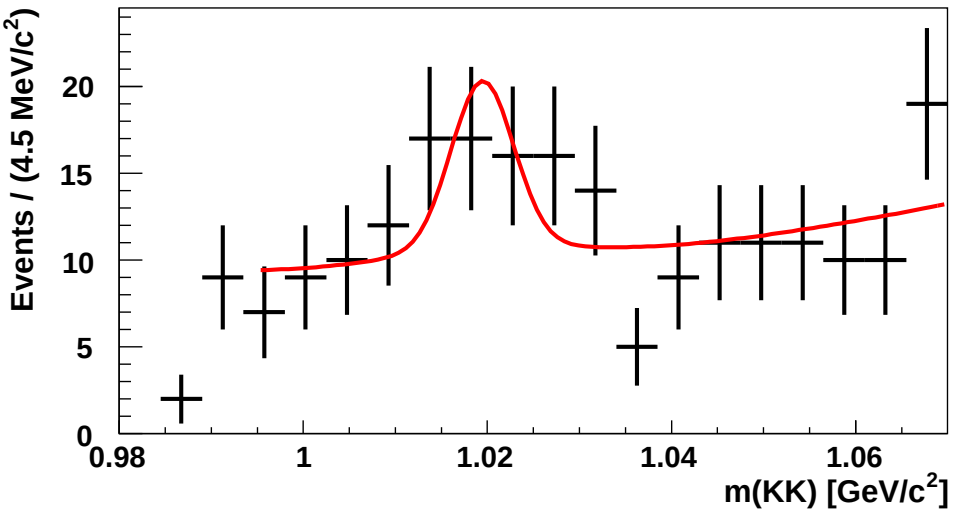

(b)

Figure 4.14: The resulting binned fit for the (KK) mass spectrum from the $(\phi_2\mu)$ system in the $(\mu\phi_2 D_s^{(*)})$ signal (a) and sideband (b) regions.

4.8.2 Single Gaussian to describe ϕ meson mass peak

The double Gaussian used in the fitting procedure was replaced by a single Gaussian and the full fitting procedure repeated. From the log-likelihood fit $13.6^{+6.1}_{-5.5}$ events were estimated, consistent with the double Gaussian fit.

4.8.3 Same-sign ($\mu^+\phi_2 D_s^{(*)+}$) sample

A sample of events were selected with identical criteria to the ($\mu\phi_2 D_s^{(*)}$) sample with the exception that the muon and $D_s(\phi_1\pi)$ candidate were required to have the same-sign charge. From the log-likelihood fit to this ($\mu^+\phi_2 D_s^{(*)+}$) sample, zero events are estimated with an upper limit of 6.9 events (68% CL).

4.8.4 Addition of a D^+ meson mass peak

The possibility of a fraction f_{D^+} of $D^+ \to \phi_1\pi^+$ decays in the ($\mu\phi_2 D_s^{(*)}$) sample was also considered. The term

$$f_{D^\pm} S_D(M_D)\mathcal{B}(M_\phi, a_\phi, b_\phi) \tag{4.20}$$

was added to log-likelihood fit and the combinatoric background fraction altered to $(1 - f_s - f_D - f_{D^+} - f_\phi)$. Using this modified PDF the log-likelihood fit yielded $N(\mu\phi_2 D_s^{(*)}) = 13.8^{+6.6}_{-6.0}$, consistent with Eq. 4.17. The difference between these two values was used as an estimate of uncertainty due to the fitting procedure and is included as a systematic, and is discussed in section 5.3. The fit projections are shown in Figs. 4.15 and 4.16.

4.8.5 Lower limit of $M(\mu\phi_2 D_s^{(*)})$

In Fig. 4.17, the MC distribution has been scaled to the fitted number of signal events and superimposed onto the $M(\mu\phi_2 D_s^{(*)})$ data distribution. As a further consistency check, the lower mass $M(\mu\phi_2 D_s^{(*)})$ was increased from $4.3\,\mathrm{GeV}/c^2$ to $4.7\,\mathrm{GeV}/c^2$ and the resulting distributions shown in Figs. 4.18 and 4.19. As statistics are low, simple event counting was used by subtracting events in sidebands from the signal region and $\sim 5 \pm 3$ events were found.

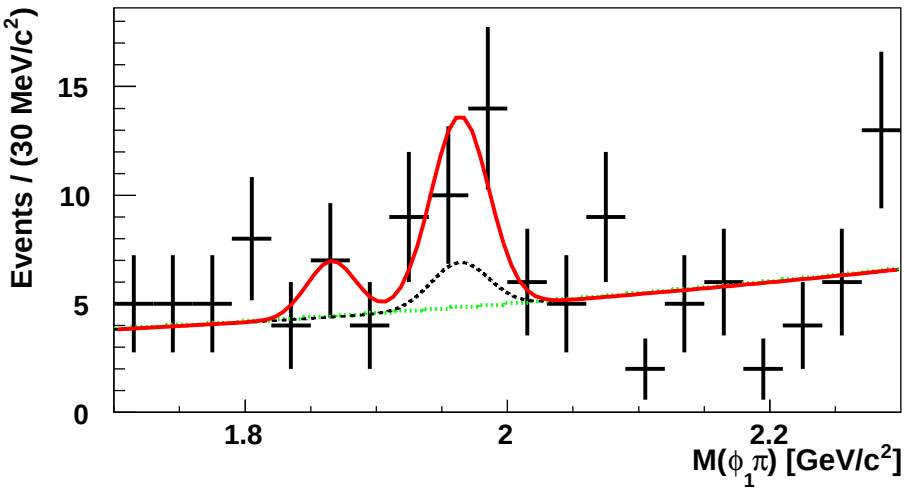

(a)

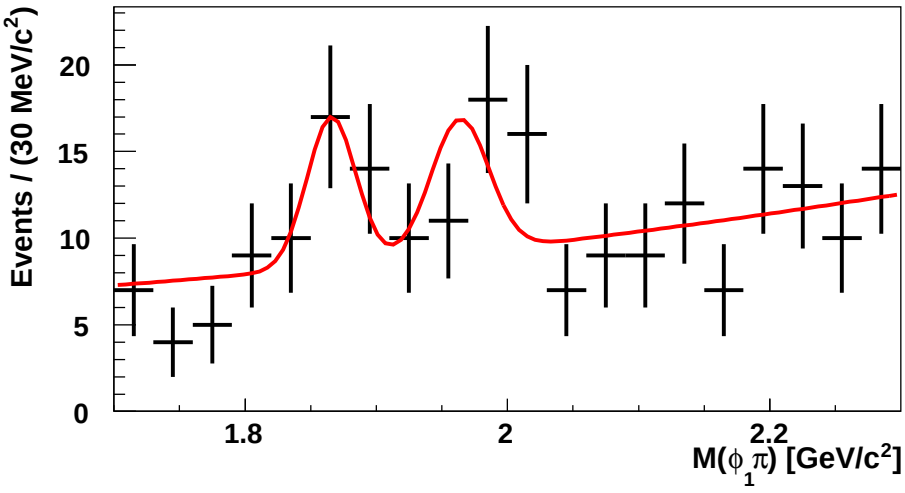

(b)

Figure 4.15: Mass plot of $(\phi_1\pi)$ for (a) events from the (KK) signal region, and (b) events in the (KK) sideband mass window. The solid curve displayed in the plot corresponds to the fitted result of the unbinned log-likelihood fit projected into the different mass regions when the fraction f_{D^+} of D^+ meson decays is released from zero.

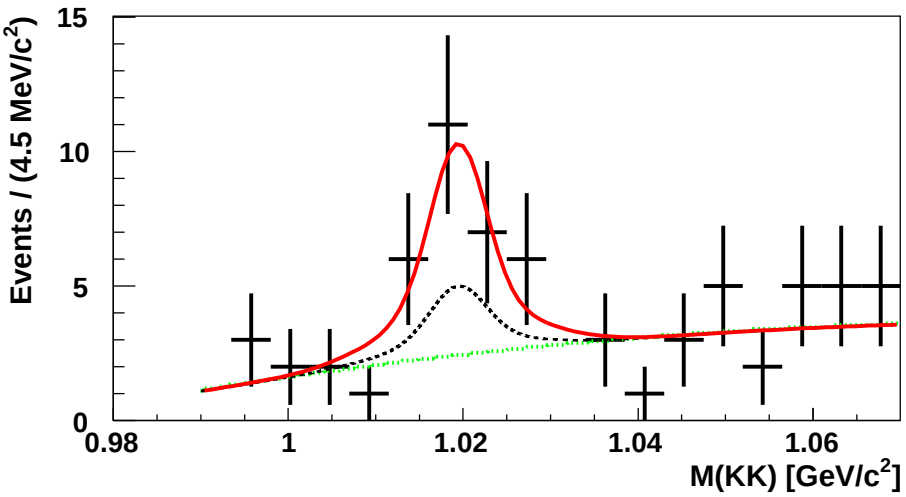

(a)

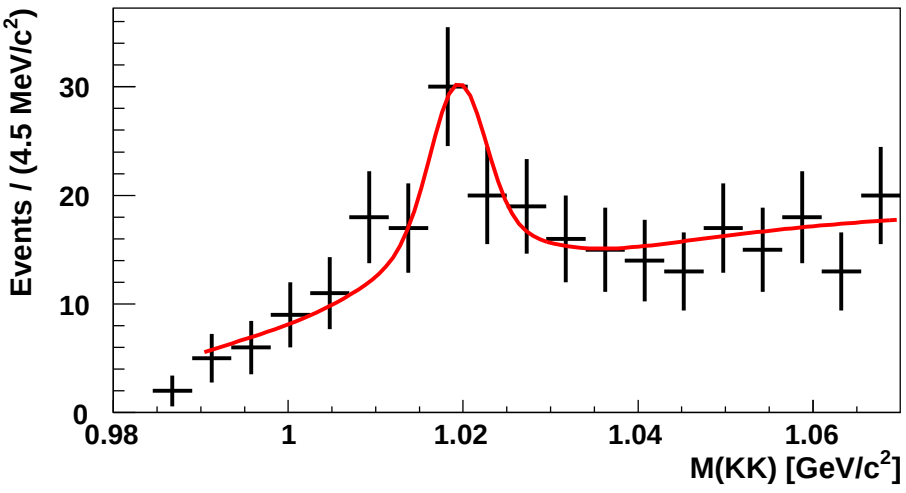

(b)

Figure 4.16: Mass plot of (KK) for $D_s \to \phi_2\mu\nu$ projected into the $(\phi_1\pi)$ (a) signal region and (b) sideband region. The superimposed solid curves are projections from the unbinned log-likelihood fit into the different mass regions when the fraction f_{D^+} of D^+ meson decays is released from zero.

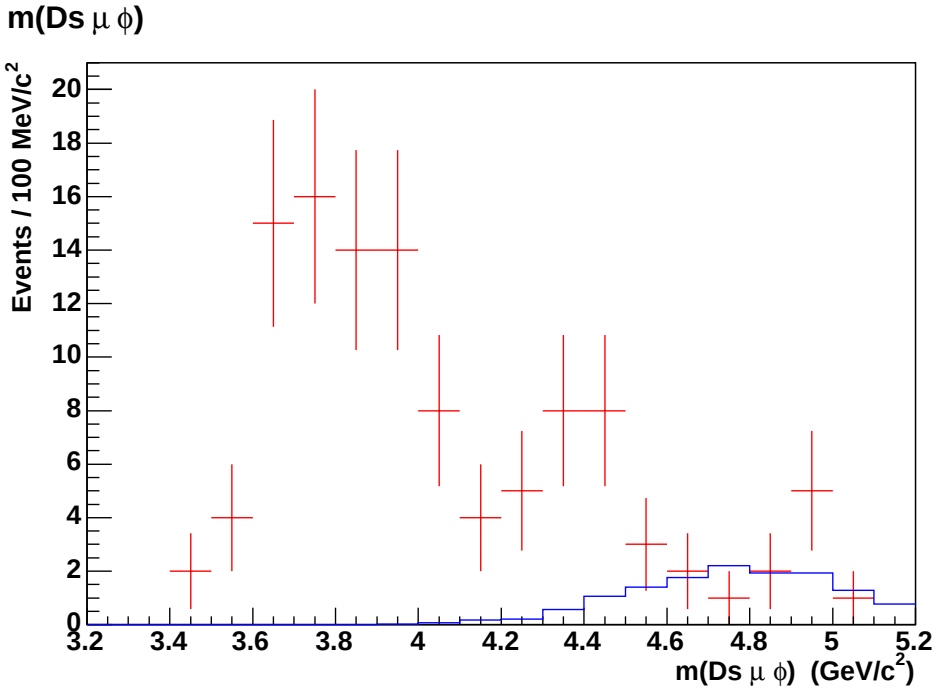

Figure 4.17: Mass spectrum of $M(\mu\phi_2 D_s^{(*)})$ for the data sample of $(\mu\phi_2 D_s^{(*)})$ candidates, shown with error bars. The $B_s^0 \to D_s^{(*)} D_s^{(*)}$ MC distribution is superimposed on this plot, scaled to the fitted number of signal events.

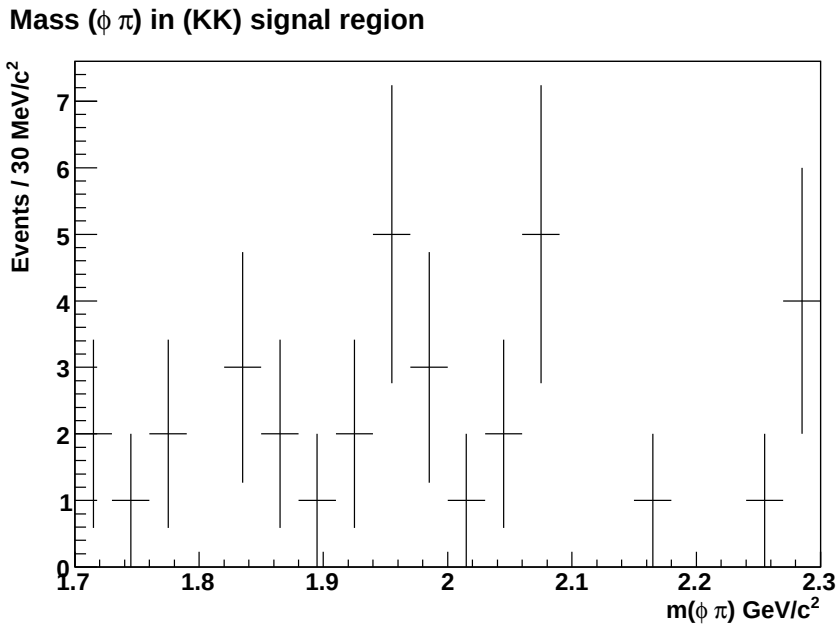

(a)

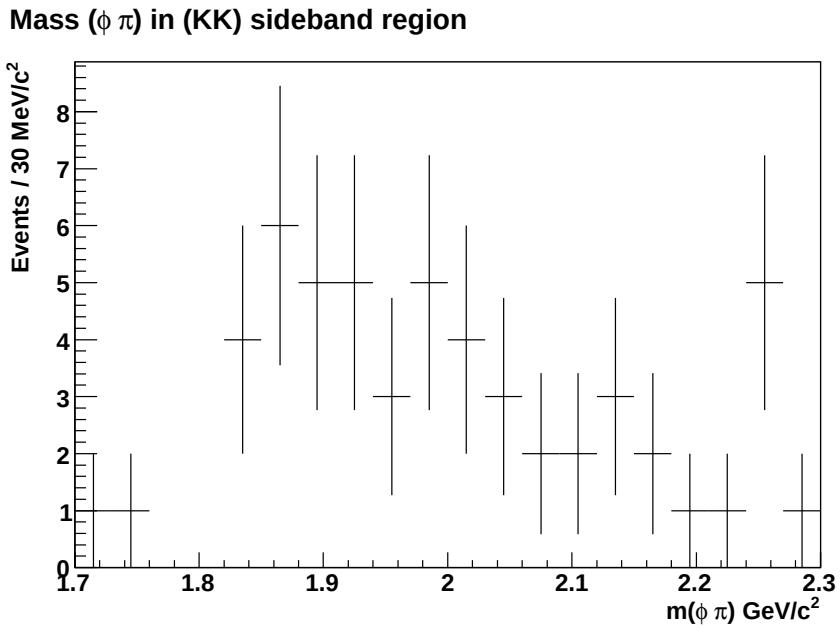

(b)

Figure 4.18: Mass plot of $(\phi_1\pi)$ within $4.7 < M(\mu\phi_2 D_s^{(*)}) < 5.2$ GeV/c^2. In (a) events from the (KK) signal region are plotted, and in (b) the histogram is constructed from events in the (KK) sideband mass window.

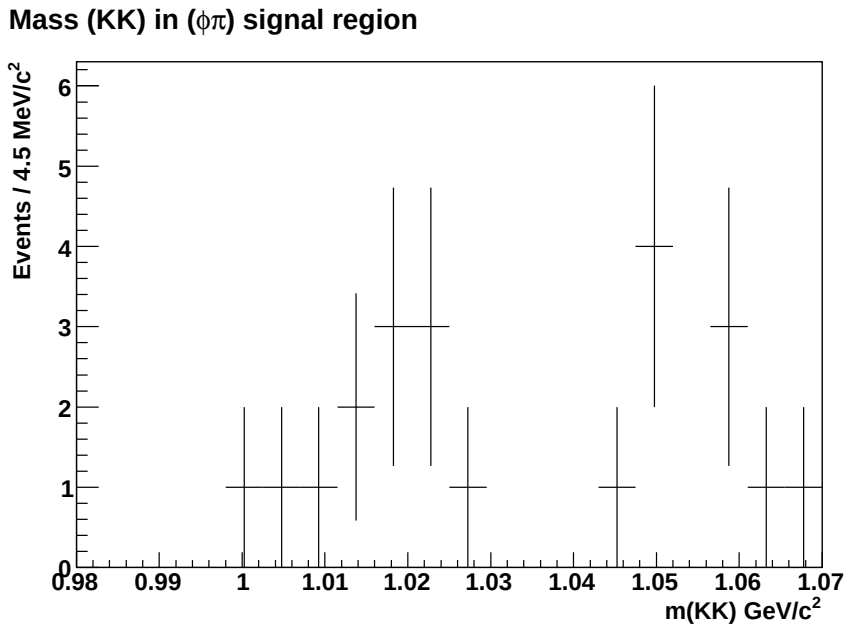

(a)

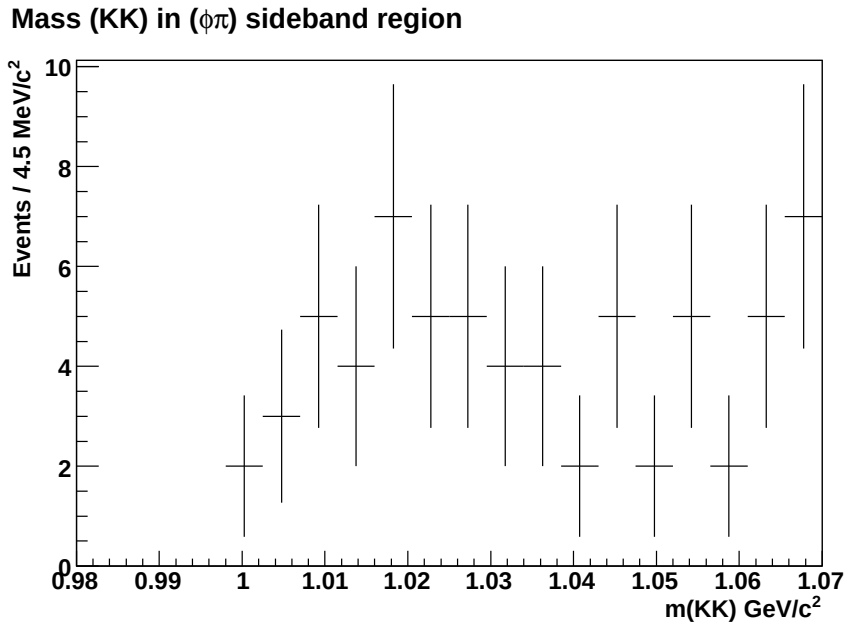

(b)

Figure 4.19: Mass plot of (KK) for $D_s \to \phi_2 \mu\nu$. Plot (a) contains events from the $(\phi_1\pi)$ signal region and in (b) events from the $(\phi_1\pi)$ sideband region are displayed for the mass window $4.7 < M(\mu\phi_2 D_s^{(*)}) < 5.2$ GeV/c^2.

From MC ~ 8.4 events were expected which is compatible with the number of events found in data.

4.9 Potential difference between trigger and decay muon

Due to the softer decay spectrum of the muon from the secondary decay in the $(\mu\phi_2 D_s^{(*)})$ rather than from the B_s^0 decay in the $(\phi_2\mu)$ sample, there exists the possibility that the muon that triggered the event is different from the muon in the decay chain. To confirm this is not the case, the number of additional muons in the event is compared between the $(\mu D_s^{(*)})$ and $(\mu\phi_2 D_s^{(*)})$ samples. The fraction of events in the $(\mu D_s^{(*)})$ and $(\mu\phi_2 D_s^{(*)})$ samples with more than one muon is found to be 0.100 ± 0.001 and 0.102 ± 0.013 respectively. No excess of additional muons are found in the $(\mu\phi_2 D_s^{(*)})$ sample providing no evidence that an additional muon triggered an increased number of events.

4.10 Data quality check

In order to maximise the available statistics, all available physics data were considered in the analysis. However, some of these runs are recorded as "bad" for particular detector subsystems. To determine whether the inclusion of runs determined as bad for the SMT, CFT, and the muon system increased the signal yield, the following study was performed. A sample of events was selected from the $(\mu D_s^{(*)})$ sample that were recorded as bad in the data quality database, contributing approximately 2% of the total sample, and the resulting $(\phi_1\pi)$ invariant mass distribution fitted, as in section 4.6. The fraction of events estimated in the fitted D_s peak is $(7.7 \pm 0.9)\%$ and $(7.6 \pm 0.1)\%$ for the bad and total samples respectively. The compatibility of these values indicate that these bad events contributed the number of expected signal events, and so were not excluded from the analysis.

Table 4.6: The hadronisation rates f and branching fractions for the background processes considered in the ($\mu D_s^{(*)}$) sample [5, 29]. Also included are the relative contributions to the ($\mu D_s^{(*)}$) sample r_i, the ratio of reconstruction efficiencies compared to the decay $B_s^0 \to D_s^{(*)}\mu\nu$.

Process	$f(b \to B)$	Branching fraction (%)	r_i (%)
$B^0 \to D_s^{(*)} D^{(*)} X$	0.397	10.5 ± 2.6	7.24
$B^\pm \to D_s^{(*)} D^{(*)} X$	0.397	10.5 ± 2.6	7.56
$B_s^0 \to D_s^{(*)} D_s^{(*)}$	0.107	12^{+11}_{-7}	2.29
$B_s^0 \to D_s^{(*)} D X$	0.107	15.4 ± 15.4	2.13

4.11 Determination of the ($\mu D_s^{(*)}$) sample composition

The fitted number of events $N(\mu D_s^{(*)})$ in Eq. 4.10 contains the number of events from the $B_s^0 \to D_s^{(*)}\mu\nu$ decay as well as various background contributions, as discussed in section 4.4.2. In the Monte Carlo simulation of the $B_s^0 \to D_s^{(*)}\mu\nu X$ sample, the following processes and branching fractions were considered [48]:

$$\begin{aligned}
\mathrm{Br}(B_s^0 \to D_s \mu\nu) &= 2.10\% \\
\mathrm{Br}(B_s^0 \to D_s^* \mu\nu) &= 5.60\% \\
\mathrm{Br}(B_s^0 \to D_{s0}^* \mu\nu) &= 0.20\% \\
\mathrm{Br}(B_s^0 \to D_{s1}' \mu\nu) &= 0.37\% \\
\mathrm{Br}(B_s^0 \to D_s^{(*)} \tau\nu) \cdot \mathrm{Br}(\tau \to \mu\nu) &= 0.51\%
\end{aligned}$$

The D_{s0}^* and D_{s1}' were each decayed to a D_s meson and π^0.

The background processes given in section 4.4.2 were assigned the branching fractions and fragmentation rates given in Table 4.6. The branching fractions for $B \to D_s D^{(*)} X$ and $B_s \to D_s D_s$ are taken from the PDG, while there is no experimental information for the $\mathrm{Br}(B_s^0 \to D_s D X)$ decay, and its value is provided by EvtGen [29] and assigned a 100% uncertainty. In addition, the ($\mu D_s^{(*)}$) sample includes the processes $c\bar{c} \to \mu\nu D_s^{(*)} X$, $b\bar{b} \to \mu\nu D_s^{(*)} X$, events with a misidentified muon, referred to earlier as peaking background.

A study was performed in ref. [51] where the Authors estimated the contributions of the peaking background to be $(10 \pm 7)\%$ for an RMS value of $80\,\mu$m. A further study [52] gave the estimate as $(13.4 \pm 4.4)\%$ for the contribution into the (μD_s) final state.

The noticeable feature of the peaking background is a small value of the visible proper decay length, centred around zero with an estimated RMS from 80 to $150\,\mu$m [51, 53]. In this analysis, the requirement of VPDL $\mathcal{L} > 150\,\mu$m was made. With this selection criterion, the estimated contribution of peaking background is reduced to $(2 \pm 1)\%$ for RMS$= 150\,\mu$m.

The fraction $f(B_s^0 \to D_s^{(*)}\mu\nu)$ of events in the $(\mu D_s^{(*)})$ sample to come from the decay $B_s^0 \to D_s^{(*)}\mu\nu$ was estimated as:

$$f(B_s^0 \to D_s^{(*)}\mu\nu) = \frac{1}{\sum_i r_i + 1} - f_{c\bar{c}}, \tag{4.21}$$

where $f_{c\bar{c}} = (2\pm1)\%$ is the $c\bar{c}$ contribution, and r_i is the ratio of contributions from each of the background processes relative to the signal $B_s^0 \to D_s^{(*)}\mu\nu$ decay, as determined from MC. The r_i include the corresponding branching fractions, the production rates $(b \to B_x)$ and the efficiencies to reconstruct each process, and is given in Tab. 4.6.

In total, the estimated fraction of events in the $(\mu D_s^{(*)})$ from $B_s^0 \to D_s^{(*)}\mu\nu$ is estimated to be

$$f(B_s^0 \to D_s^{(*)}\mu\nu) = 0.82 \pm 0.05. \tag{4.22}$$

4.12 Determination of the ($\mu\phi_2 D_s^{(*)}$) sample composition

Section 4.4.1 on page 54 lists the background processes that were considered as possible contributions to the signal. The reconstructed mass M($\mu\phi_2 D_s^{(*)}$) of the B_s^0 meson for the decays $B_{u,d} \to D_s^{(*)} D_s^{(*)} KX$ and $B_s^0 \to D_s^{(*)} D_s^{(*)} X$ is much less than for $B_s^0 \to D_s^{(*)} D_s^{(*)}$ because of the additional $\pi\pi$ pairs or K mesons in the decay. The requirement $M(\mu\phi_2 D_s^{(*)}) > 4.3$ GeV/c^2 strongly suppresses these contributions. The contribution of the decay $B_s^0 \to D_s^{(*)} D_s^{(*)} X$ is much less than $B_{u,d} \to D_s^{(*)} D_s^{(*)} KX$ because of a higher

production rate of B^+ and B^0 compared to B_s^0. The final state in the $B_s^0 \to D_s^{(*)} D_s^{(*)} X$ decay should include at least two pions due to isospin considerations; at least two gluons are required to produce this state (similar to $\psi(2s) \to J/\psi\pi\pi$) and is therefore additionally suppressed. As a result, its contribution is neglected compared to the $B \to D_s^{(*)} D_s^{(*)} KX$ process. The contribution of $B_{u,d} \to D_s^{(*)} D_s^{(*)} KX$ is described in section 4.12.1. The decay $B_s^0 \to D_s^{(*)} \mu\nu\phi$ produces a high mass of both $(\phi_2\mu)$ and $(\mu\phi_2 D_s^{(*)})$ systems. The requirement $M(\phi_2\mu) < 1.85\,\mathrm{GeV}/c^2$ strongly suppresses this contribution, which is estimated in section 4.12.2. The peaking background processes are strongly suppressed by the cut on the visible proper decay length. The selection of an additional ϕ_2 meson reduces the contribution of these processes to a small level, and its contribution is described in section 4.12.3. Finally, the decay $B_s^0 \to D_s^{(*)} \mu\nu$ with the production of a ϕ meson from fragmentation is not correlated with the decay of $B_s^0 \to D_s^{(*)} \mu\nu$ and any possible contribution of this process was taken into account by the log-likelihood fitting procedure, as this is absorbed into the f_ϕ background term of Eq. 4.12.

In addition, an attempt was made to reconstruct $(\mu\phi_2 D_s^{(*)})$ events from the $B_s^0 \to D_s^{(*)} \mu\nu$ simulation containing ~ 9200 reconstructed $(\mu D_s^{(*)})$ events. No such events were found and the contribution of this process was neglected.

4.12.1 $B_{u,d} \to D_s^{(*)} D_s^{(*)} KX$

There is no experimental information for most of the processes described above, therefore their contributions were estimated by counting events in different regions of the $(\mu\phi_2 D_s^{(*)})$ phase space and comparing the obtained numbers with the expected mass distribution for a given background process. All these processes were simulated using the standard DØ tools and reconstructed using the same algorithms as for data.

The simulation shows that for the $B \to D_s^{(*)} D_s^{(*)} KX$ decay:

$$\frac{N(M(\mu\phi_2 D_s^{(*)}) > 4.3\,\mathrm{GeV}/c^2)}{N(M(\mu\phi_2 D_s^{(*)}) < 4.3\,\mathrm{GeV}/c^2)} = 0.05 \pm 0.01. \qquad (4.23)$$

Applying the cut on $M(\mu\phi_2 D_s^{(*)}) < 4.3$ GeV/c^2 and keeping all other selections $2.8^{+11.2}_{-2.8}$ events are observed in data. The contribution of the

$B_s^0 \to D_s^{(*)} D_s^{(*)}$ decay into such a sample is very small. Assuming that all these events come from $B \to D_s^{(*)} D_s^{(*)} KX$ and using Eq. 4.23, the estimated contribution into the signal ($\mu\phi_2 D_s^{(*)}$) is $0.14^{+0.56}_{-0.14}$ events.

4.12.2 $B_s^0 \to D_s^{(*)} \mu\nu\phi$

The estimated $B_s^0 \to D_s^{(*)} \mu\nu\phi$ contribution was found using a similar method to the above procedure. The simulation shows that for this process:

$$\frac{N(M(\phi_2\mu) < 1.85\,\mathrm{GeV}/c^2)}{N(M(\phi_2\mu) > 1.85\,\mathrm{GeV}/c^2)} = 0.14 \pm 0.01. \tag{4.24}$$

Applying the cut $M(\phi_2\mu) > 1.85$ GeV/c^2 and keeping all other selections 13 ± 11 events are observed in data. The contribution of the $B_s^0 \to D_s^{(*)} D_s^{(*)}$ decay into such a sample is small. Assuming that all these events come from $B_s^0 \to D_s^{(*)} \mu\nu\phi$ and using Eq. 4.24, its contribution into the signal ($\mu\phi_2 D_s^{(*)}$) is estimated as 1.88 ± 1.51 events.

4.12.3 Peaking background in ($\mu\phi_2 D_s^{(*)}$)

Peaking background processes are strongly suppressed by the cut on the visible proper decay length. By requiring the constraint of an additional ϕ meson, possible contamination is further reduced. The contribution for the process $c\bar{c} \to D_s^{(*)} \phi\mu X$ was estimated as follows.

- The peaking background contribution in the ($\mu D_s^{(*)}$) sample was estimated in section 4.11 as $(2 \pm 1)\%$.
- An additional ϕ_2 meson is required for the ($\mu\phi_2 D_s^{(*)}$) sample. Since the production of ϕ in D^+, D^0 and Λ_c semileptonic decays is strongly suppressed, this ϕ meson can only come from a D_s meson.
- The ratio of $c \to D_s \to \mu\phi X$ in the $c \to \mu X$ sample is evaluated like this:
  - It is assumed that $\mathrm{Br}(c \to D_s)/\mathrm{Br}(c \to \mu X) = 0.1$, (similar to $b \to B_s$),
  - $\mathrm{Br}(D_s \to \mu\phi X)/\mathrm{Br}(D_s \to \mu X) = 0.3$, and

– the value $\mathrm{Br}(\phi \to K^+K^-) = 0.49$.

Combining the above terms, the estimated fraction of $c \to D_s \to \mu\phi X$ in the sample of $c \to \mu X$ is given as:

$$\begin{aligned} \frac{\mathrm{Br}(c \to D_s \to \mu\phi X)}{\mathrm{Br}(c \to \mu X)} &= 0.10 \cdot 0.3 \cdot 0.49 \\ &= 0.015. \end{aligned}$$

- Assume the efficiency to reconstruct an additional ϕ_2 meson, when the $(\mu D_s^{(*)})$ system is reconstructed, is the same for $c\bar{c} \to D_s^{(*)} D_s^{(*)}$ and $B_s^0 \to D_s^{(*)} D_s^{(*)}$, i.e., it is about 0.2.

- The requirement of $M(\mu\phi_2 D_s^{(*)}) > 4.3\,\mathrm{GeV}/c^2$ is applied to the $(\mu\phi D_s^{(*)})$ sample. Supposing a uniform distribution of $M(\mu\phi_2 D_s^{(*)})$ in peaking background between $3\,\mathrm{GeV}/c^2$ and $5.2\,\mathrm{GeV}/c^2$, the efficiency for this cut is equal to 0.4. Notice however, that peaking background events tend to have a low mass of the $(\mu\phi_2 D_s^{(*)})$ system.

- Taking all factors together and using the starting number of $(\mu D_s^{(*)})$ events = 17700, the estimated contribution is

$$17700 \cdot 0.02 \cdot 0.015 \cdot 0.2 \cdot 0.4 = 0.42 \pm 0.42 \text{ events.}$$

This number is considered as an upper limit and the corresponding uncertainty is absorbed into the systematics because the RMS of the peaking background contribution is estimated at 80 microns in ref. [53] and would give an additional factor 7 suppression.

For $b\bar{b} \to \mu\phi D_s X$ the suppression is even higher, because $b \to \mu\phi X$ can come mainly from the B_s^0 decay and $\mathrm{Br}(B_s^0 \to \mu\phi X)/\mathrm{Br}(B_s^0 \to \mu X)$ can be estimated as:

$$\mathrm{Br}(B_s^0 \to \mu\nu D_s^{(*)})/\mathrm{Br}(B_s^0 \to \mu X) \cdot \mathrm{Br}(D_s \to \phi X) \simeq 0.8 \cdot 0.18 = 0.14.$$

Here it is assumed that $\mathrm{Br}(B_s^0 \to \mu\nu D_s^{(*)})/\mathrm{Br}(B_s^0 \to \mu X) = 0.8$ and $\mathrm{Br}(D_s \to \phi X) = 0.18$ [5]. This estimate is less than $\mathrm{Br}(D_s \to \mu\phi\nu)/\mathrm{Br}(D_s\mu X) = 0.30$, used in the estimate of $c\bar{c} \to \mu\phi D_s X$ contribution.

4.12.4 Total background contribution

In total, combining the contributions from $B_{u,d} \to D_s^{(*)} D_s^{(*)} KX$ and $B_s^0 \to D_s^{(*)} \mu\nu\phi$, the background contribution $N_{\rm bkg}$ is estimated as

$$N_{\rm bkg} = 2.0 \pm 1.6 \text{ events.} \tag{4.25}$$

The systematic uncertainty of this estimate on the determination of $\mathrm{Br}(B_s^0 \to D_s^{(*)} D_s^{(*)})$ is described in section 5.3.

4.13 Monte Carlo reweighting

Differences occur between events produced from MC and data which are due to uncertainties in MC production of B mesons and from trigger effects. To account for these differences, the MC samples used in this analysis were reweighted using the ratio between data and MC for the $p_{\rm T}$ distributions of the muon and B_s^0 meson. From a study [54], a correction factor to the B meson production uncertainties was estimated. The Authors used data from $B^+ \to J/\psi K^+$ decays after correcting for trigger effects. A fit using a second-order polynomial was made to the ratio of data to MC of the B meson $p_{\rm T}$ distribution and this weighting function applied to all MC events.

The second weighting function was derived from the ratio between MC and data for the $p_{\rm T}$ distribution of the muon. Using the MC sample of $(\mu D_s^{(*)})$ events, and sideband-subtracted events in the signal region of the sample of $(\mu D_s^{(*)})$ data, the $p_{\rm T}$ distributions of the muon were constructed, as shown in Fig. 4.20. The ratio of MC to data events was plotted in bins of $p_{\rm T}$ of the muon for these samples and a second-order polynomial fitted to this distribution, shown in Fig. 4.21. The weighting function is applied to all MC events, as illustrated with the $(\mu D_s^{(*)})$ and $(\mu\phi_2 D_s^{(*)})$ samples in Figs. 4.20 and 4.22 respectively. A systematic uncertainty is assigned to the reweighting procedure and is discussed in section 5.3.

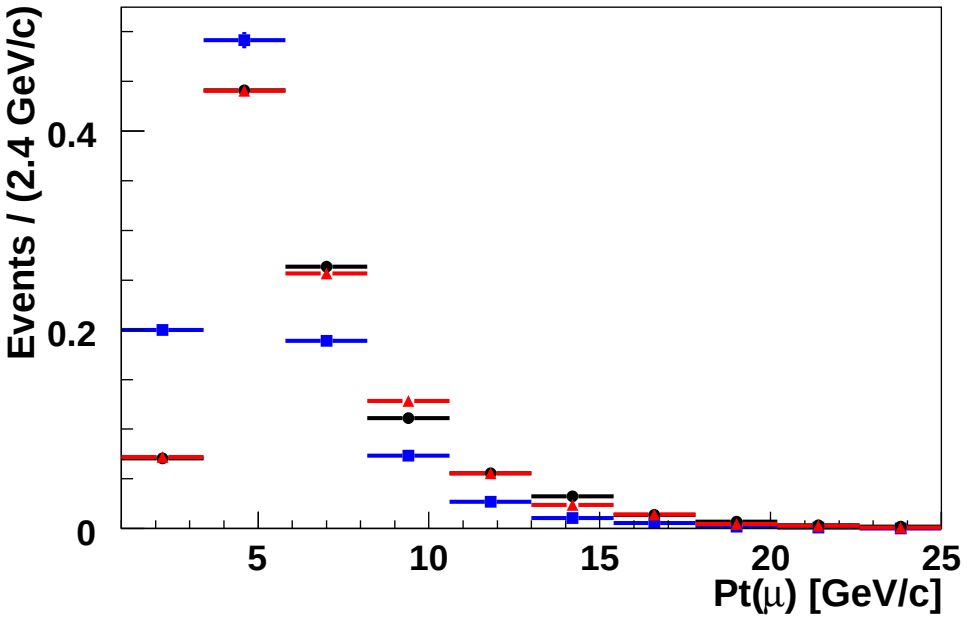

Figure 4.20: In black (circle), the normalised muon p_{T} distribution for the decay $B_s^0 \to D_s^{(*)}\mu\nu$ from the $(\mu D_s^{(*)})$ sideband-subtracted data events is shown. The blue (square) normalised histogram shows the unweighted MC for the same decay, and with the reweighting function applied the MC distribution is given as the red (triangle) histogram.

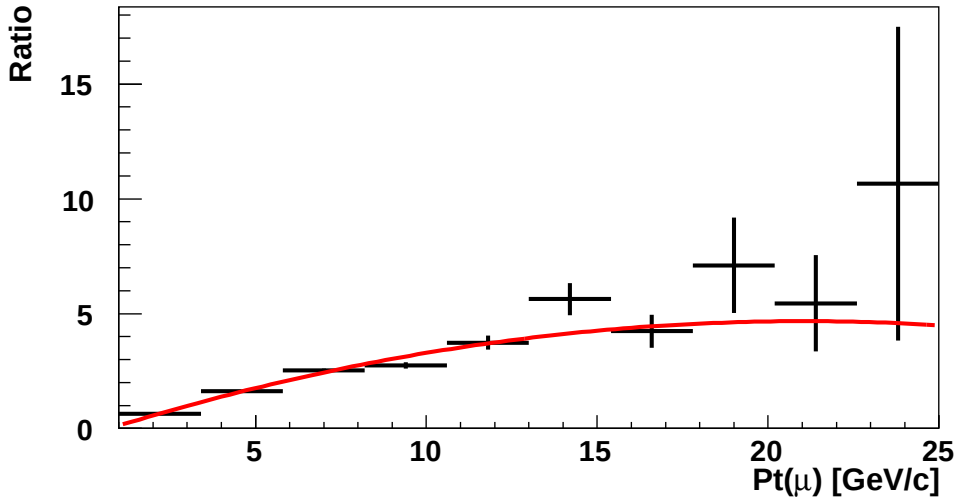

Figure 4.21: The histogram is the ratio of data events to MC for the p_{T} distribution of the muon. The reweighting function, shown as the red curve, is a second-order polynomial fitted to the histogram.

4.14 Efficiency ratio

The efficiency of reconstruction for the two processes $B_s^0 \to D_s^{(*)} D_s^{(*)}$ and $B_s^0 \to D_s^{(*)} \mu\nu$ differ due to the additional two kaons. The muon from $B_s^0 \to D_s^{(*)} D_s^{(*)}$ also has a softer p_{T} distribution than the decay $B_s^0 \to D_s^{(*)} \mu\nu$. The efficiency of reconstruction is given as the fraction of events generated as the relevant decay chain to pass all selections and be successfully reconstructed. With the correction of the reweighting functions applied, the ratio of efficiencies is found to be:

$$\frac{\varepsilon(B_s^0 \to D_s^{(*)} D_s^{(*)})}{\varepsilon(B_s^0 \to \mu\nu D_s^{(*)})} = (5.45 \pm 0.08 \text{ (stat)})\%, \tag{4.26}$$

where the error is the statistical error from MC. A systematic uncertainty is assigned to this ratio that is discussed in section 5.3.

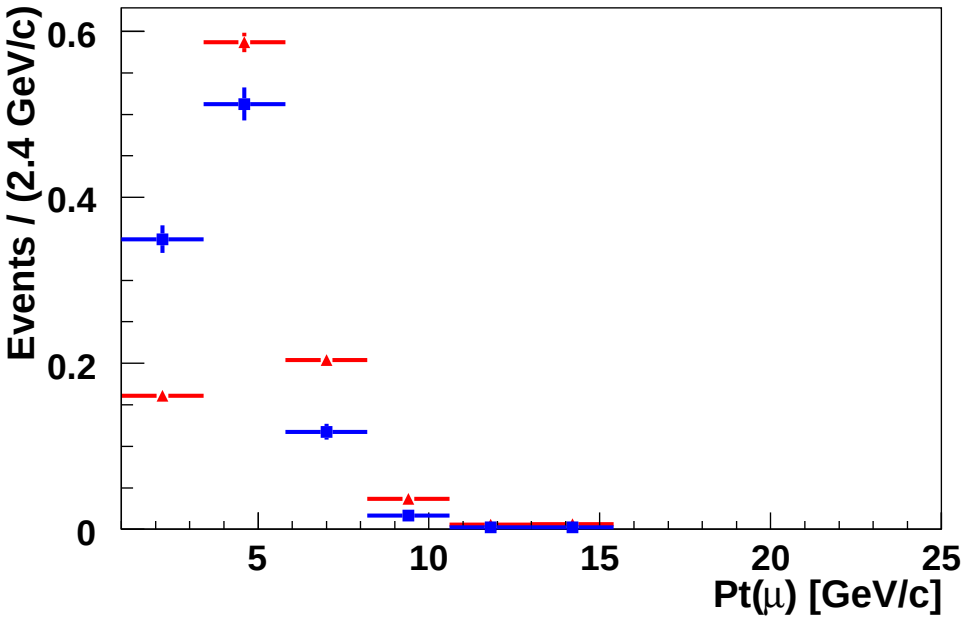

Figure 4.22: Normalised histograms of the muon p_{T} distribution for the MC decay $B_s^0 \to D_s^{(*)} D_s^{(*)}$. The original MC is shown in blue (square), and in red (triangle) are the rewieghted events.

Chapter 5

Results

5.1 Ratio R

Recalling Eq. 4.2:

$$R = \frac{\mathrm{Br}(B_s^0 \to D_s^{(*)} D_s^{(*)}) \cdot \mathrm{Br}(D_s \to \phi\mu\nu)}{\mathrm{Br}(B_s^0 \to D_s^{(*)}\mu\nu)},$$

and using Eq. 4.1, R can be re-expressed as

$$R = \frac{\left(N(\mu\phi_2 D_s^{(*)}) - N_{\mathrm{bkg}}\right) \cdot \varepsilon(B_s^0 \to D_s^{(*)}\mu\nu)}{N(\mu D_s^{(*)}) \cdot f(B_s^0 \to D_s^{(*)}\mu\nu) \cdot 2\mathrm{Br}(\phi \to KK) \cdot \varepsilon(B_s^0 \to D_s^{(*)} D_s^{(*)})}. \tag{5.1}$$

Inserting the relevant quantities obtained in chapter 4,

$$R = \frac{\mathrm{Br}(B_s^0 \to D_s^{(*)} D_s^{(*)}) \cdot \mathrm{Br}(D_s \to \phi\mu\nu)}{\mathrm{Br}(B_s^0 \to D_s^{(*)}\mu\nu)} = 0.015^{+0.0072}_{-0.0066}\ (\mathrm{stat}). \tag{5.2}$$

The value $\mathrm{Br}(\phi \to KK) = 0.492 \pm 0.006$ was taken from PDG [5]. The statistical uncertainty shown in Eq. 5.2 includes only the uncertainty in the number of $(\mu\phi_2 D_s^{(*)})$ signal events from Eq. 4.17. All other uncertainties are included as systematic uncertainties, and are discussed in section 5.3.

5.2 Dependence on Br($D_s \to \phi\pi$)

The values Br($B_s^0 \to \mu\nu D_s^{(*)}$) and Br($D_s \to \phi\mu\nu$) taken from the PDG [5] depend on Br($D_s \to \phi\pi$), which is given with large uncertainty: Br($D_s \to \phi\pi$) = $(4.4 \pm 0.6)\%$. By factorising out the dependence on Br($D_s \to \phi\pi$) from the PDG values, the branching fractions

$$\begin{aligned} \mathrm{Br}(B_s^0 \to \mu\nu D_s^{(*)})\ \mathrm{Br}(D_s \to \phi\pi) &= (2.84 \pm 0.49) \times 10^{-3}, \text{ and} \\ \mathrm{Br}(D_s \to \phi\mu\nu) &= (0.55 \pm 0.04)\ \mathrm{Br}(D_s \to \phi\pi) \end{aligned}$$

are obtained.

Inserting the above expressions into R, the value

$$\mathrm{Br}(B_s^0 \to D_s^{(*)} D_s^{(*)}) = (0.039^{+0.019}_{-0.017}(\mathrm{stat})) \left(\frac{0.044}{\mathrm{Br}(D_s \to \phi\pi)} \right)^2 \tag{5.3}$$

is obtained.

5.3 Systematic Uncertainties

The systematic uncertainties relevant to this analysis can be separated into uncertainties from: branching fraction values; sample contribution estimates; uncertainties from the use of Monte Carlo data; and the method of extracting the number of signal events from the data samples.

The systematic uncertainties in the measured value of Br($B_s^0 \to D_s^{(*)} D_s^{(*)}$) were estimated as follows.

The branching fractions, Br($D_s \to \phi_2\mu\nu$) and Br($B_s^0 \to D_s^{(*)}\mu\nu$), taken from the PDG, were varied within one standard deviation. As mentioned above, these two branching fraction depend on Br($D_s \to \phi\pi$), which is also varied within one standard deviation. The uncertainty in Br($D_s \to \phi\pi$) provides a significant contribution and is shown as a separate contribution.

In the ($\mu D_s^{(*)}$) sample, the fraction of events to come from the decay $B_s^0 \to D_s^{(*)}\mu\nu$ is estimated as: $f(B_s^0 \to D_s^{(*)}\mu\nu) = 0.82 \pm 0.05$. The uncertainty from this estimate is included as a systematic uncertainty. Due limited statistics, a 100% uncertainty in the number of background events in ($\mu\phi_2 D_s^{(*)}$) sample was assumed.

The ratio of efficiencies given in Eq. 4.26 can be affected by the uncertainties of reconstruction of two additional charged particles from the ϕ_2 meson decay. The analysis in ref. [51] measured the efficiency to reconstruct a charged pion from the decay $D^{*+} \to D^0\pi^+$ and the obtained value was in a good agreement with the MC estimate. However this comparison is valid within the uncertainty of branching fractions of different B semileptonic decays, which is about 7%. Therefore a 14% systematic uncertainty was conservatively assigned (7% for each charged particle, 100% correlated) to the ratio of efficiencies and propagated to the final result. It should be mentioned that a more recent study [55] gives a more precise comparison of efficiency in data and in simulation using muons from J/ψ decay and good agreement is also reported. For the ratio of efficiencies, a 15% value is conservatively assigned for the reweighting procedure, which reflects the difference in efficiency between reweighted and unweighted estimates.

A 2.6% systematic uncertainty is assigned to the log-likelihood fitting procedure, which was determined from the difference in the fitted number of signal events between fixing the fraction of $D^{\pm}$ events to zero and letting this fraction float in the fit. Table 5.1 shows all contributions to the systematic uncertainty, which are added in quadrature for the final result.

Table 5.1: Contributions of the estimated values of individual types of systematic uncertainty for the measurement of $\mathrm{Br}(B_s^0 \to D_s^{(*)}D_s^{(*)})$. The final systematic uncertainty is obtained from the quadrature-added value of the individual contributions.

Source	Uncertainty in $\mathrm{Br}(B_s^0 \to D_s^{(*)}D_s^{(*)})$
$\mathrm{Br}(D_s \to \phi\pi) = 0.044 \pm 0.006$	$^{+0.006}_{-0.005}$
$\mathrm{Br}(B_s^0 \to \mu\nu D_s^{(*)})\ \mathrm{Br}(D_s \to \phi\pi)$	0.007
$\mathrm{Br}(D_s \to \phi\mu\nu)/\mathrm{Br}(D_s \to \phi\pi)$	0.003
$f(B_s^0 \to D_s^{(*)}\mu\nu) = 0.82 \pm 0.05$	0.002
Background contribution in $N(\mu\phi_2 D_s^{(*)})$	0.007
Ratio of efficiencies	0.006
Reweighting of MC	0.006
Fitting procedure	0.006

5.4 Branching fraction $\mathbf{Br}(B_s^0 \to D_s^{(*)} D_s^{(*)})$

Using the result of Eq. 5.3 and including the systematic uncertainties given in Table 5.1 an estimate of the branching fraction is given as:

$$\mathrm{Br}(B_s^0 \to D_s^{(*)} D_s^{(*)}) = \left(0.039^{+0.019}_{-0.017}\,(\mathrm{stat.}) \pm 0.014\,(\mathrm{syst.})\right) \left(\frac{0.044}{\mathrm{Br}(D_s \to \phi\pi)}\right)^2 . \tag{5.4}$$

Using the value from the PDG of $\mathrm{Br}(D_s \to \phi\pi)$,

$$\mathrm{Br}(B_s^0 \to D_s^{(*)} D_s^{(*)}) = 0.039^{+0.019}_{-0.017}\,(\mathrm{stat.})^{+0.016}_{-0.015}\,(\mathrm{syst.})\,. \tag{5.5}$$

This value improves on the precision of the previous result from ALEPH [5, 17]:

$$\mathrm{Br}(B_s^0 \to D_s^{(*)} D_s^{(*)}) = 0.12^{+0.11}_{-0.06}, \tag{5.6}$$

and is still more precise if the previous value is rescaled according to the more recent estimate of $\mathrm{Br}(D_s \to \phi\pi)$, where

$$\mathrm{Br}(B_s^0 \to D_s^{(*)} D_s^{(*)}) = 0.077 \pm 0.034\,(\mathrm{stat.})^{+0.038}_{-0.026}\,(\mathrm{syst.}) \tag{5.7}$$

is obtained.

5.5 $\Delta\Gamma_s/\Gamma_s$

Assuming the decay $B_s^0 \to D_s^{(*)} D_s^{(*)}$ is mainly $\mathcal{CP}$-even and gives the dominant contribution to the width difference between the $\mathcal{CP}$-even and $\mathcal{CP}$-odd B_s^0 states, the ratio of the width difference to the average width of the B_s meson is given as (from Eq. 2.43):

$$\begin{aligned} \frac{\Delta\Gamma_s^{\mathrm{CP}}}{\Gamma_s} &= 2\mathrm{Br}(B_s^0 \to D_s^{(*)} D_s^{(*)}) \\ &= 0.079^{+0.038}_{-0.035}\,(\mathrm{stat.})^{+0.031}_{-0.030}\,(\mathrm{syst.})\,. \end{aligned} \tag{5.8}$$

Assuming that $\mathcal{CP}$ violation is small, this estimate is in good agreement with the SM prediction [15]

$$\frac{\Delta\Gamma_s}{\Gamma_s} = 0.147 \pm 0.060. \tag{5.9}$$

A direct measurement [47] of $\Delta\Gamma_s$ performed by the DØ experiment in the decay of $B_s^0 \to J/\psi\phi$ is in good agreement with Eq. 5.8, where the value $\Delta\Gamma_s = 0.12^{+0.08}_{-0.10}\,\mathrm{ps}^{-1}$, $\tau_s = 1.52^{+0.08}_{-0.08}\,\mathrm{ps}$ was obtained with the constraint $\phi_s \equiv 0$. A more recent result [19] measured the value $\Delta\Gamma_s = 0.19 \pm 0.07^{+0.02}_{-0.01}\,\mathrm{ps}^{-1}$ and $\tau_s = 1.52 \pm 0.06 \pm 0.01\,\mathrm{ps}$. In Fig. 5.1 a comparison of this result, the recent DØ result and the SM predicted value is illustrated. Using the same decay process the CDF collaboration have measured [20] $\Delta\Gamma_s = 0.076^{+0.059}_{-0.063} \pm 0.006\,\mathrm{ps}^{-1}$ together with $\tau_s = 1.52 \pm 0.04 \pm 0.02\,\mathrm{ps}$.

The results obtained by the DØ and CDF collaborations [19, 21] in the decays of B_s mesons to $J/\psi(\mu^+\mu^-)\phi(K^+K^-)$ have been combined in ref. [56]. This result (Eq. 5.8) compares well with the value obtained for $\Delta\Gamma_s/\Gamma_s$:

$$\frac{\Delta\Gamma_s}{\Gamma_s} = 0.105 \pm 0.049. \tag{5.10}$$

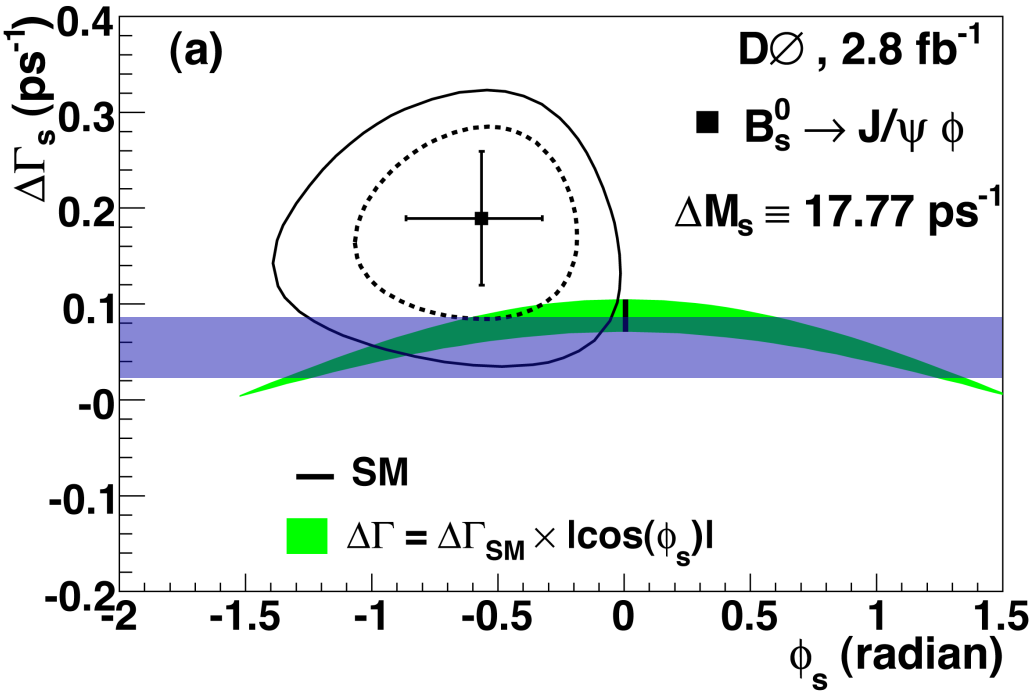

Figure 5.1: The Plot of lifetime difference versus the $\mathcal{CP}$ violating phase ϕ_s is shown from the analysis [19] in the decay of $B_s \to J/\psi\phi$. The vertical black bar is the SM prediction for $\Delta\Gamma_s^{SM}$, and in green the $\pm 1\sigma$ bands for the SM prediction as a function of the $\mathcal{CP}$ violating phase ϕ_s is displayed. The cross-hairs show the point of best fit from the analysis, with 1-dimensional projections of the 1σ uncertainties. The dashed and solid CL contours are at 68.3% and 90% respectively. Superimposed on figure is the result from this analysis, shown in blue, corresponding to the $\pm 1\sigma$ uncertainty bounds, where $\Gamma_s = 1/\tau_s$ is fixed to the value $\tau_s = 1.52\,\mathrm{ps}^{-1}$ [19].

Chapter 6

Summary and Conclusions

A measurement of the branching fraction $\mathrm{Br}(B_s^0 \to D_s^{(*)} D_s^{(*)})$ has been performed using the decays of B_s^0 mesons to two $D_s^{(*)}$ mesons, where one D_s meson decays to $\phi\pi$ and the other D_s meson decays to $\phi\mu\nu$. Both ϕ mesons decay to K^+K^-.

This result is about a factor of two more precise than the only previous measurement by the ALEPH Collaboration and hence is currently the most precise estimate of $\mathrm{Br}(B_s^0 \to D_s^{(*)} D_s^{(*)})$.

Under certain assumptions [14], the estimate of the branching fraction $\mathrm{Br}(B_s^0 \to D_s^{(*)} D_s^{(*)})$ can be related to $\frac{\Delta\Gamma_s^{\mathrm{CP}}}{\Gamma_s}$. This result translates into the strongest currently available constraint of the $\mathcal{CP}$ width difference of the B_s meson from a single measurement and is consistent with SM predictions, as well as other direct measurements. This result has been approved by the DØ collaboration and has been published in Physical Review Letters [1].

Improvements in this analysis would be realised through an increase in statistics, reducing the statistical uncertainty, as well as providing possibilities for improved analysis techniques. It is important, in order to verify the validity of the relation between the branching fraction $\mathrm{Br}(B_s^0 \to D_s^{(*)} D_s^{(*)})$ and the width difference ratio $\Delta\Gamma_s/\Gamma_s$, to distinguish the states $D_s^+ D_s^-$, $D_s^{*+} D_s^-$, $D_s^+ D_s^{*-}$, and $D_s^{*+} D_s^{*-}$.

The BELLE collaboration has collected approximately $1.9\,\mathrm{fb}^{-1}$ of integrated luminosity at the $\Upsilon(5S)$ mass [57], which has a centre-of-mass energy sufficient to produce B_s mesons. The ability of this machine to detect photons/π^0 would allow separations of the $D_s^{(*)} D_s^{(*)}$ states, and with sufficient

statistics could improve on this result.

The Tevatron, and the two detectors: DØ, and CDF have made significant contributions in high-energy physics, with the discovery of the top quark, the mass difference of the B_s^0 meson, and may find evidence for the Higgs before the shutdown of the Tevatron.

This next period of experimental high-energy particle physics will see the culmination of effort of the Tevatron experiments, with the rise of the LHC, and hopefully the realisation of an International Linear Collider, which together will undoubtedly herald new discoveries in our comprehension of fundamental physics. In this, I am fortunate to have made a contribution.

Bibliography

[1] D0 Collaboration, V. M. Abazov *et al.*, Study of the decay $B_s^0 \to D_s^{(*)} D_s^{(*)}$, Phys. Rev. Lett. **99**, 241801 (2007), hep-ex/0702049.

[2] F. Halzen and A. Martin, *Quarks & Leptons* (John Wiley & Sons, 1984).

[3] I. Bigi and A. Sanda, *CP Violation* (Cambridge University Press, 2001).

[4] D. H. Perkins, *Introduction to High Energy Physics* (Cambridge University Press, 2001).

[5] Particle Data Group, W. M. Yao *et al.*, Review of particle physics, J. Phys. G **33**, 1 (2006).

[6] P. W. Higgs, Broken symmetries and the masses of gauge bosons, Phys. Rev. Lett. **13**, 508 (1964).

[7] N. Cabibbo, Unitary symmetry and leptonic decays, Phys. Rev. Lett. **10**, 531 (1963).

[8] S. L. Glashow, J. Iliopoulos, and L. Maiani, Weak interactions with lepton-hadron symmetry, Phys. Rev. D **2**, 1285 (1970).

[9] M. Kobayashi and T. Maskawa, CP violation in the renormalizable theory of weak interaction, Prog. Theor. Phys. **49**, 652 (1973).

[10] L. Wolfenstein, Parametrization of the Kobayashi-Maskawa matrix, Phys. Rev. Lett. **51**, 1945 (1983).

[11] K. Anikeev *et al.*, B physics at the Tevatron: Run II and beyond, (2001), hep-ph/0201071.

[12] I. Dunietz, R. Fleischer, and U. Nierste, In pursuit of new physics with B_s decays, Phys. Rev. D **63**, 114015 (2001), hep-ph/0012219.

[13] BABAR Collaboration, P. F. Harrison and H. R. Quinn, The BaBar physics book: Physics at an asymmetric B factory.

[14] R. Aleksan, A. Le Yaouanc, L. Oliver, O. Pene, and J. C. Raynal, Estimation of $\Delta\Gamma$ for the B_s–$\bar{B}_s$ system: Exclusive decays and the parton model, Phys. Lett. B **316**, 567 (1993).

[15] A. Lenz and U. Nierste, Theoretical update of B_s^0–$\bar{B}_s^0$ mixing, JHEP **06**, 072 (2007), hep-ph/0612167.

[16] M. L. Mangano, Two lectures on heavy quark production in hadronic collisions, 1997, `http://www.citebase.org/abstract?id=oai:arXiv.org:hep-ph/9711337`.

[17] ALEPH Collaboration, R. Barate *et al.*, A study of the decay width difference in the B_s^0–$\bar{B}_s^0$ system using $\phi\phi$ correlations, Phys. Lett. B **486**, 286 (2000).

[18] CDF Collaboration, Observation of the exclusive decay $B_s^0 \to D_s^+ D_s^-$, CDF Note 7925.

[19] D0 Collaboration, V. M. Abazov *et al.*, Measurement of B_s^0 mixing parameters from the flavor-tagged decay $B_s^0 \to J/\psi\phi$, (2008), hep-ex/0802.2255.

[20] CDF Collaboration, T. Aaltonen *et al.*, Measurement of lifetime and decay-width difference in $B_s^0 \to J/\psi\phi$ decays, (2007), hep-ex/0712.2348.

[21] CDF Collaboration, T. Aaltonen *et al.*, First flavor-tagged determination of bounds on mixing- induced CP violation in $B_s^0 \to J/\psi\phi$ decays, (2007), hep-ex/0712.2397.

[22] Fermilab, `http://www.fnal.gov`.

[23] Fermilab Today, 6 Jan 2006, `http://www.fnal.gov/pub/today/archive_2006/today06-01-06.html`.

[24] D0 Collaboration, V. M. Abazov *et al.*, The upgraded D0 detector, Nucl. Instrum. Meth. A **565**, 463 (2006).

[25] D0, V. M. Abazov *et al.*, Measurement of the charge asymmetry in semileptonic B_s decays, Phys. Rev. Lett. **98**, 151801 (2007), hep-ex/0701007.

[26] D0 Collaboration, S. Abachi *et al.*, The D0 detector, Nucl. Instrum. Meth. A **338**, 185 (1994).

[27] D0 Collaboration, D. Bauer, B physics and triggers at D0: Operational experience, Nucl. Phys. Proc. Suppl. **170**, 288 (2007).

[28] T. Sjostrand, S. Mrenna, and P. Skands, Pythia 6.4 physics and manual, JHEP **05**, 026 (2006), hep-ph/0603175.

[29] D. J. Lange, The EVTGEN particle decay simulation package, Nucl. Instrum. Meth. A **462**, 152 (2001).

[30] D0 Collaboration, The DØ monte carlo event selection system, `http://www-clued0.fnal.gov/d0_mess`.

[31] D0 Collaboration, DØSTAR: DØGEANT simulation of the total apparatus response, DØ Note 3191, 1997.

[32] Application software group, Detector description and simulation tool, CERN Program Library Long Writeup W5013, 1995.

[33] D0 Collaboration, DØ SIM user manual, DØ Note 407, 1986.

[34] CTEQ, H. L. Lai *et al.*, Global QCD analysis of parton structure of the nucleon: CTEQ5 parton distributions, Eur. Phys. J. **C12**, 375 (2000), hep-ph/9903282.

[35] DØRECO, `http://www-d0.fnal.gov/computing/algorithms/howto/howtoreco.html`.

[36] R. A. Illingworth, Development of trigger software for the silicon and fibre trackers and a study of B meson lifetimes for the D0 experiment, FERMILAB-THESIS-2002-59.

[37] G. Borissov, Technical details of AATracking, Talk given at All DØ Meeting, 28 Feb 2003.

[38] D0 Collaboration, HTF: Histogramming method for finding tracks. The algorithm description, DØ Note 3778, 2000.

[39] D. Collaboration, The DØ Kalman track fit,, DØ Note 4303, 2004.

[40] G. Borissov, Status of D0 track reconstruction, Based on talk presented at general DØ meeting, 14 Feb 2003.

[41] DELPHI, J. Abdallah *et al.*, b-tagging in DELPHI at LEP, Eur. Phys. J. C **32**, 185 (2004), hep-ex/0311003.

[42] M. Williams, *Observations and Measurements of L=1 Orbitally Excited B Mesons at the D0 Experiment*, PhD thesis, Lancaster University, 2008.

[43] D0 tracking algorithm web page, `http://www-d0.fnal.gov/global_tracking`.

[44] D0 Collaboration, Muon ID Certification for p14, DØ Note 4350, 2004.

[45] BANA, `http://www-d0.fnal.gov/Run2Physics/ckm/d0_private/bgv/aa/bana.htm`.

[46] Skim criteria for initial dataset for general b-physics data analysis, `http://d0server1.fnal.gov/users/nomerot/Run2A/BANA/Dskim.html`.

[47] D0 Collaboration, V. M. Abazov *et al.*, Lifetime difference and CP-violating phase in the B_s^0 system, Phys. Rev. Lett. **98**, 121801 (2007).

[48] D0 Collaboration, V. M. Abazov *et al.*, First direct two-sided bound on the B_s^0 oscillation frequency, Phys. Rev. Lett. **97**, 021802 (2006), hep-ex/0603029.

[49] R. Brun and F. Rademakers, ROOT: An object oriented data analysis framework, Nucl. Instrum. Meth. A **389**, 81 (1997), `http://root.cern.ch`.

[50] F. James and M. Roos, Minuit: A system for function minimization and analysis of the parameter errors and correlations, Comput. Phys. Commun. **10**, 343 (1975).

[51] D0 Collaboration, V. M. Abazov *et al.*, Measurement of the ratio of B^+ and B^0 meson lifetimes, Phys. Rev. Lett. **94**, 182001 (2005), hep-ex/0410052.

[52] D0 Collaboration, Study of $c\bar{c}$ contribution to the semileptonic sample of B mesons, D0 Note 4639.

[53] D0 Collaboration, V. M. Abazov *et al.*, A precise measurement of the B_s^0 lifetime, Phys. Rev. Lett. **97**, 241801 (2006), hep-ex/0604046.

[54] D0 Collaboration, V. M. Abazov *et al.*, A search for the flavor-changing neutral current decay $B_s^0 \to \mu^+\mu^-$ in $p\bar{p}$ collisions at $\sqrt{s} = 1.96$ tev with the DØ detector, Phys. Rev. Lett. **94**, 071802 (2005), hep-ex/0410039, `http://www-d0.fnal.gov/~ralf/d0_private/BsMuMu/talkEB07.pdf`.

[55] D0 Collaboration, V. M. Abazov *et al.*, Measurement of inclusive differential cross sections for Upsilon(1S) production in p anti-p collisions at $\sqrt{s} = 1.96\,\text{TeV}$, Phys. Rev. Lett. **94**, 232001 (2005), hep-ex/0502030.

[56] UTfit, M. Bona *et al.*, First evidence of new physics in $b \leftrightarrow s$ transitions, (2008), hep-ph/0803.0659.

[57] Belle Collaboration, K. Abe *et al.*, Measurements of exclusive B_s^0 decays at the Upsilon(5S), (2006), hep-ex/0610003.